EXPERIMENTAL AND COMPUTATIONAL STUDY OF FLUID DYNAMICS IN SOLAR REACTOR

A Dissertation

by

MIN-HSIU CHIEN

Submitted to the Office of Graduate and Professional Studies of
Texas A&M University
in partial fulfillment of the requirements for the degree of

DOCTOR OF PHILOSOPHY

Chair of Committee,	Gerald Morrison
Co-Chair of Committee,	Nesrin Ozalp
Committee Members,	Robert E. Randall
	Devesh Ranjan
Head of Department,	Andreas A. Polycarpou

May 2014

Major Subject: Mechanical Engineering

ABSTRACT

The experimental simulation and a computational validation of a methane-cracking solar reactor powered by solar energy is the focus of this article. A solar cyclone reactor operates at over 1000 °C where the methane decomposition reaction takes place. Carbon particles are formed when methane molecules dissociate into carbon and hydrogen. During the course of this two-phase flow transport, part of the carbon particles tend to deposit on the inner surfaces such as the inner wall, window, and exit of the reactor. The deposition of carbon particles on the inner surfaces of the reactor blocks energy input and decreases converting efficiency. Particularly when they accumulate near the reactor exit, agglomeration of these particles tends to block the exit. In response to the unwanted deposition, a cyclone main flow provided a shield flow concept was predicted to prevent carbon deposition from the methane decomposition process via computational fluid dynamics (CFD). Based on the geometry of previous CFD studies an experimental validation to the effectiveness of the shield flows was performed via particle image velocimetry (PIV) and pressure sensitive paint (PSP) techniques. Three flow cases using air at atmospheric pressure, air at partial vacuum and mixture of different gas species at atmospheric pressure were used to simulate the flow interaction in the high temperature environment where methane cracking process occurs. The vortex structure in the reactor prolonged the resident time of the main flow in favor of higher energy conversion. The

optimal resident time took place when the main flow decreased by 20 % compared to a reference CFD prediction. The resident time decreased when wall streams increase.

According to the experimental data obtained from the three flow cases, a CFD simulation was performed to validate the computational model. A high temperature case simulation was compared to the room temperature cases via CFD. The CFD results showed same flow pattern between high temperature case and room temperature cases. By experimental and computational approaches, this article provides a thorough analysis to the future design and study of the solar cyclone reactors.

DEDICATION

To my family

In memory of my late grandfather, Cheng-Hsiung Chien, the giant of the Chien's family

ACKNOWLEDGEMENTS

I would like to thank my advisor, Dr. Gerald Morrison, for his continuous support throughout the course of my PhD work. I am truly grateful to him for teaching me the fundamentals of laser velocimetry and the beauty of fluid science. I have learned lots of invaluable lessons from him not only in my research work but also in my personal life. I would also like to express my deep gratitude to my Co-advisor, Dr. Nesrin Ozalp, for her strong support during my PhD work. She was always glad to answer my questions on CFD simulations. It would be impossible for me to finish my computation research without her help. I must give special thanks to my committee member, Dr. Devesh Ranjan, for his expert help with my turbulence experiments and analysis. His professional experiences and kind encouragements helped me accomplish many difficult tasks. I was benefited greatly from the discussion with my committee member, Dr. Robert Randall. He gave me many useful suggestions to improve my dissertation. I was fortunate to have them as my committee members. I would like to thank Dr. Je-Chin Han and Yang for their assistance on the PSP measurements, and to my friends Sahand, Joey, Abhay, Nico, Emanuel, Daniel, Sujan, Mustafa, and the people and staff at Turbo-machinery Laboratory for making my time at Texas A&M University a great experience.

Finally, I would like to thank my parents, my wife Chia-Wei and my younger brother Chien-Yu for their support and encouragement.

NOMENCLATURE

C	Number density, the number of particles per unit volume
D	Dimension of interrogation spot, pixel
d_{diff}	Diameter under diffraction limit, m
d_e	Particle diameter in image domain, m
d_p	Diameter of the tracking particle, m
d_r	Resolution of the recording medium, m
f	Coriolis coefficient, defined as $f = 2\omega \sin\phi$
$f^{\#}$	F-number of aperture, ratio of focal length to aperture diameter
H	Transfer function
I	Gray scale intensity in image domain
L	Axial length of solar reactor, m
M	Magnification factor
P	Pressure, kPa
S	Sutherland's constant for gaseous material
S_n	Swirl number
SG	Specific gravity at standard conditions
SNR	Signal-to-noise ratio, defined as ratio of highest peak signal to the second highest peak constructed by noise and wrong pairing.

St	Stokes number
T	Temperature, °K
t	Time
u	Velocity, m/s
$\dot{V}$	Volume flow rate, m^3/s
$\vec{X}$	Coordinate system in image domain
$\vec{x}$	Coordinate system in physical space
α	Reciprocal magnification factor, mm/pixel
λ	Wavelength of laser, m
η	Amplitude ratio of tracking particle to fluid
ϕ	Latitude
γ	Density ratio of tracking particle to fluid
τ_p	Characteristic time
μ	Dynamic viscosity, $Pa \cdot s$
ω	Angular frequency, 1/s
Γ	Diffusive coefficient

Subscript

f	Fluid
m	Measured quantity
p	Particle

TABLE OF CONTENTS

Page

LIST OF FIGURES

Page

LIST OF TABLES

1 INTRODUCTION

1.1 Motivation

Natural gas decomposition powered by direct sunlight irradiation, namely solar cracking process, provides a solution to produce emission free energy products of hydrogen gas and carbon black, which are two essential commodities in powering the modern society. Current industrial methods of hydrogen and carbon production consume energy and emit environmental unfriendly byproducts such as carbon-dioxide into the atmosphere. As an emission-free process, solar cracking of natural gas can be considered as an alternative to the conventional ways of hydrogen and carbon production.

1.2 Introduction to research

In spite of its environmental attractiveness, this technology faces some challenges such as protecting the window from carbon particles to allow the solar irradiation to penetrate, reactor clogging due to carbon particle deposition, protection of the reactor against thermal shock, and loss of solar power from the window due to multiple reflections. There have been many innovative solar cracking reactor designs aimed to achieve higher converting efficiency. The current development of a solar reactor aims to enhance flow dynamics that result in improved overall efficiency and reduction of carbon deposition, however, the carbon deposition still remains. This study summarizes the research

contents including an experimental study of the solar reactor model, a CFD validation of the experimental result and the computational result of this solar reactor concept.

During the research and development of the reactor, gas phase methane is chosen as the fuel for its simplicity. The chemical process of methane decomposition takes place at temperature of order of 1000 °C. Among the decomposition processes the carbon is formed and accumulated into particles that start to deposit on the inner surface of the reactor. The total efficiency of the conversion decreases when the reactor window is covered with increased deposition. In order to solve the carbon deposition issue, a gas shield solar reactor is developed. In a gas shield solar reactor, additional gases are injected into the reactor. These streams serve as a shield layer to prevent energy conversion drop from carbon deposition on the inner surfaces, and they also provide a buffering layer to prevent high heat damage to the inner wall surface materials.

The initial setup of the experiment is based on earlier computational studies. The reactor model is constructed of transparent polycarbonate. The fluid properties in the real reactor can be simulated by surrogate gases under partial vacuum. In this manner, an identical flow field can be obtained without needing the high temperature to experimentally achieve optical observations on the flow interaction between a cyclone main flow and two shield auxiliary flows around the cyclone via 2-D particle image velocimetry (PIV) and the carbon deposition via pressure sensitive paint (PSP) technique.

The PIV measures the vortex structure from the virtual center line to the periphery region. The experiment runs under different vacuum pressures in order to match the fluid density in the real reactor. The results presented are obtained using air as the working fluid. The inlet flows are seeded by the tracking particles with particle diameter of 1 μm to observe the mixing of the main flow and the shield flows. The carbon particle transport in the flow and deposit on the inner wall is observed using nano-scale carbon particles. In addition to the PIV technique which measures the internal field of the cyclone, the PSP technique can acquire flow information on the wall. The PSP measurement is used to measure the flow mixing on the wall to evaluate the effectiveness of the auxiliary flows against the particle deposition. The experiment runs at atmospheric pressure, using mixture of air and carbon dioxide to approximate the blowing ratio. The cyclone structure is captured from axial and transversal views at positions of fixed spacing. The qualitative and quantitative analysis of the velocity vector field and concentration distribution of the auxiliary gases provides understanding to the internal flow dynamics as well as guidelines to the solutions of carbon particle deposition, energy converting effectiveness and heat transfer.

A computational reactor model is validated with the experimental result from the PIV and PSP measurements. After the validation a simulation is performed to predict the flow dynamics and heat transfer in a high temperature solar reactor using different turbulent and radiation models.

2 LITERATURE REVIEW

2.1 Hydrogen and solar reactor research

Current methods of hydrogen production come from steam methane reforming, electrolysis, thermolysis, coal gasification or carbonization etc. During the above industrial processes, large amounts of energy are consumed and/or carbon-dioxide emission is created. Since the industrial production of hydrogen mainly relies on a carbon-rich compound as the source of conversion, the major issue of the hydrogen generation comes from the carbon processing during the extraction. In order to reduce the energy consumption and carbon emission in current industrial methods, Ozalp (2008) proposed that the solar cyclone reactor using direct solar irradiation to dissociate methane into hydrogen and carbon particles be used. Methane decomposition which produces carbon particles was numerically and experimentally described by Muradov, Chen, Smith and T-Raissi (2005) using a fluidized bed reactor.

In spite of emission free advantage, like many generating or power output devices that contains carbon production as part of the process, the solar reactor faces carbon deposition problems during the production of hydrogen, which significantly decreases the life span of the device. Also, the solid deposition at the exit can cause failure as comprehensively described in Shilapuram, Devanuri, Ozalp (2010) and Abanades, Rubbia, Salmeiri (2012)'s works. In order to solve the deposition issue, a solar cyclone

reactor was proposed by Steinfeld in Switzerland (1998), Kogan in Israel (2002), and Ozalp in Qatar (2008).

Szekely and Carr (1966) investigated the effect of the presence of solid particles to the heat transfer between a cyclone wall and a gas-particle suspension. Good heat transfer was observed between the particles and the heated wall. However, the presence of particles also decreased the heat transfer between the wall and the gas compared to the heat exchange with gas alone. The heat exchange is mainly affected by the particle size, specific heat and density rather than the thermal conductivity.

Steifeld, Brack, Meier, Weidenkaff and Wuillemin (1998) demonstrated a solar chemical reactor running ZnO and methane to form a gas-particle vortex to convert the input mixture into Zn and syngas. During the experiment a 2000 times concentrated solar intensity raised operating temperature up to 1600 $^{\circ}$K. 90 % Zn conversion was achieved. The inner wall of the reactor was engraved with a helical groove feature to guide the carbon particles to increase the resident time and heat transfer between the reactants and wall. A CFD simulation using the k-epsilon turbulence model was performed. The result showed a helical trajectory of main flow from the inlet to the exit and another helical trajectory around the axis in opposite direction for the auxiliary window flow. An encouraging conclusion of economic benefit from solar reactor was evaluated by Weimer (2000) and Ozalp (2009).

Cortes and Gil (2007) discussed the effects of unsteadiness and asymmetry fluid to the modeling of multi-phase particle-gas swirling flows. The precessing vortex core (PVC) induced by strong rotation or instability starting at downstream of vortex line leads to asymmetry and pressure loss of a cyclone. The resulting precessing vortex could displace the vortex core from the geometry center of the device. In a cyclone flow, a Rankine vortex profile with semi-free vortex outer part in form of $u_{\tan} r^n = C$ where $n = 0.4 - 0.8$ is found as a result of viscosity. The pressure loss is dominated by the viscous dissipation. When wall friction increases, the pressure loss decreases as a result of decreasing tangential velocity. The effectiveness of current turbulence models to simulate swirling flow was discussed. Apart from the costly models, the very sensitive Rankine vortex profile could be obtained by Reynolds Stress models. Steady RANS models with higher order discretization gave adequate capability to simulate a cyclone flow while the unsteady RANS models could capture the PVC.

Kogan and Kogan (2002) proposed an auxiliary gas curtain to sweep the particle deposition on the reactor window from overheating the reactor wall. A tornado-like flow pattern with tangential main flow inlet can reduce the required radial auxiliary gas flow rate to 5 % of the main flow rate by the aid of radial pressure gradient. A funnel-like jet was the result of radial motion of fluid driven by the pressure gradient, provided the centrifugal force to the fluid particles was sharply reduced by the friction within the boundary layer above the reactor window.

Hirsch and Steinfeld (2004a) designed a 5-kW two-cavity configuration with an auxiliary gas injecting into the aperture and reactor window to cool and keep the surfaces free of particles. A steady convection/conduction coupling multi-phase heat transfer simulation was performed via a ray-tracing analysis using a Monte-Carlo method to simulate heat exchange between the gas-particle and the diffusive-gray reactor (2004b). Mie-scattering theory was applied to the gas-particle property. The radiation properties of two different size micro-scale particles under two irradiation peak wavelengths at 1200 $^{\circ}$K were reported. Higher and more uniform broad-band attenuation was obtained by using larger particles. A rapid increasing gas-particle temperature profile within 5 % the inner wall length was obtained at different gas-particle mass flow rates. A lower wall temperature was achieved with higher particle mass flow rate.

A solar reactor with screening window flow was experimentally simulated at room temperature by Kogan, Kogan and Barak (2004). A tornado flow configuration helped to enhance the effectiveness of the window screening. A wall screening flow was added to counteract the reversed periphery rotating flow containing particles toward the reactor window. The carbon particle deposition was solved by the above two auxiliary flow setting under the specific reactor geometry. The minimum location from the entrance beyond which the negative reversed flow effect was prevented was determined. The applicability of the ambient temperature experiment to simulate a high temperature flow pattern was justified.

Kogan, Israeli and Alcobi (2007) obtained a numerical result indicating that the main stream entering at top periphery of the reactor split into two directions. The majority of the main stream moved along the cylindrical wall toward the exit, and the rest accelerated radially toward the center of the reactor window and then made a sharp turn in the axial direction toward the reactor exit. Upon reaching the exit following the former route, part of the fluid traveling along the cylindrical wall separated from the original path and turned toward the reactor window between the funnel jet and the fluid along the cylindrical wall, the rest continued to the exit. Part of the reversing fluid reached the reactor window and became the source of particle deposition, and the rest rejoined the neighbor fluid traveling toward the exit. This particle deposition on the reactor window caused by the toroidal flow was observed before. The toroidal effect could be reduced by injecting flow in the opposite direction of rotation to suppress the deposition issue. It also showed that high operation temperature alleviates particle deposition since the fluid tended to be laminar which prevented the reversing fluid from reaching the reactor window. On the other hand, the deposition could be observed in a turbulent case at room temperature.

Chen, Chen, Hsieh and Siegel (2007) modeled a 3-D steady rectangular solar receiver using an Eulerian model for the multi-phase gas-particle mixture, the discrete ordinate (DO) model with ray-tracing method as the radiation model, and realizable k-epsilon model for fluid dynamics. The same simulation group then described multi-phase radiation heat transfer between gas-particle and inner surfaces via two band DO model.

Either decreasing the particle size or increasing the particle mass flow rate could lead to higher particle absorption efficiency.

Daw, Rempe and Knudson (2010) measured the specific heat capacity, thermal expansion and thermal diffusivity via a high temperature measurement for Inconel 600 up to 1473 $^{\circ}$K. Thermal conductivity and density of the material were calculated based on the measurement data and compared with the extrapolated data from other literatures. A specific heat capacity difference was reported while the thermal conductivity was very close to previous industrial data. The result showed that the density of Inconel 600 decreases linearly as temperature increases, which can be approximated as d = 8865 - 0.42T ($^{\circ}$K) kg/m^3. The specific heat capacity can be approximated as c = 386 + 0.2T ($^{\circ}$K) J/kg-K; the thermal conductivity can be approximated as k = 4.3 + 0.018T ($^{\circ}$K) W/m-K. Dalzell and Sarofim (1969) developed an optical means to relate the spectral absorption coefficient and total emissivity of soot suspension to the soot concentration when measuring the heat flux during combustion via soot concentration.

Rodat, Abanades, Sans and Flamant (2010) performed a 2-D axis-symmetric simulation to a solar reactor heated in a 1 MW solar furnace. Incomplete dissociation in form of C_2H_2 was reported. A 77 % optimal black body absorption efficiency at 1800 $^{\circ}$K was achieved numerically compared to the 15 % thermal efficiency during experiment due to the heat loss, which illustrates the requirement for both thermal insulation and specific solar concentrating strategy. Rodat, Abanades and Flamant (2010) also tested two solar

reactor configurations to recover the carbon black while the original configuration produced hydrogen product in form of C_2H_2 instead of hydrogen at 2073 $^{\circ}$K.

Ozalp and Krishna (2010) computationally investigated the effect of inner surface condition upon the axial temperature profile and gas species mole fraction distribution in a reversed flow solar reactor. Global absorption, scattering coefficients and Mie theory were used for the particle property. The RNG model was used as the turbulence model. It was found that the surface had minor effect on the residence time of the particles and the outlet temperature. Shilapuram, Krishna and Ozalp (2011) also performed a residence time analysis by applying a tracer injection method onto an aero-shield reactor model. A trend of increasing residence time by decreasing the flow rate was reported. The flow dynamics and gas thermal properties also affected the residence time. In general, a vortex flow pattern can help to prolong the residence time while the auxiliary flows are against it.

Wu, Caliot, Flamant and Wang (2011) also simulate a 2-D steady heat transfer and flow dynamics coupled model for a solar air receiver. The standard k-epsilon, P1 radiation and local thermal non-equilibrium models with a SIMPLE solution scheme were used to predict the temperature distribution on a 2-D cross-section of the reactor.

Krishna and Ozalp (2013) numerically investigated the cyclone gas structure comprised of three gas flows and carbon particles at the same time by adopting the discrete phase

model (DPM) to the turbulence model to quantify the particle deposition on the inner surface of the reactor. The carbon deposition with respect to the individual flow rates, particle size and mass rate were qualitatively discussed.

A multi-auxiliary flows design was proposed and experimental tested by Ozalp, Chien and Morrison (2012, 2013). A wall shield flow was added to protect the inner wall in addition to the window screen flow proposed before. A wall shield flow using Argon was computationally proved to be an effective means to prevent particle deposition on the inner surface of the reactor. The interacting effect between the main flow, wall shield flow and window shield flow from the center to the wall of the reactor by whole field visualization techniques was reported. A resident time evaluation was performed based on the experimental result.

2.2 Development of flow visualization

Particle image velocimetry (PIV) evolved from the laser speckle velocimetry (LSV) originally developed in solid mechanics in 1970s. In 1984 the term PIV was for the first time distinguished from the LSV mode by the definition of source density in Adrian's work (1984). At early stages of PIV development in 1980s, the particle images were recorded on photographic film and processed optically by evaluating Young's fringes or analog auto-correlation peak. Thus the PIV technique was time consuming and did not gain wide popularity in the flow visualization community until the advent of high speed computational resources and digital recording medium. Nowadays, the conventional PIV systems are digital and double exposed for discrete cross-correlation via fast Fourier Transform (FFT). The performance of a digital PIV is as accurate as film PIVs discussed by Westerweel (1993). PIV especially gained its popularity over other velocimetry techniques because of the capability to measure the derivative quantities, i.e. vorticity.

Before the emergence of PIV, the displacements of particles pairs in LSV mode were obtained by the Young's fringe method proposed by Burch and Tokarski (1968). This optical method was also applicable to the LSV with lower particle image density, i.e. PIV. The discrete feature of particle images due to the lower image density made it possible to apply other statistics methods to evaluate the particle displacement than LSV.

At the beginning of PIV development, different kinds of illumination source, recording medium, particle type, time coding, statistics techniques were proposed by Adrian (1986). The uncertainty was formulated as a function of laser pulse, diffraction limit, recording medium resolution, particle diameter, and sub-pixel evaluator applied. Nishio (2008) derived a complete description to quantify a 2-D PIV measuring uncertainty for a medium speed subsonic flow. The 3-D effect, the miss-match error and other major bias limits are discussed.

$$\frac{\sigma_u^2}{u^2} = \frac{\sigma_{\Delta x}^2}{\Delta x^2} + \frac{\sigma_{\Delta t}^2}{\Delta t^2}$$

The major source of uncertainty generated by locating the particle image centroid was identified. The uncertainty induced by time was about 1 % and in general neglected. The optimal light sheet thickness of 0.5 – 1 mm was documented.

Keane and Adrian (1990, 1991) proposed the measuring criteria of PIV by theoretical and numerical simulations. According to the simulating result, the image density, namely the particle number per interrogation spot N_I should be larger than 10, the local velocity gradient within interrogation should be lower than 5 %, and the in-plane and out-of-plane motion should not exceed 1/4 of the interrogation spot, namely the one-quarter rule of PIV.

Adrian (1997) derived the mathematical description of the dynamic velocity range, defined as the maximum velocity divided by the minimum resolvable velocity, along with the dynamic spatial range under considerations of system setup and particle properties. The optimal performance of PIV can be evaluated by the following equation.

$$DVR_{opt} = \frac{c_{\max}}{c_\tau \sqrt{1 + c_r^2}}$$

where $c_{\max}$ is the max displacement of a particle image pair; c_τ is in percentage error with respect to the particle image diameter for determining the particle image centroid, usually 10 %. c_r is the number of pixels that make the diameter of a particle image, usually 2.

Since the interrogation window size affects the spatial resolution of PIV, by implementing an averaging scheme on a DNS simulation, Saikrishnan, Marusic and Longmire (2006) studied the effect of spatial averaging within the interrogation window. A visualization comparison between PIV and filtered DNS data is made in the logarithmic region of turbulence. Philip, Hutchins, Monty and Marusic (2013) presented a frame work for studying the spatial resolution of finite sensor characteristic length to velocity measurements. The experimental data from a hot-wire measurement in a 2-D turbulence flow near wall region was correlated with the corresponding spatial-averaged DNS database. The correlation in spatial and spectral domains showed the limit of the

highest spatial resolution a hot-wire probe with finite probe length can possibly achieve. The relation between the characteristic length scale of sensor and the resolvable eddy scales was documented. It also proved that the turbulence flow condition can affect the resolution of measurement with a fixed characteristic length sensor.

Keane and Adrian (1992) investigated the effect of correlation methods in theoretical simulations. The effects of image density, multiple exposures, in-plane loss, out-of-plane loss, tracking particle concentration and interrogation spot size to the system performance are characterized, where the image density was defined as the number of particle images per interrogation window.

A velocity gradient can cause multiple peaks or a wide and weak peak within a single interrogation spot. Hart (1998) proposed a spatial averaging method disregarding the correlation algorithm selected by multiplying adjacent correlation maps to increase the sub-pixel accuracy. By comparing the two entire correlation maps, any correlation value that doesn't appear in both correlation maps is attenuated from the resulting map. Therefore the Hart correlation is very robust eliminating white noise and random errors. But this correlation error correction fails when the relative particle displacement between the two correlation maps is more than one particle image due to high velocity gradients.

Prasad, Adrian, Landreth and Offutt (1992) examined the effect of the interrogation spot resolution to the interrogation speed by using a test photograph where the displacement

was known. Westerweel (2000) performed a measurement precision analysis on PIV. The theoretical accuracy of sub-pixel is 0.02 pixels under ideal condition. The measurement errors were expressed as a function of sub-pixel displacement, the particle image diameter and image density. The result showed that when the particle image diameter is smaller than two pixels, the peak locking occurs and the error increase drastically. On the contrary, the error increases proportional to the image diameter. The image density should larger than 10 to control displacement error under 0.05 pixel according to the simulation.

Adrian et al. (2000) presented comparisons of resolving small scale components from specific PIV turbulence flow data using Galilean decompositions, Reynolds decompositions, LES decompositions and critical-point analysis at different locations normal to the wall. He (2007) also described an early PIV application resolving the progress of coherent structures including the streamwise vortices, hairpin vortices and hairpin pocket formation in the wall region. The 2-D PIV measurements were compared with the DNS data to resolve the background physics of the wall turbulence that contribute to momentum transport and kinetic energy production.

Mei (1996) proposed the fidelity of spherical tracking particles to follow the fluid at finite Reynolds numbers by Stokes flow theory. The frequency response and energy transfer functions are formulated to determine how well the particles following the fluid. The cut-off-response and cut-off size of the particles are estimated to determine the

largest size of tracking particle to ensure discernible particle displacement. Melling (1997) further focused on the tracking particle of high particle-fluid density ratio. The generations of both liquid and solid particles were introduced. Global seeding upstream far enough from the measuring volume is in general preferred over local seeding for high particle concentration to reach the homogeneity of particle distribution.

Zhang and Sarkar (2011) investigated a near-ground tornado to quantify the structural characteristic of the artificial tornado using digital double pulsed PIV. The vortex wandering, a seemly random motion of the vortex center round its mean position was observed. A vorticity diffusion and forced-free tangential velocity profile was captured. The magnitude of the tangential component is about three times of the maximum radial components regardless of the swirl ratio.

Natarajan (2011) performed a 3-D unsteady simulation on a tornado-like vortex at different swirl ratios using FLUENT. 150,000 cells with Hex/Wedge mesh were used. Velocity-gradient adaptation, region adaptation and Y+ adaptation were applied in post process. Reynolds stress model and large-eddy simulation models were used as the turbulence models. SIMPLEC pressure-velocity coupling scheme with second order discretization for the rest turbulence variables. The turbulent intensity was 1 %, and the turbulent viscosity ratio was either 1 or 10, which didn't significantly affect the result. Enhanced wall treatment was applied to the wall boundary condition. The Y+ is about

order of 1, which requires very fine mesh near the wall. Velocity inlet, free-slip side wall and outflow outlet were used. A forced-free vortex profile was obtained.

A successful pressure sensitive paint measurement using a photo-luminescent paint was presented by Morris, Donovan, Kegelman, Schwab and Levy (1993). The effects of temperature variation, camera calibration, model movement and paint contamination were identified. The 8 % RMS error was determined between the experimental data and a least-square fit. The noise reduction was performed to reduce the background noise. McLachlan and Bell (1995) indicated that the measuring uncertainty increases dramatically to more than 10 % when the characteristic flow Mach number is less than 0.1. The pressure resolution of the paint compared with the pressure tap measurements could be less than 1 kPa (344Pa) for supersonic flows and 1.5 kPa for transonic flows.

Liu, Guille and Sullivan (2001) derived the error propagation equation of PSP measurement via system modeling. The relation between the luminescent condition and the imaging system parameters was obtained based on the light transport and photo-detector response to the luminescence. The bias errors and the corresponding sensitivities were evaluated. The minimum uncertainty that the PSP can achieve was determined. It's shown that temperature had the highest sensitivity coefficient and the lowest upper bound of error in measurement. Therefore temperature must be corrected to obtain quantitative pressure result.

Han and Rallabandi (2010) presented a PSP measurement on film cooling application for turbine blade. The sources of uncertainties were identified. The major term that affects the accuracy of PSP is the intensity resolution with respect to the partial pressure of oxygen. A typical value of 15 % error was estimated when the mainstream and the coolant gas are highly mixed. The direct data curve-fit calibration instead of conventional Stern-Volmer equation calibration was recommended. The maximum error due to curve-fit was less than 1-2 %. The effects of excitation fluctuation and camera random noise can be removed by applying assemble-averaged technique. In order to eliminate the temperature dependence, the coolant gas temperature should be the same as the mainstream temperature.

3 METHODOLOGY

3.1 Overview

This solar reactor research is divided into three phases. In the first phase, a room temperature experiment of a solar reactor model is designed, built, calibrated and tested. The initial experimental fluid parameters are estimated via a thermodynamic analysis according to a reference CFD research. The corresponding PIV parameters are calculated via an optical analysis and a Stokes flow analysis. The measurement accuracy is evaluated by an uncertainty analysis and a correlation analysis using synthetic data. In the second phase, a room temperature experiment simulating a high temperature solar reactor is performed via PIV and PSP techniques to measure the cyclone flow dynamics from the center to the near wall region of the reactor and shield flow effectiveness respectively. In the third phase a computational fluid dynamics (CFD) research using the boundary conditions of the room temperature experiment in the second phase is performed. The simulation result is validated with the experimental result. Then the reactor geometry and inlet conditions are numerically modified, the simulation results are compared to search for optimal performance of the solar reactor.

Because the PIV measurement in this application relies on maintaining the velocity vector field in the room temperature model same as that in the real reactor, the geometry

and volume flow rates are kept identical to those of the real reactor. In order to maintain the flow field the same as that of the real reactor in the room temperature experiment, the fluid properties in the reactor model is set to match the flow dynamics of the solar reactor at high temperature where the methane-cracking reaction takes place. This is achieved by changing the operating pressure and the inlet gas species in the experiment to match the bulk flow density, the Reynolds number and the blowing ratio between the main flow and the wall shield flow in the real reactor.

The reactor model geometry design for manufacture is performed via SolidWorks; the thermodynamic properties of fluids are calculated via a MATLAB parametric analysis by extrapolating the fluid properties from the earlier CFD studies of a solar reactor by Ozalp, Hogan and Steinfield. The optical performance of PIV is evaluated by empirical equations based on Adrian's theoretical study based on synthetic data, an optical and gas dynamic simulation of the experimental setup is performed via MATLAB code to search for the optimal setting for the PIV measurement.

In order to validate the result from the CFD simulation via PIV measurement, the reactor model is operated under the same bulk density as that in the CFD simulation by means of lowering the operating pressure in the reactor model down to around 1/3 absolute atmospheric pressure. The vacuum pressure is maintained by a 220 Voltage single phase vacuum pump downstream of the reactor model, controlled by a vacuum regulator.

In the PSP measurement, the gas mixture is used to verify the effectiveness of the wall shield flows against carbon particle deposition with blowing ratio close to that of the real reactor. During the experiments a gas species correction for the rotameters and reference concentration calibration are required.

3.2 Parametric analysis

3.2.1 Thermodynamic analysis

Based on earlier CFD case studies for high temperature solar reactors, a thermal-fluid analysis is performed to duplicate the flow field at room temperature. Since the reactor operates at high temperature and atmospheric pressure, the ideal-gas assumption is applied. Firstly the temperature distribution profile is estimated as shown in Figure 1 via a CFD solar reactor heat transfer simulation by Ozalp (2010) as the reference case.

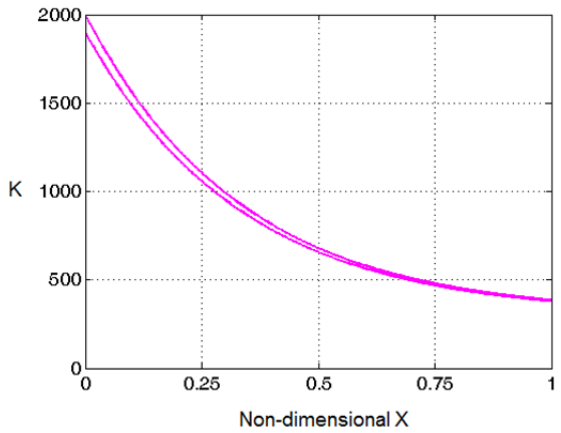

Figure 1 Temperature profile in axial direction of a solar reactor

By observing the temperature decay profile from inlet to outlet of the solar reactor, the reactor temperature profile in the axial direction is approximated by the following relationship assuming that the fluid property didn't change in the radial direction.

$$T_x = T_i + (T_{\max} - T_i) exp(\frac{-nx}{L})$$

The flow supply inlet temperature T_i for all the three flows is 300 °K; the maximum temperature $T_{\max}$ for the main flow is 2000 °K; the shield flows are 1900 °K. The outlet temperature T_L is 380 °K. L is the axial length of the reactor. The attenuation coefficient n is 3 by matching the temperature profile with the reference case. The averaged main flow temperature is 838 °K; the averaged shield flows' temperatures are 807 °K. The average density of each flow is obtained by the equation of state. The reference CFD study used methane as the main flow, argon and hydrogen as the wall and window shield flows. The ideal gas viscosity of the fluids are calculated via the Sutherland's law as

$$\mu = \mu_{ref} \left(\frac{T}{T_{ref}} \right)^{3/2} \frac{T_{ref} + S}{T + S} = \frac{CT^{3/2}}{T + S}$$

μ_{ref} is the reference dynamic viscosity at reference temperature T_{ref} , S is the Sutherland's constant. The coefficients for dynamic viscosities are listed in Table 1.

Gas species	μ_{ref} ($\mu Pa \cdot s$)	T_{ref} (^{o}K)	S	C
Methane	1.20E-5	273.15	197.8	1.25E-6
Argon	5.58E-5	1000	164.2	2.05E-6
Hydrogen	8.35E-6	273.15	84.4	6.61E-7
Air	1.72E-5	273.15	110.4	1.46E-6

Table 1 The Sutherland's coefficients for dynamic viscosities of four gases

Based on the reference CFD study, the boundary conditions of the high temperature solar reactor are calculated and listed in Table 2.

Reference CFD			
Fluid property	Main flow	Wall shield flow	Window shield flow
Gas species	CH_4	Ar	H_2
Molecular weight (g/mol)	16.04	39.95	2.02
Inlet pressure (kPa)	101.325	101.325	101.325
Inlet temperature (K)	300	300	300
Inlet Viscosity (Pa*s)	1.10E-5	2.30E-5	8.94E-6
Inlet Density (kg/m^3)	0.652	1.623	0.082
Max. temperature (K)	2000	1900	1900
Avg. temperature (K)	838	807	807
entrance temperature (K)	385	380	380
Flow rate (LPM)	10	10	1
Mass rate (kg/s)	1.09E-4	2.71E-4	1.37E-6
Inlet Velocity (m/s)	2.947	2.125	0.332
Angular frequency (1/s)	73.7	-	-
Blowing ratio	-	1.80	-
Bulk density (kg/m^3)	0.397	-	-
Mean velocity (m/s)	0.5	-	-
Avg. Reynolds number	545	-	-

Table 2 Fluid property of reference CFD case

For the PIV measurements at room temperature, the experiments are performed at atmospheric pressure and partial vacuum respectively. The gas species of the three flows were replaced by moisture-free air for simplicity. In the atmospheric pressure case, the corresponding fluid properties are estimated as shown in Table 3.

Atmospheric air case			
Fluid property	Main flow	Wall shield flow	Window shield flow
Gas species	Air	Air	Air
Molecular weight (g/mol)	28.97	28.97	28.97
Inlet pressure (kPa)	101.325	101.325	101.325
Inlet temperature (K)	294	294	294
Inlet Viscosity (Pa*s)	1.82E-5	1.82E-5	1.82E-5
Inlet Density (kg/m^3)	1.201	1.201	1.201
Flow rate (LPM)	10	10	1
Velocity in hose (m/s)	21.05	21.05	2.11
Reynolds number in hose	4400	4400	440
Mass rate (kg/s)	2.00E-4	2.00E-4	2.00E-5
Inlet velocity (m/s)	2.95	2.13	0.33
Angular frequency (1/s)	73.7	-	-
Blowing ratio	-	0.72	-
Bulk density (kg/m^3)	1.201	-	-
Mean velocity (m/s)	0.5	-	-
Avg. Reynolds number	4123	-	-

Table 3 Fluid property of atmospheric air case

The size of the gas supply hoses is 0.125 inch. The dynamic pressures of the three flows in the hoses are negligible compared to the static pressure loss which should be taken into account at the outlets of the rotameters. The Reynolds numbers for the main flow and wall shield flow in the hoses are both 4400, large enough to induce turbulence mixing before the flows reach the reactor. However the Reynolds number for the

window shield flow is only 440, therefore a longer hose length was adopted to fully mix the fluid and the tracking particles for PIV measurement. The same strategy is applied in other cases when the flows in the hoses are laminar. It's noticed that the average flow speed here is experimentally obtained via PIV measurement.

In the vacuum case of the PIV experiment, the reactor pressure is reduced to 33.51 kPa in order to match the average fluid density to that in the real reactor. The boundary conditions are listed as shown in Table 4.

Vacuum air case			
Fluid property	Main flow	Wall shield flow	Window shield flow
Gas species	Air	Air	Air
Molecular weight (g/mol)	28.97	28.97	28.97
Inlet pressure (kPa)	33.51	33.51	33.51
Inlet temperature (K)	294	294	294
Inlet Viscosity (Pa*s)	1.82E-5	1.82E-5	1.82E-5
Inlet Density (kg/m^3)	0.397	0.397	0.397
Flow rate (LPM)	10	10	1
Velocity in hose (m/s)	21.05	21.05	2.11
Reynolds number in hose	1460	1460	146
Mass rate (kg/s)	6.61E-5	6.61E-5	6.61E-6
Inlet velocity (m/s)	2.95	2.13	0.33
Angular frequency (1/s)	73.7	-	-
Blowing ratio	-	0.72	-
Bulk density (kg/m^3)	0.397	-	-
Mean velocity (m/s)	0.2	-	-
Avg. Reynolds number	546	-	-

Table 4 Fluid property of vacuum air case

In this case, all the Reynolds numbers in the hoses are not in the turbulent region. In order to enhance the mixing of the fluid and tracking particles, long hoses are used to ensure uniform tracking particle distribution in the flows before entering the reactor. The average flow speed obtained via the PIV measurement is about 40 % of the average flow speed in the reference case. The average kinetic viscosity of the fluid is also about 40 % of that in the reference case. Therefore the average Reynolds number defined as $\rho VD / \mu$, where D is the inner diameter of the reactor, is close to that in the CFD reference case.

The Reynolds number provides an indication of similarity of the flow patterns between the experimental cases and the reference case. Since the dynamic viscosity, μ , is primarily a function of temperature for gas species, a higher Reynolds number in the room temperature model than in the reference case is expected while the average velocity was kept same as that of the reference case. Also, the gas species difference in the reference case providing non-uniform gas species distributions in the real reactor made it difficult to estimate the bulk gas viscosity. But it still provides a quantitative indication to the expected velocity in the PIV experiment. The thermodynamic analysis of the reference case shows that the average Reynolds number of the reference case is 545. In the PIV experiment, the Reynolds number is 4123 in the atmospheric pressure case and 546 in the vacuum case by applying average velocities obtained from the experiments.

In the PSP experiment, only the wall shield flow gas is replaced by CO_2 to simulate the wall shield flow made of heavy gas species. The other two flows are made of air for simplicity. The experiment is conducted at steady atmospheric pressure to avoid pressure variation. The calibration intensity fields are established specifically for each experimental measurement. The boundary conditions and flow properties are calculated as shown in Table 5.

Atmospheric mixture case			
Fluid property	Main flow	Wall shield flow	Window shield flow
Gas species	Air	CO_2	Air
Molecular weight (g/mol)	28.97	44.01	28.97
Inlet pressure (kPa)	101.3	101.3	101.3
Inlet temperature (K)	294	294	294
Inlet Viscosity (Pa*s)	1.82E-5	1.47E-5	1.82E-5
Inlet Density (kg/m^3)	1.200	1.823	1.200
Flow rate (LPM)	10	10	1
Velocity in hose (m/s)	21.05	21.05	2.11
Reynolds number in hose	4400	8300	441
Mass rate (kg/s)	2.00E-4	3.04E-4	2.00E-5
Inlet velocity (m/s)	2.95	2.13	0.33
Angular frequency (1/s)	73.7	-	-
Blowing ratio	-	1.10	-
Bulk density (kg/m^3)	1.496	-	-

Table 5 Fluid property of atmospheric mixture case

3.2.2 Ekman analysis

Because the vortex created by the main flow is rotational due to the existence of fluid viscosity, the Coriolis term along with the viscous term in the momentum equation causes the Ekman layer, a friction affected layer similar to the boundary layer in a non-

rotating fluid. At the beginning of the vortex flow, the shear force between the Ekman layer and the stationary fluid drive the fluid adjacent to the boundary layer to accelerate. According to the jet direction of the main flow, the Coriolis term created by the vortex causes a radial outward secondary flow. Therefore in additional to the primary circulation by the main flow vortex, a secondary circulation where flow near the entrance zone is driven radially outward, upon reaching the inner wall the flow turns upward by 90 degrees along the inner wall, then turns radially toward the axis and finally merges in axial direction to close the circulation as observed in the experiment at the initial stage of the vortex flow. In order to quantify the effect of the Ekman layer, the Ekman analysis is derived by a steady, incompressible, homogenous horizontal flow, the momentum equation is expressed as

$$\upsilon_z \frac{\partial^2 \bar{u}}{\partial z^2} + f\bar{v} = 0$$

$$\upsilon_z \frac{\partial^2 \bar{v}}{\partial z^2} - f\bar{u} = 0$$

f is the Coriolis coefficient; ν_z is the vertical turbulent viscosity. The Ekman number is defined as the ratio of the viscous term to the Coriolis term in the form of $E_k = \nu / \omega L^2$, where ν is the turbulent viscosity, ω is the angular frequency of the main flow at the entrance zone, L is a characteristic length scale namely the axial length of the reactor. Since L and ω are kept constant, the Ekman number is a function of turbulent viscosity.

For example, in the vacuum case, the length scale of the reactor is 0.2 m, the angular frequency is 73.7 Hz by applying the fluid condition at the entrance zone, the turbulent viscosity is 4.58×10^{-5}, therefore the corresponding Ekman number is 1.6×10^{-5}. The Ekman layer thickness defined as $\delta=\sqrt{E_k}L$ is 7.9×10^{-4} m. The calculated values for the rest of cases are shown in Table 6:

CASE	ν (m2/s)	E_k	δ (m)
Reference CFD	1.15E-4	3.9E-5	1.2E-3
Atmospheric air	1.52E-5	5.2E-6	4.5E-4
Atmospheric air-CO2 mix	1.18E-5	4.0E-6	4.0E-4
Vacuum air	4.58E-5	1.6E-5	7.9E-4
Vacuum air-CO2 mix	3.57E-5	1.2E-5	7.0E-4

Table 6 Ekman number and Ekman layer thickness in different cases

Between the above cases the variation of Ekman number is about within one order, and so for the Ekman layer thickness. A very small Ekman number indicates that the flow is significantly affected by Coriolis Effect. Radial secondary circulation dominates within the layer with magnitude proportional to the angular velocity difference between the main flow and the viscosity-affected adjacent fluid. It's expected that the Ekman number at the conical part is larger than at the entrance of reactor as the fluid reaches the exit of the reactor. In radial direction, when the Coriolis Effect generated from the vortex takes significant effect on the fluid, the effect further enhances near the axis since the fluid speed is higher due to the conservation of angular momentum. It's noticed that during the initial stage of the vortex flow forming, the merged secondary flow in axial direction

might carry the particles toward the reactor window and cause particle deposition on the window surface. The existence of the secondary flow is also a proof of radial pressure gradient, which further enhances the radial and axial components in this flow structure.

3.3 Particle image velocimetry (PIV)

3.3.1 Overview

Particle image velocimetry (PIV) shown in Figure 2 is an instantaneous, non-intrusive, whole field measurement. It relies on optical access for a light sheet and the scattering light from the tracking particles to a camera to capture the Eulerian velocity of the particles.

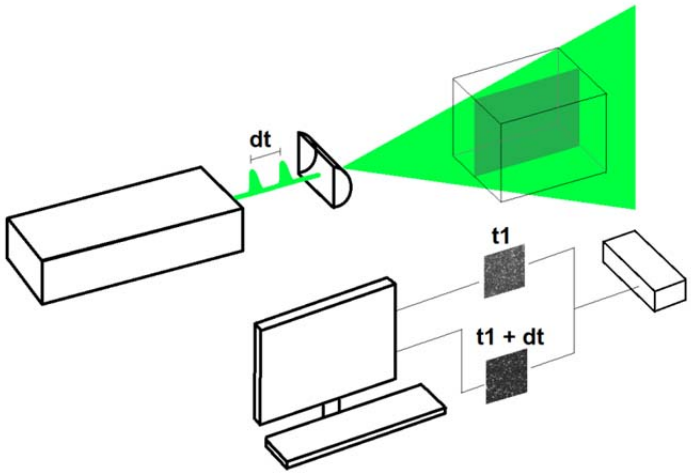

Figure 2 A 2-dimensional PIV system

The tracking particles are decently seeded by a fluidized bed or an atomizer. Generally, the size distribution of the particles, d_p, is uniform and small enough to minimize the velocity lag while traveling with the fluid. The particle distribution in the flow field should be kept homogeneous to increase the signal-to-noise ratio (SNR) and robustness of the image quality. The images captured by the digital camera record the positions of the tracking particles in form of gray scale intensity field, $I(i, j)$. The particle velocity vectors are calculated from the simple equation below.

$$\overrightarrow{V_p} = \frac{\Delta \overrightarrow{X_p}}{M \Delta t}$$

$\vec{V}_p$ represents the particle velocity vector; $\Delta \overrightarrow{X_p}$ is the straight-line displacement of a particle on the image plane between two consecutive frames; M is the magnification factor; Δt is the time interval between two consecutive frames referred to an image pair. The particle displacement is calculated by the intensity field cross-correlation

$$R(k,l) = \frac{\sum_{i=1}^{N_X}\sum_{j=1}^{N_Y}\left(I_a(i,j) - \bar{I}_a\right)\left(I_b(i+k, j+l) - \bar{I}_b\right)}{\left[\sum_{i=1}^{N_X}\sum_{j=1}^{N_Y}\left(I_a(i,j) - \bar{I}_a\right)^2 \sum_{i=1}^{N_X}\sum_{j=1}^{N_Y}\left(I_b(i+k, j+l) - \bar{I}_b\right)^2\right]^{1/2}}$$

$$\bar{I}_a = \frac{1}{N_X N_Y} \sum_{i=1}^{N_X} \sum_{j=1}^{N_Y} I_a(i, j)$$

Subscripts ‘a’ and ‘b’ represent the consecutive frame A and frame B. (i, j) represents the centroid position of the particle images on the image plane. Number N represents the particle images number in the area of interest. The direct $N \times N$ 2-D cross-correlation can be processed faster by the fast Fourier transform (FFT) which lowers the processing time from scale of N^4 to $N^2 \log_2 N$. Typically, a captured frame image is divided into interrogation spots, namely the sub-grids images for correlation to increase the spatial resolution of the velocity vector field. Since the displacement, $\Delta \overrightarrow{X_p}$, implies the loss of the curvature information, a small interrogation spot can mitigate the intrinsic defect.

3.3.2 Laser

A laser contains a pumping source to provide photon, a gain-medium to generate radiation of specific wavelength, and an optical cavity to produce coherent light. The laser adopted in the PIV experiment is a Nd: YAG double pulsed laser with maximum 120 mJ per pulse as shown in Figure 3. It’s a multimode, water-cooled laser system. The beam wavelength is 532 nm; the maximum pulse rate for each cavity is 15 Hz. The laser is powered by a 95 - 240 VAC 50/60 Hz electric power supply. The emitting power level is controlled by Q-switch according to a specific gain-to-time relation. The output beam

profile is a Gaussian distribution. In our application, the pulse power of each laser can be adjusted respectively by the Q-switch from external software interface.

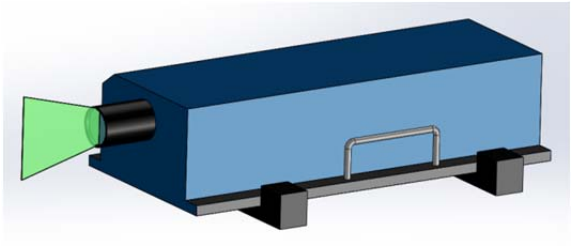

Figure 3 532 nm Nd-YAG double pulsed solid-state laser with light sheet optics

According to the specification sheet, the beam pulse width is less than 6 ns; the divergence less than 3 mrad; the beam pointing stability is less than 100 μrad. The beam output quality is shown in Figure 4 and Figure 5.

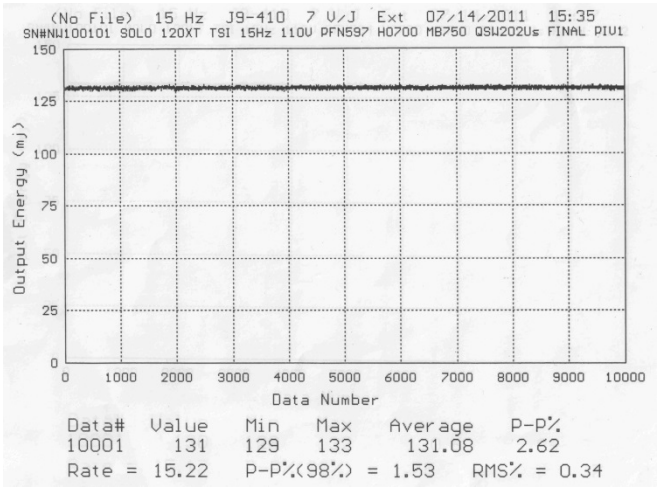

(a)

Figure 4 Laser output energy test result (a) Laser A (b) Laser B

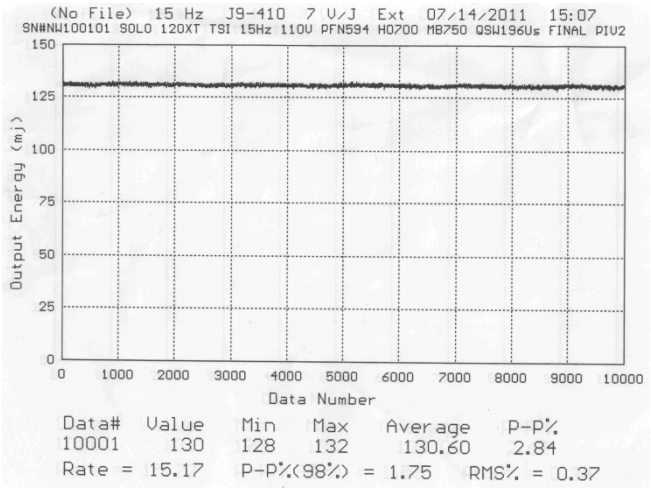

(b)

Figure 4 Continued

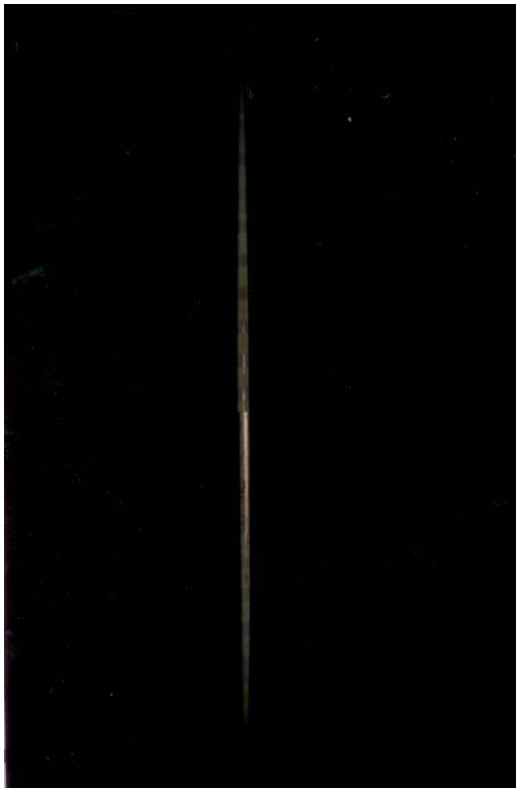

Figure 5 Light sheet alignment burn test result

3.3.3 Camera

The camera of the PIV system is a POWERVIEW PLUS 4MP model made by TSI Inc. The recording CCD resolution is 2048 x 2048 pixels with 12-bit intensity dynamic range, noise reduction and maximum frame rate of 15 Hz. A 532 ± 10 narrow band-pass filter is mounted on the camera lens to eliminate the background noise from the environment light sources. The camera is also equipped with the capability to be synchronized with the laser pulses to operate on straddle mode, which allows two pulses to straddle the inter-frame time between two exposures with short exposure time below 200 ns. The camera is capable to operate solely for 2-D measurement or cooperate with another image grabber in 3-D stereo measurement.

3.3.4 Synchronizer

The entire triggering process during the PIV measurement is controlled by the external synchronizer model 610036 made by TSI Inc. The synchronizer can control up to eight devices with external trigger TTL input and USB communication via a serial interface. The signals of the laser flash lamps, Q-switches, camera exposure and frame time interval are generated and synchronized for the software interface control. The time interval between two laser pulses, which is directly related to the particle displacement, is one of the most important parameters for the PIV measurement.

3.3.5 Optical analysis

The PIV system uses a lens set including a cylindrical lens with -15/-25 mm focal length options and a spherical lens with 500/1000 mm focal length options to generate the light sheet. The cylindrical lens spreads the laser beam into a vertical light sheet with specific divergence rate according to the focal length of the lens. The spherical lens converge the light sheet horizontally to maintain a thin sheet of high intensity. In optical lens alignment, especially for applications of using high power laser such as Nd : YAG pulsed laser, a diverging lens should be mounted at the first stage of the lens set to avoid the laser beam from focusing at a point in space which may cause ionization of the medium or the surrounding air. The selection of each lens also depends on the dimensions of measuring volume and other experimental considerations, for example both the -15 and -25 mm cylindrical lens can be used at the same time to reduce the non-uniform intensity distribution across the light sheet. The focal length of the spherical lens here is 500 mm, which is the distance between the lens set of the laser to the measuring platform.

The optical resolution of a PIV system is intrinsically limited by the diffraction limit, even with an aberration-free lens. According to Huygens-Fresnel principle (1816), every spatial portion of the light across a finite-sized lens surface is considered as a point source and thus sum up to specific interference patterns namely airy function due to different propagating paths from the lens to the image focal place. When the scattering

light from a particle passes through a lens and projects on the image plane, the diffraction limit defined as the diameter of the central bright dot detectable by the camera, namely d_{diff}, is expressed as

$$d_{diff} = 2.44(1+M) f^{\#} \lambda$$

$f^{\#}$ is the F-number, M is the magnification factor, λ is the wavelength of light. Practically, it gives an order of 10 μm as the limit of spatial resolution to the current PIV measurements. In the experiment, the physical field of view is 146 mm, the CCD size is 15.15 mm with 2048 x 2048 pixels. Therefore the magnification factor is 0.104. The diffraction limit is 11.5 μm when the F-number is equal to 8.

The depth of field, δ_z, refers to a distance range within which the edge of an object on the image plane is sharp and in focus. It affects the positioning of the particle image, especially in region away from the center of the image. It's a result of optic setting between the object distance, the focal length and the F-number, which can be defined as

$$\delta_z = 4(1+\frac{1}{M})^2 f^{\#2} \lambda$$

A narrow depth of field δ_z ensures the captured motions of the particles to be right in the light sheet 2-D plane, but this also tends to increase the signal loss and background noise due to loss of particle pairs. In contrast, a large depth of field gives better focus on the particles images across the light sheet plane, especially when a misalignment exists between the light sheet and the camera due to instrumentation uncertainty or light distortion as the light sheet passes through material interfaces. Although it causes velocity averaging in the direction normal to the light sheet plane, a large field of depth is preferred in conventional PIV measurements for its alignment tolerance and applicability. It's seen that the diffraction diameter can be decreased by decreasing the F-number, but this will also decrease the depth of field. It's also seen that when the distance between the camera and the measuring volume is decreased, the diffraction limit will increase, and depth of field will decrease. When the depth of field is set by the experimental setup, the diffraction limit is determined. Therefore, one should put the camera with F-number set to around 8 starting from a certain distance away from the measuring volume and pull the camera gradually toward to measuring volume while keeping well focus across the image till obtaining large enough particle image.

When the effects of diffraction limit and the resolution of the recording medium are considered, the particle image diameter on the recording medium can be expressed as

$$d_\tau = \sqrt{\left(Md_p\right)^2 + d_{diff}^2 + d_r^2}$$

d_r denotes the pixel resolution of the recording CCD and is equal to 7.4 μm in this application. It is involved with the particle image size on the image plane, for example, the particle image diameter approximate to d_r while the system is not diffraction-limit dominated and using extremely small tracking particles. The particle image diameter d_τ is an important parameter because the uncertainty tends to decrease with smaller d_τ, and the average intensity of particle image is proportional to d_p^2.

When applying a particle into the flow field, the particle size must be small enough to follow the flow quickly while keeping a cross-section area large enough to scatter light toward the image grabber. In general, the optimal size of the particle image should be larger than 1-2 pixels on the image plane to avoid Nyquist under-sampling and peak locking. Thus an empirical value of particle diameter ranging 1 to 10 micron will gives better results. It's found that in most of the conventional PIV measurements for gas flows, the particle image is dominated by the diffraction limit. In this application the liquid tracking particle size is 1 μm, the diffraction limit d_{diff} is 11.5 μm, the combined particle image size d_τ is 13.6 μm, which is about 1.84 times of the pixel size.

The spatial resolution of the PIV is proportional to the resolution of the camera in terms of the dynamic velocity range (DVR) and the dynamic spatial range (DSR) proposed by Adrian (1997). These two parameters under a fixed PIV optical setup are constants quantifying the maximum optical capability of measuring a flow field. The former is

defined as the ratio of the maximum measurable velocity under fixed experimental setup to the minimum resolvable velocity as

$$DVR \equiv u_{p\max} / \sigma_u$$

σ_u can be replaced by $\sigma_{\Delta X} / M\Delta t$, where $\sigma_{\Delta X}$ is the uncertainty of centroid displacement of the particle image. Typically, $\sigma_{\Delta X}$ can be further related to the particle image in the form of $c_\tau d_\tau$, where c_τ is a sub-pixel error factor usually less than 10 %. It's noticed that when the size of a particle image is too small compared to the pixel size, for example the nano scale carbon particles, the particle image will occupy only 1 pixel on the image plane and thus lead to integer position in the coordinate called peak locking. The sub-pixel error factor will become unity. The relationship between the particle image and the DVR under different F-number is shown in Figure 6.

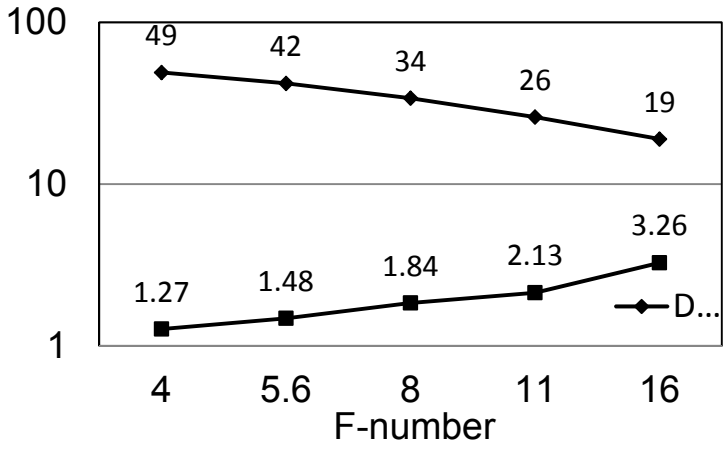

Figure 6 Relation between particle image size and DVR under different F-number

The dynamic spatial range is defined as the ratio of the dimension of the physical field to the minimum observable physical length scale as

$$DSR = L_x / \Delta x_{\max}$$

The DVR and DSR under different time intervals are shown in Figure. 7

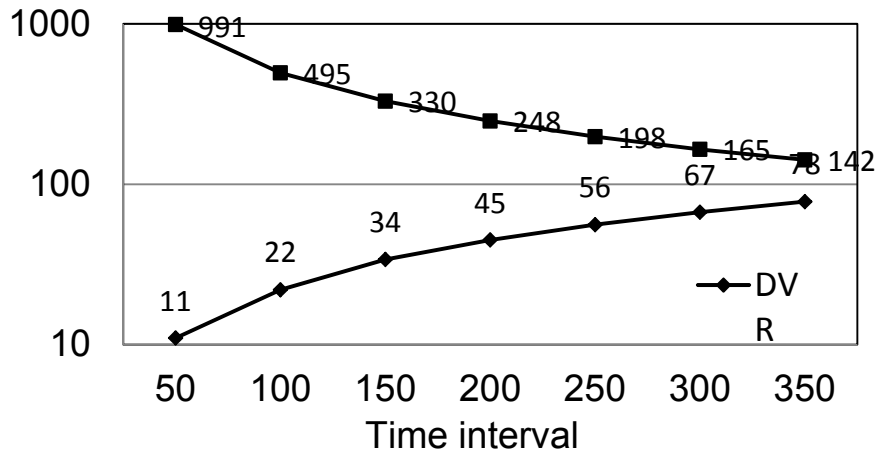

Figure 7 Relation between DVR and DSR under different time interval

A reciprocal relationship between the DVR and DSR under a fixed optical setup can be found to be

$$DVR \times DSR = \frac{L_X}{c_\tau d_\tau}$$

L_X represents the capacity of the system to carry the flow information; c_τ is a measure of the algorithm accuracy during image processing; d_τ indicates the performance of the optics. An optimal value for DVR can be determined by following the one-quarter rule.

According to the parametric analysis, the DVR under the experimental setup in this study is 34 while using the F-number to be 8, the corresponding DSR is 330. The theoretical optimal DVR when c_τ equal to 2 is 36 with an optimal F-number equal to 10, the optimal DSR is 256. The choice of available F-number between 8 and 11 is made according to the dimension of the field of view. When the F-number is 8, the optimal field dimension is 36 mm; when the F-number is equal to 11, the optimal field capacity is 470 mm. Since the diameter of the reactor model is 125 mm, the F-number of 8 was selected to avoid larger diffraction limit diameter on the image plane and to accommodate more light information within an acceptable field of depth.

3.3.6 Tracking particle

Since a high quality PIV image relies on obtaining particle images of sharp particle edges and homogeneous distribution, several theoretical and empirical parameters were developed to be considered to ensure optimal image quality under a fixed measurement setup.

Due to the existence of diffraction limit, a tracking particle with diameter smaller than the diffraction limit will result in a particle image larger than the physical size of the particle, which implies that the particle images on the image plane could overlap when the particles in the light sheet plane are close enough to each other. Therefore the source density N_S defined as the number of particles within a volume projected from a particle image back to the physical space should follow the criteria as

$$N_S = C\Delta z \frac{\pi d_\tau^2}{4M^2} \ll 1$$

In order to minimize the particle image overlap, the concentration of the tracking particles should be kept below a certain threshold by physically diluting the particle smoke or powder with a particle-free fluid, usually air or water before entering the measuring volume. According to previous optical analysis, the optimal particle images diameter should be kept at least 1-2 times of the CCD pixel size. This is also the reason that 1 μm diameter of tracking particle is small enough in most of the current PIV measurements.

When a sparse particle distribution in the flow field is obtained, a low signal-to-noise ratio (SNR) may occur if the particles numbers is insufficient in a relatively small interrogation spot during correlation. Therefore a larger interrogation spot size is required to include enough particle images to maintain an acceptable SNR value. The

criteria for the image density defined as the number of particle images within an interrogation spot is expressed as

$$N_I = C\Delta z \frac{D_i^2}{M^2} \gg 1$$

In most of the conventional PIV measurements, the image density should be at least 10 to hold a good SNR on the correlation map. It's worthy of notice that in turbulence measurements, the length scale of the turbulence is the Kolmogorov scale, which is too small to be resolved by the current conventional PIV systems due to the diffraction limit of lens.

The tracking fidelity of the seeded particles in fluid is evaluated by using Stokes flow theorem, now known as Stokes' Law to describe the motion of a single homogeneous spherical body suspended in a continuous viscous fluid with a very small particle Reynolds number. The equation of particle motion neglecting non-linear drag and vorticity diffusion can be expressed as

$$m_p \frac{d\overrightarrow{u_p}}{dt} = 3\pi\mu d_p(\overrightarrow{u_f} - \overrightarrow{u_p}) - \frac{1}{2} m_f \left[\frac{d\overrightarrow{u_p}}{dt} - \frac{d\overrightarrow{u_f}}{dt} \right] + m_f \frac{d\overrightarrow{u_f}}{dt} - m_p \left(1 - \frac{1}{\gamma} \right) \vec{g}$$

The first term on the right represents the viscous drag; the second term is the added mass effect, namely the force exerted on the particle by the periphery fluid derived by Auton et al. (1988); the third term is the force exerted on the particle by the fluid displaced by the particle; the last is the body force effect. γ is the density ratio of tracking particle to the fluid. Since the purpose of particle tracking analysis is to evaluate how well the seeding particles can track the fluid, considering the equation is viscous drag dominant, the response time can be expressed in a simple form as result of the first-order differential equation

$$\tau_p = \frac{\rho_p d_p^2}{18\mu}$$

τ_p is also called characteristic time or time constant. It is a measure of capability of the tracking particles to follow the fluid. When taking the body force effect into consideration, the terminal velocity difference can be further expressed as

$$(\overrightarrow{u_p} - \overrightarrow{u_f})_{t\to\infty} = (1-\gamma^{-1})\vec{g}\tau_p$$

According to the above expressions, the velocity lag of the tracking particles can be reduced by selecting a smaller particle diameter or a density ratio close to unity. However, in most cases the particle property is subjected to the experimental limitations.

The response time τ_p should be small enough to follow the smallest turbulent disturbance of interest. In order to relate the response time of the particle to fluid disturbance, the fluid velocity can be conceptually represented as sum of harmonic functions $u_f = u_f(\omega)$, where ω is the angular frequency of the flow oscillation. Providing the fluid and particle properties can be evaluated, then the Stokes number defined by the ratio of response times between the particle and fluid disturbance can be expressed as

$$St = \frac{\tau_p}{\tau_f} = \frac{\rho_p d_p^2 \omega}{18\mu}$$

When the effect of vorticity diffusion proposed by Basset (1888) is considered, Mei et al. (1996) defined the Stokes number in form of $St = \sqrt{\omega d_p^2 / 8\nu}$, a response function of the tracking particle to the fluid was derived as a function of the density ratio γ only as

$$\eta = \left\{ \frac{(1+St)^2 + (St + \frac{2}{3}St^2)^2}{(1+St)^2 + \left[St + \frac{2}{3}St^2 + \frac{4}{9}(\gamma - 1)St^2 \right]^2} \right\}^{1/2}$$

The resulting amplitude ratio versus Stokes number is shown in Figure 8.

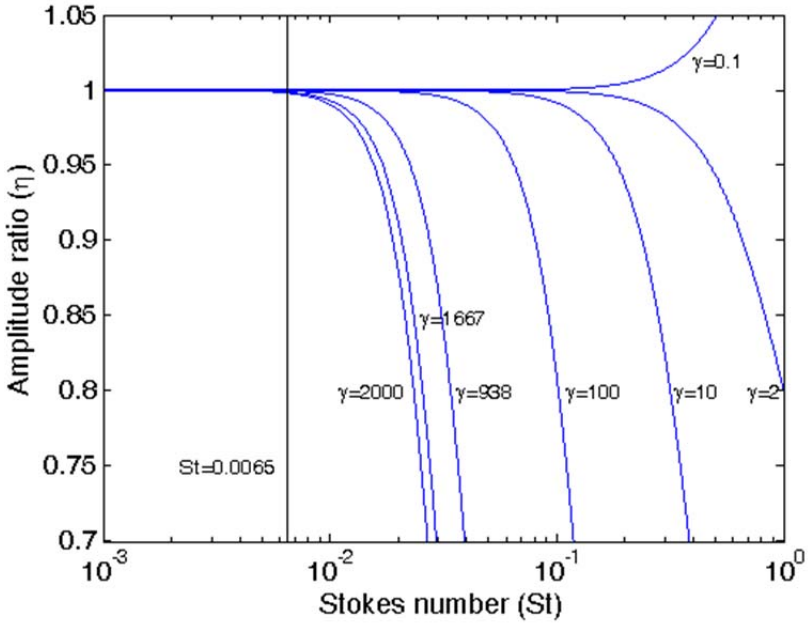

Figure 8 Stokes number vs. amplitude ratio at different density ratio

For $St \ll 1$, the particle can track the fluid with amplitude ratio η of approximately unity. When the Stokes number increases, for $\gamma > 1$, the amplitude ratio decreases and thus the particles act as a low-pass filter as shown; for $\gamma < 1$, the particles tend to over-react to the fluid disturbance.

For 1 μm tracking particles made of tri-ethylene glycol (TEG), the corresponding Stokes number is 0.0065. The liquid density is 1125 kg/m^3, thus the density ratio of the particle to the fluid is 938. The resulting amplitude response is above 99.9 %. In order to prevent low pass filtering and over-shoot behavior of the particle, a reasonable cut-off limit of ± 3 dB energy response is defined. Based on the cut-off criteria, the corresponding cut-off

Stokes number is 0.049; the cut-off frequency is 46.44 kHz; the maximum cut-off particle diameter is 7.62 μm.

For 50 nm tracking particles made of carbon (SUPER-P), the particle density is 2000 kg/m^3, the specific heat is 650 J/kg-K, the thermal conductivity is 165 W/m-K. The Stokes number is 0.0003 and higher since the particles tend to agglomerate due to existence of humidity and static charge. In the experiment the particles are dried and injected at the downstream of the rotameters. The density ratio of carbon to the fluid is 1667. The amplitude ratio is 1. The cut-off Stokes number is 0.037; the cut-off frequency is 10.42 MHz. The maximum cut-off particle diameter is 5.69 μm. By comparison it's shown that the carbon particle can track the fluid with velocity lag an order smaller than the TEG particles do.

The cut-off eddy diameter is a measure to check how well the particles will follow turbulent eddies under the limitation of spatial resolution of the PIV system. According to the experimental setup, the minimum characteristic lengths or eddy diameters under which the particles can follow the fluid with an amplitude ratio no less than 0.707 are 20 μm for the TEG particles and 90 nm for the Carbon particles. Compared to the spatial resolution of a single CCD pixel with a projected physical field size of 71.3 μm, both the tracking particles are synchronized with the fluid at the maximum spatial resolution of the PIV camera.

The minimum detectable eddies can be defined in different ways when considering the spatial resolution of the CCD along with the overlapping percentage of the interrogation spots. For example, an eddy may straddle on two adjacent interrogation spots with different vector directions on each spot. When 50 % spot overlapping is applied, the smallest detectable eddy in the vector field is half the spot size. According to the experimental setup, the minimum eddy detectable by the PIV system is more than 56 times of the cut-off eddy size for the TEG particles, which ensures the robustness of the eddy velocity vectors on the image plane.

3.3.7 Traverse

The traverse platform creates a sub-coordinate system on the optical table to allow a maximum of 120 mm off-axial displacement with finer positioning. The dimension of the traverse is 300 mm × 341 mm × 12.7 mm with fine position adjustment using hex key socket and position locking screw.

3.3.8 PIV Software

3.3.8.1 Overview

The selection of algorithms is the most critical part, beside the tracking particle, to the result of PIV measurement. The software adopted was INSIGHT-4G programmed by TSI Inc. The software is able to process large numbers of frame pairs and generate vector fields via several correlation algorithms depending on the internal RAM capacity. The software is also able to generate vortices and turbulence intensity contour via TECPLOT add-on components.

3.3.8.2 Interrogation spot

In generation of the interrogation spots, every interrogation spot is partially overlapped with the adjacent spots in order to increase data yield by retrieving the pair loss in the adjacent spots. A 50 % overlapping is sufficient and is adopted as the default setting. Because the 2-D cross-correlation is processed via FFT which assumes the data within the interrogation spot to be periodic, the Nyquist theorem applies to the selection of interrogation spot size. Thus particle displacement should not exceed half of the spot size to avoid Nyquist noise generated on the correlation map.

Also, when the particles travel too fast within a relatively small interrogation spot, the large displacements cause the in-plane loss of particle pairs in the cross-correlation. The same issue occurs in the direction of light sheet thickness called out-of-plane loss. In order to reduce pair loss of the in-plane and out-of-plane motions, practically the particle displacement should be controlled not exceeding 1/4 of the spot size and of the light sheet thickness, which is referred to the one-quarter rule. However, the one-quarter rule leads to a coarse spatial resolution when the particle velocity is high. The multi-pass interrogation spot can be applied to compensate the insufficient spatial resolution due to obeying the one-quarter rule. It can start with a coarse spot size to determine a coarse velocity vector field in the first pass. In the subsequent pass, a smaller interrogation spot size is used to correlate with the destination spot via a vector offset obtain from the previous pass. In this research, the recursive-Nyquist spot engine was adopted to accommodate large particle velocity with high spatial resolution, the interrogation spot size started from 64 pixels to 32 pixels.

3.3.8.3 Spot weighting mask

When a velocity gradient exists within an interrogation spot, the faster particles, especially those near the edge of the interrogation spot, are more likely to cause in-plane loss than the slower ones. Therefore the correlation tends to bias toward the lower particle velocities due to pair loss of the faster ones. In order to minimize the velocity

bias, a weighting mask is applied to the interrogation spot to weight the particle at the center of the spot more than those near the edges before correlation so that the bias due to the information loss of the faster particle pairs near the edge is mitigated. In practice, the velocity difference in an interrogation spot should be controlled below 5 %. In this research a Gaussian mask was applied under existence of the velocity gradient.

3.3.8.4 Sub-pixel estimator

In practice, the particle image size should be at least 1-2 pixels to avoid peak locking and to obtain sub-pixel accuracy. On the correlation map, a peak weighting profile is applied to the signal peak along with its adjacent pixel values to determine the particle displacement to sub-pixel level. The profile can be a 3-point or 5-point function in each dimension. In general, the accuracy of the particle displacement is up to 0.1 pixel proposed by Willert et. al. (1991) compared to the accuracy of integral number of pixel before. Therefore, the final signal peak is a combined accuracy of a cross-correlation and a peak estimator, which produce an SNR value stronger than the second highest peak constructed by noise and wrong pairing. The empirical SNR value equal to 1.5 was called SNR threshold value to determine whether a signal peak was robust or not. In this research a Gaussian 3-point peak finder was used in X and Y direction respectively on the 2-D correlation plane, the SNR was set to 1.4. The sub-pixel displacement ε is expressed as

$$\varepsilon = \frac{\ln R_{-1} - \ln R_{+1}}{2\ln R_{-1} + \ln R_{+1} - 2\ln R_0}$$

The subscript of R represents the position of correlation values R around the correlation peak R_0 .

3.3.8.5 Pre-processing

The background light fluctuation and out–of –focus particles in the flow also introduced noise. In order to get a higher SNR peak on the correlation plane, the minimum intensity field was obtained by ensemble statistics and then subtracted from each interrogation spot. It's only available when multiple pairs of frames are processed at the same time because of its statistic nature. By doing so, the second highest peak due to wrong pairing is minimized.

3.3.8.6 Post-processing

A post-process is required in most PIV measurements. The two most common methods are vector validation and vector conditioning. The vector validation compares a vector to its neighborhood vectors to exam the robustness of the vector by mean comparison or median comparison. It could also be applied to the whole field scale if the range of

velocity is known. By doing this, the vector fluctuations, such as the small scale turbulences and shocks in the velocity field, were smoothed. The vector conditioning method interpolates vectors to fill the region where vector are unavailable. It can also be used to replace the original vector failed in previous vector validation. Since the vector conditioning is considered a method that inherently increases bias, the process could be placed in post-processing but shouldn't be performed more than one time in the entire image process stream, especially in highly turbulent flow fields. In this research only global vector validation was adopted during post-processing. No vector conditioning was used.

3.4 Flow control

The flow parameters are controlled by a continuous monitoring system including compressed gas sources, pressure regulators, pressure gauges, pressure transducers, T–type thermocouples, rotameters, particle filter and a single phase vacuum pump as shown in Figure 9, Figure 10 and Figure 11. The real-time electronic signals of the pressure and temperature are acquired and logged using LABVIEW instrumentation interface shown in Figure 12. The operating pressure volume flow rates are controlled manually according to the self–correction outputs from the LABVIEW monitoring interface.

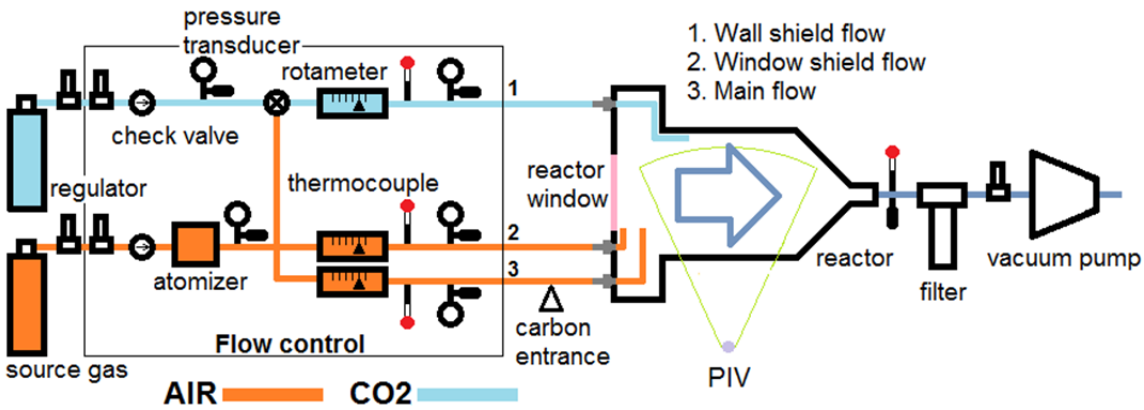

Figure 9 Schematic of flow control

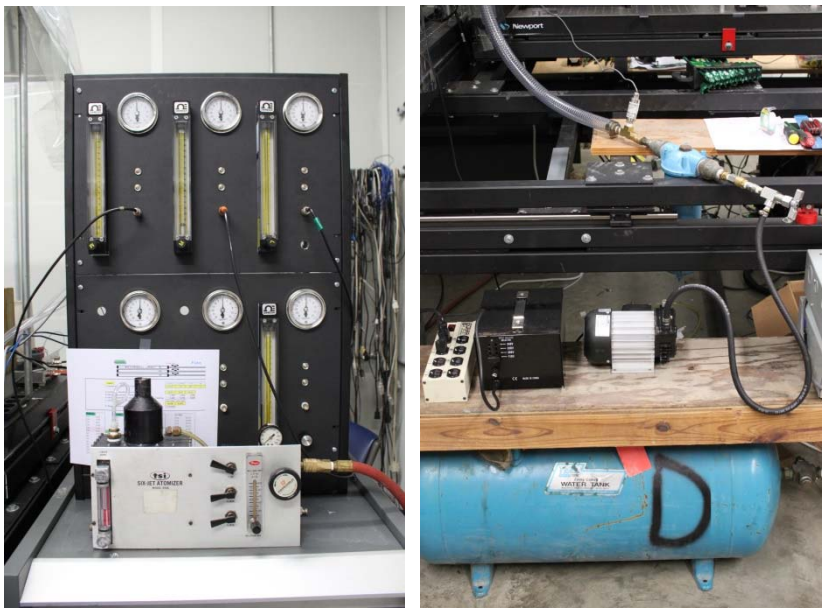

(a) (b)

Figure 10 Flow control (a) Up-stream (b) Down-stream

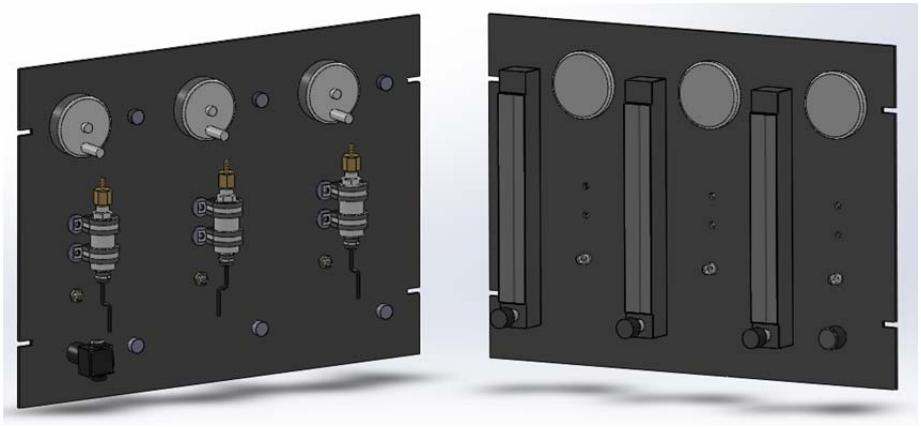

Figure 11 Flow control panel

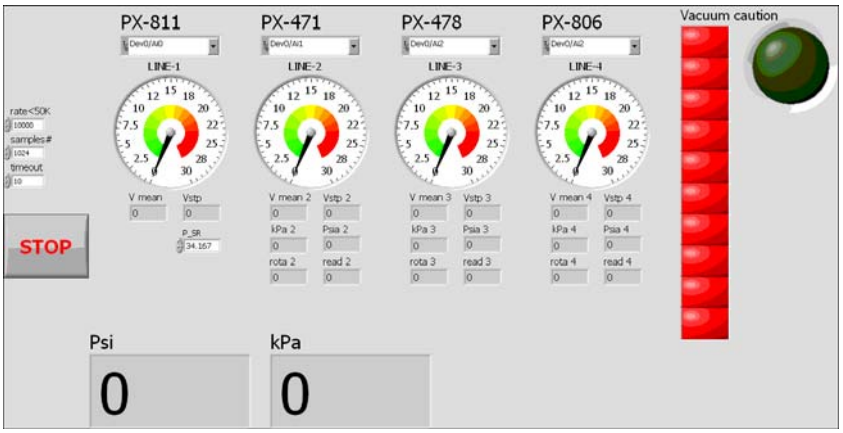

Figure 12 LABVIEW flow monitoring interface

The OMEGA 150 mm high accuracy rotameters for measuring the gas flow rate must be calibrated if the pressure and gas species are different from air at standard pressure and temperature. The volumetric rates of non-air species at pressures deviated from atmospheric pressure are converted to air volumetric rates at the standard pressure and

temperature. The rotameters for gas service use a capacity rating based on air at STP (20° C, 1 atm) condition. The gas correction factor is used to convert the service gas to equivalent STP air flow rate readings in rotameters when using a gas other than air at STP condition. The equivalent air flow rate of a working gas can be calculated by the following equation:

$$\dot{V}_{equiv.air} = \left[\dot{V} \times \frac{P}{P_{STP}} \times \frac{T_{STP}}{T} \right] \times \left[\frac{SG}{SG_{air@STP}} \times \frac{T}{T_{STP}} \times \frac{P_{STP}}{P + P_{loss}} \right]^{1/2}$$

The first bracket shows the flow rate converted from working condition to STP condition; the second bracket determines the gas correction factor. The pressure drop between the pressure sensors to the measuring volume at downstream is considered.

The OMEGA PX-209 pressure transducers with the measuring range from 0 to 30 psia are calibrated by dead weight test to obtain a linear relation between the input pressure P and the output voltage V in form of $P = aV + b$, where a and b are constants for a specific transducer. The thermal-couples are calibrated by an extension wire as a reference of ambient temperature.

The blowing ratio is defined as the momentum ratio between the wall-shield flow and the main flow. A large blowing ratio represents stronger vertical momentum along the inner wall compared to the momentum of the main flow, vice versa. In the high

temperature simulation the blowing ratio is 1.80. In order to obtain velocity vectors with correct momentum interaction between the main and wall shield flows, the blowing ratio in the room temperature experiment should be kept as close to that of the reference case as possible. Here the momentum ratios between the window shield flow and the other two flows are negligible since the momentum level of the window shield flow is less than 2 % of the other two flows.

According to the thermodynamics analysis, the bulk density in the high temperature simulation is 0.397 kg/m^3. The density of the solid carbon generated from the dissociation reaction is estimated as the density of activated carbon equal to 2000 kg/m^3. Since there's a density difference between the carbon particles and the fluid in the high temperature reactor, the two phase flow effect needs to be taken into account. In order to obtain the same trajectory information of the carbon particles under the two-phase flow effect in the room temperature measurement, the bulk density in the vacuum case is kept same as that in the high temperature case. The fluid dynamics is obtained by using liquid TEG tracking particles to eliminate velocity lag.

In order to reduce the operating pressure in the vacuum cases, a REPUBLIC single phase 220 VAC/50 Hz vacuum pump is installed downstream of the reactor model to control the fluid density. Air is used in the room temperature measurement instead of helium, hydrogen and argon in the real reactor.

The TEG tracking particles are generated by a TSI six-jet atomizer. When starting generation of the particles, the liquid is sucked into a siphon tube and blown by an intersecting air jet. The liquid carried by the air stream impinges on an impacter downstream and breaks into a particle fog containing droplets of various sizes from dozens of microns to about 1 μm. Near the top exit of the atomizer, the droplets of large sizes are filtered off by gravity. Another air stream meets the particle fog near the top exit of the atomizer, dilutes the fog to a decent particle concentration and blows the finest droplets toward the outlet, making the air flow full of the tracking particles. The final diameter of the particles is about 1 μm, which is a suitable size for this application. The seeding amount is proportional to the inlet pressure controlled by the inlet regulator. At a fixed diluting air stream flow rate, the concentration of the tracking particle is proportional to the jet number. Here the inlet pressure is set to 25 psig and the jet number is 2 determined by empirical observation to reach the optimal seeding condition.

The solid carbon particle is dried and injected into the flow using a vibrating syringe. The feeding rate of injection is manually controlled by the valid velocity vector percentage on the image plane.

In the flow control system, the seeded air flow is firstly branched into 3 flows to represents the main flow, the wall shield flow and the window shield flow. The flows are directed into three rotameters respectively. Due to the two phase mixture of the seeded flow, the rotameters become clogged by the seeded fluid in 3-5 minutes after continuous

operation, thus a periodical flow tube purging is required to prevent the rotameters from getting clogged at higher volumetric flow rates. After passing the rotameters, the temperature and pressure of the three flows are measured to determine the mass flow rates according to equation of state.

3.5 Perspective calibration

The robustness of a PIV measurement heavily depends upon the finesse of the calibration process. In order to determine physical displacement of particles from the image plane, a transform function $\vec{X} = H\vec{x}$ is required to convert position on the image plane back to the corresponding position in the physical space. In a distortion-free flow field, the magnification factors between the two domains can be obtained easily. In most of cases, however, light distortions occur when the light sheet is warped by the material interfaces or experimental misalignment. A calibration plate with high contrast equal-spaced dots array, as shown in Figure 13, can provide direct positioning reference in three-dimensional space for the calibration. Firstly, the calibration plate is put into the measuring volume with the dots array physically overlapped with the light sheet. A coordinate transform matrix H can be found according to the dot positions on the image plane by a given spacing of the calibration dots in the physical plane.

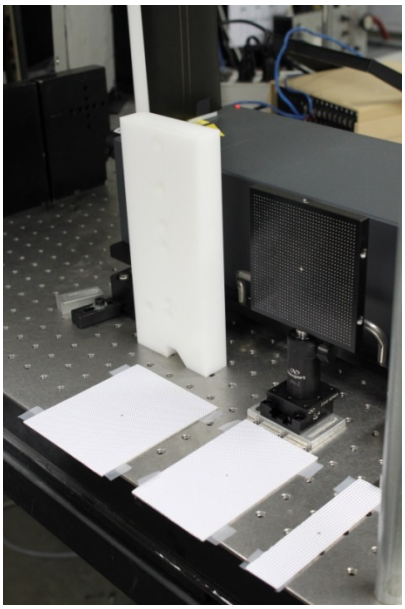

Figure 13 Perspective calibration plates with dot array and alignment block

In order to capture the fluid motions in a cyclone turbulent flow via 2-D PIV measurement, a series of images taken at different distances from the axis of the reactor is required. Due to the refractive index difference across air (n=1.00028) and polycarbonate (n=1.5849) interfaces, a ray-tracing analysis is performed by following Snell's law according to the reactor geometry using MATLAB shown in Figure 14, Figure 15 and Figure 16. The result shows that the light distortion in the conical part is severe beyond the PIV system's capability. Second, the spacing between the light sheet planes is unchanged before and after entering the cylindrical reactor wall. For example, when two light sheets by 0.5 inch spacing go into the reactor, the spacing between the light sheets after going into the reactor is still 0.5 inch. The total reflection occurs when the incident light sheet is deviated beyond 62.1 mm in Z direction. The level of light

distortion becomes significant when the light sheet deviates by more than 25.4 mm. Thus the images are captured at 0, 12.7 and 25.4 mm in Z position under the distortion limit while considering the depth of field of the camera. In PIV measurement, multiple reflections of the light sheet in the reactor generate eight to nine pairs of bright vertical stripes on the image plane where the particle information are lost due to off-scale light intensity covering the area. One way to reduce the drawback is to paint a laser absorbing dye such as the Rhodamine 590 or Rhodamine 6G ($C_{28}H_{31}ClN_2O_3$) on the inner surface. The paint absorbs 532 nm light and re-emit in 650 nm wavelength, which can be filter out by a band pass filter on the camera lens. In this application, a diffusive background paper is placed on the inner wall to reduce the reflecting light intensity. Two beam blocks are used at the two sides of the image plane to prevent the off-scale light intensity entering the camera.

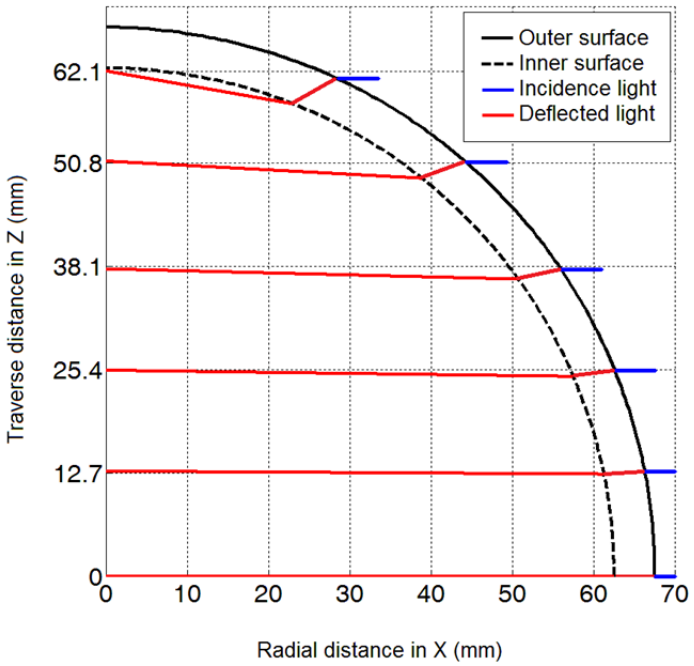

Figure 14 Light distortion across reactor wall

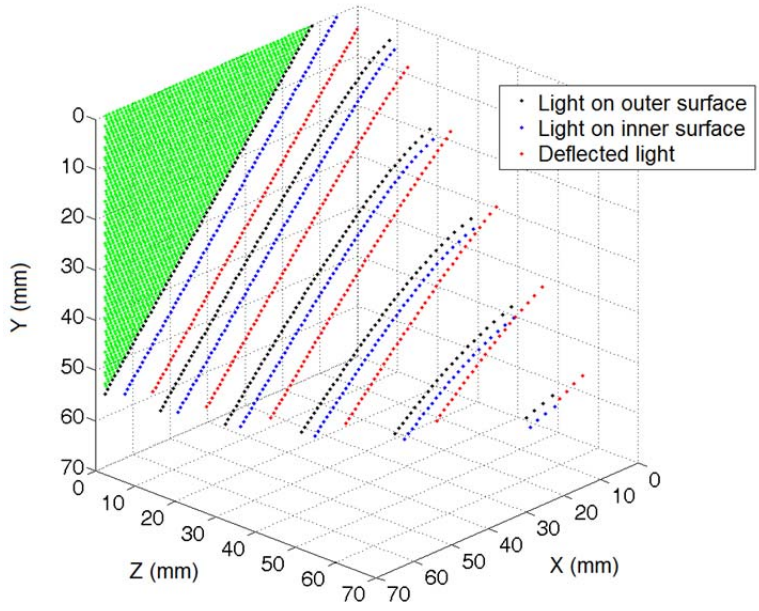

Figure 15 Light distortion across conical part of reactor – 3-D view

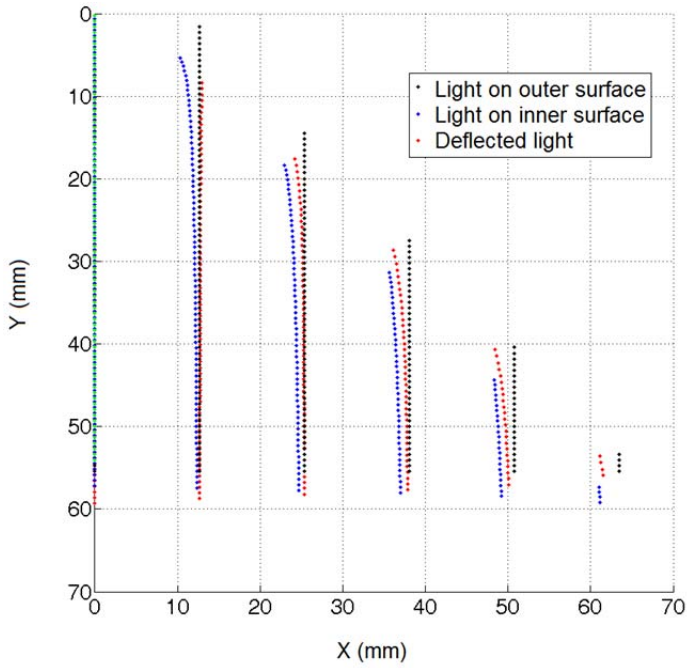

Figure 16 Light distortion across conical part of reactor – 2-D view

Once the extent of light sheet deflection is determined, a calibration plate with a dot array is placed in the reactor while the surface of the dot array is aligned with the deflected light sheet plane for 2-D calibration. The camera is positioned to hold the calibration plate image at the center of the image plane and to keep the viewing direction perpendicular to the calibration plane to minimize the defocusing effect. If the calibration dots are not fully in-focus on the image plane, increasing the F-number helps to increase depth of field with a smaller aperture. After recording the calibration images provided the known spacing between two consecutive calibration planes and order of the transfer function, the software can generate the transfer function between the image planes and the physical planes.

3.6 Reactor model

The main body of the solar reactor model is constructed of a cylindrical part and a conical part as shown in Figure 17, both made of polycarbonate to allow optical access. The cylindrical part is 125 mm in inner diameter, 135 mm in outer diameter and 120 mm in height. The conical part is a 45° angled frustum with 125 mm inner diameter on one side and 10 mm diameter on the other. The reactor wall thickness is 5 mm. The internal channels and spaces are formed with four engraved disks shown in Figure 18 to create a main flow cyclone and auxiliary shield flows in the reactor.

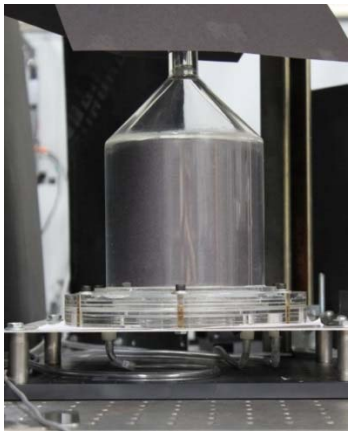

Figure 17 Solar rector model

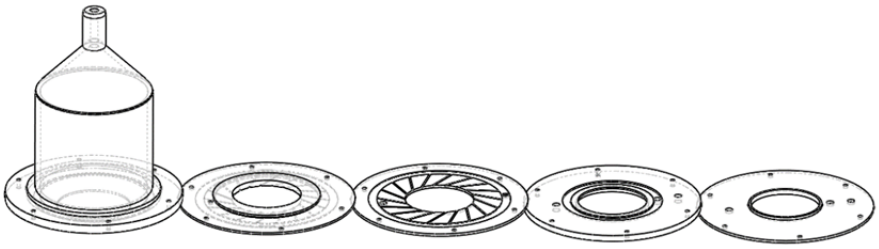

Figure 18 Assembly parts of the reactor model

The seeded fluids are branched and transported into the reactor model at the three flow supply inlets. The main flow entered the reactor via 18 eccentric circular channels by a 45° intercept angle to the inner wall and forms a cyclone flow field around the axis of the reactor, shown in Figure 19. The diameter of the eccentric channels is 2 mm. The window shield flow entered the reactor via an annular-shaped slot of 0.2 mm in height; the wall shield flow entered the reactor via a vertical ring-shaped slot of 0.2 mm in width. The shield flows form gas curtains covering the inner wall to prevent the carbon particle deposition.

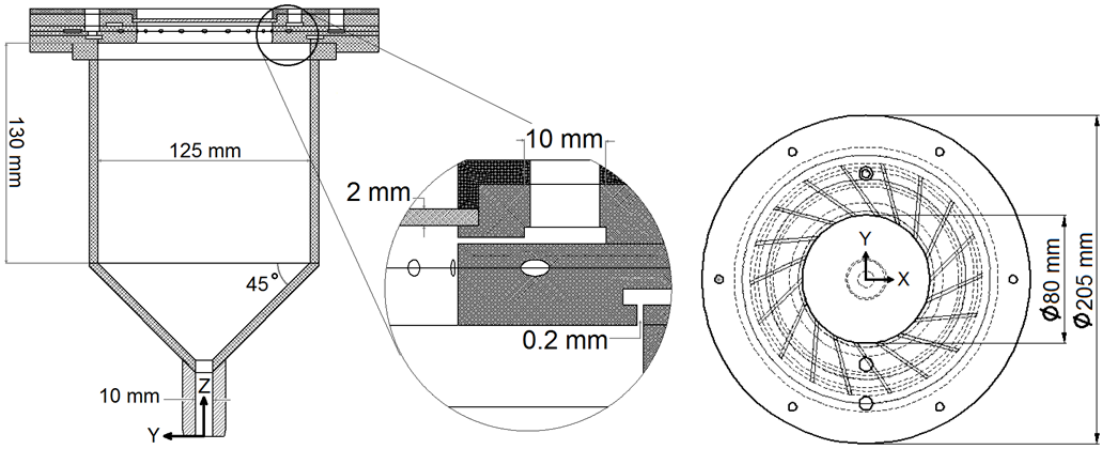

Figure 19 Inner geometry of the reactor model

In order to ensure uniform tracking particle distribution over the entire flow field, three annular buffering spaces are created in the passages of the inlet gases in the reactor model. These three cavities act as buffering spaces between the single flow supply inlet and the axial-symmetric flow entrances to allow the particle-fluid mixture to redistribute

to reach uniform inlet condition. Each of the buffering spaces is 10 mm in width and 2 mm in height subject to limited volume in the top part of the reactor. The hole size of the three flow supply inlets is 1/8 NPT. In order to prevent the material fracture during operation, the hose fittings are made of nylon to provide protection to the reactor material if stress accumulates during assembly and air-tight test. According to the reference CFD setting, the volumetric flow rate of the main flow and wall shield flow are both 10 LPM; the flow rate of the wall shield flow is 1 LPM, therefore the mean flow velocities at the flow entrances are 2.95 m/s for the main flow jets, 2.13 m/s for wall shield flow and 0.33 m/s for window shield flow.

3.7 Atmospheric case experiment

The experiments are performed using air in ambient pressure first to exam the PIV image quality and system accuracy. The system layouts are demonstrated in the following Figure 20 and Figure 21. After the light sheet been generated by a the lens set mounted on the laser head, the light sheet expands vertically and goes through the transparent reactor model at zero degree with respect to viewing plane of the camera. Three alignment blocks are placed on the path of the reflecting light to prevent the reflecting light from entering the laser and to provide additional indication of light sheet alignment. The alignment between the reactor model and the light sheet is controlled by adjusting the four screw legs of the base plate under the reactor. The capture position is

controlled by the traverse plate. The seeding system is connected upstream of the flow control system, shown in Figure 22.

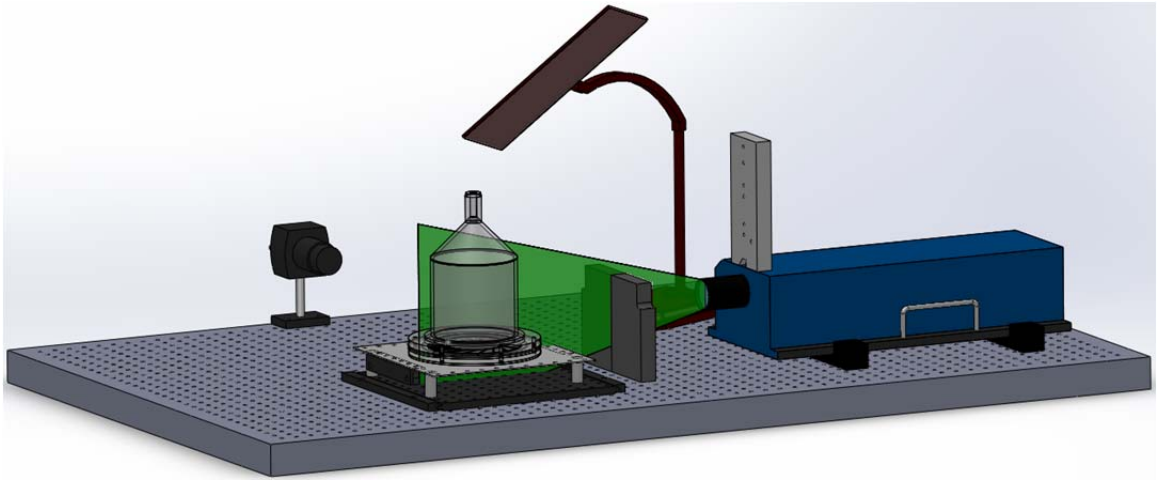

Figure 20 Side view setup of PIV experiment

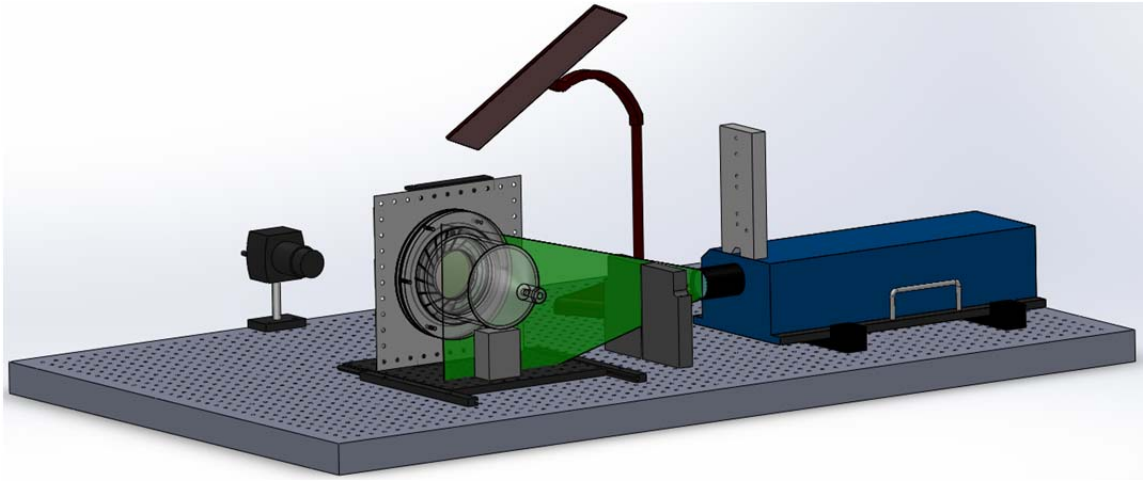

Figure 21 Top view setup of PIV experiment

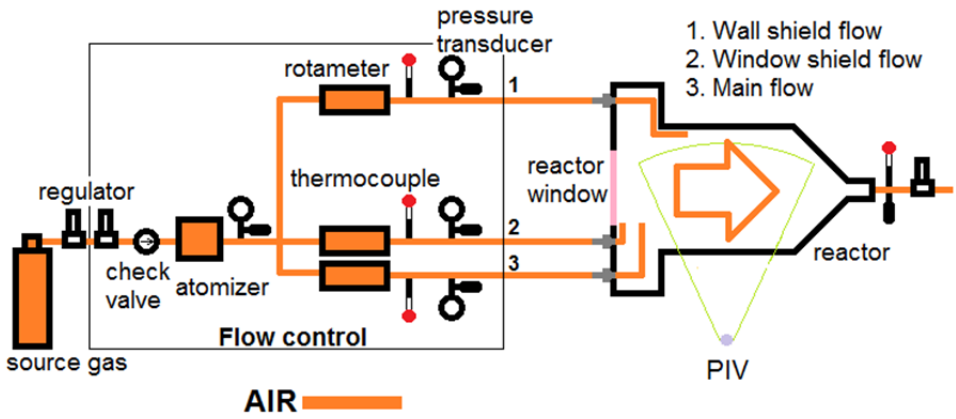

Figure 22 Schematic of flow control of atmospheric air case

The time interval between two captured frames is one of the most critical PIV parameters. According to the reference CFD setting, the maximum inlet mean flow speed is 2.95 m/s. The one-quarter rule is applied to reduce in-plane and out-of-plane particle image pairing loss. When the thickness of light sheet is 1 mm, then the estimated upper limit of the time interval is 194 μs; the lower limit is 85 μs. Thus the time interval in the experiment is tested from 30 μs to 400 μs. The experimental results show that when time interval is larger than 200 μs, the central region of the vortex starts to lose particle image pairs due to out-of-plane limitation. This also implies the flow speed is at maximum at the central region across the inner diameter of reactor. On the other hand, in the optical analysis when time interval is lower than 100 μs, the dynamic range decreases to 22 and the measurement uncertainty starts to increase drastically. Therefore the time interval is set to 150 μs with a dynamic range equal to 34 compared to an optimal value of 36 under same experiment setup for all experiment cases.

3.8 Vacuum case experiment

In order to obtain the flow dynamics of momentum levels the same as the real solar reactor flow, the pressure is decreased to around 1/3 atmospheric absolute pressure. The experimental layouts of the vacuum case, shown in Figure 23, are the same as those of the atmospheric case except for a downstream vacuum control. The operating pressure of the reactor is maintained by the vacuum pump located downstream and is adjusted by a high accuracy vacuum regulator. The tracking particles are collected by the particle filter to prevent contact damage to the vacuum pump. The Reynolds number was maintained while the density is decreased due to pressure change. The kinetic viscosity is estimated to about 2.5 times smaller than the real reactor fluid. Therefore the average flow velocity is expected to be 2.5 times smaller than the real reactor in order to hold the Reynolds numbers the same.

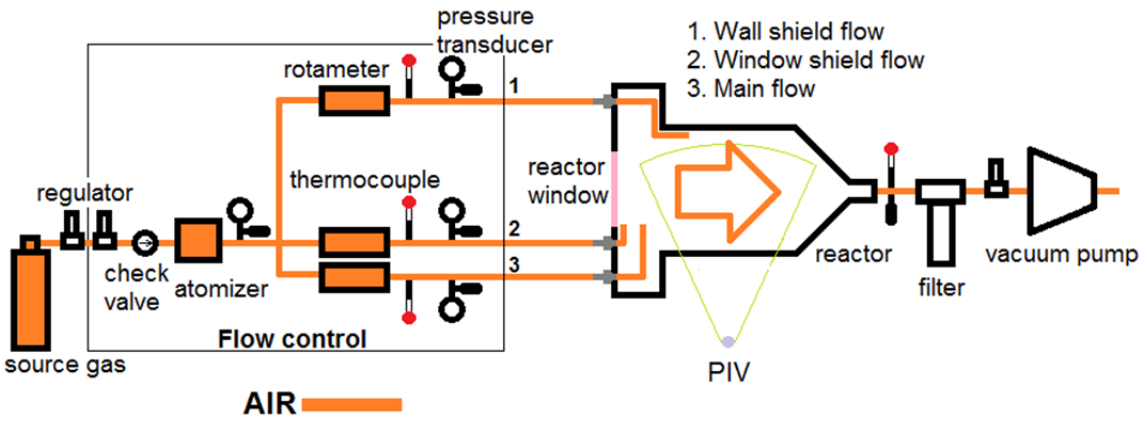

Figure 23 Schematic of flow control of vacuum air case

3.9 Pressure sensitive paint (PSP)

Although the PIV can help to reconstruct the 3-D structure of the cyclone flow field, it fails when reaching the near-wall region due to the multiple reflections of the light sheet in the cylindrical space. Therefore an alternative is required in order to obtain flow information at the near-wall region. The effectiveness of the wall shield flow can be related to the fluid mixing between the main flow and the wall shield flow on the wall via the Pressure Sensitive Paint (PSP) technique as shown in Figure 24.

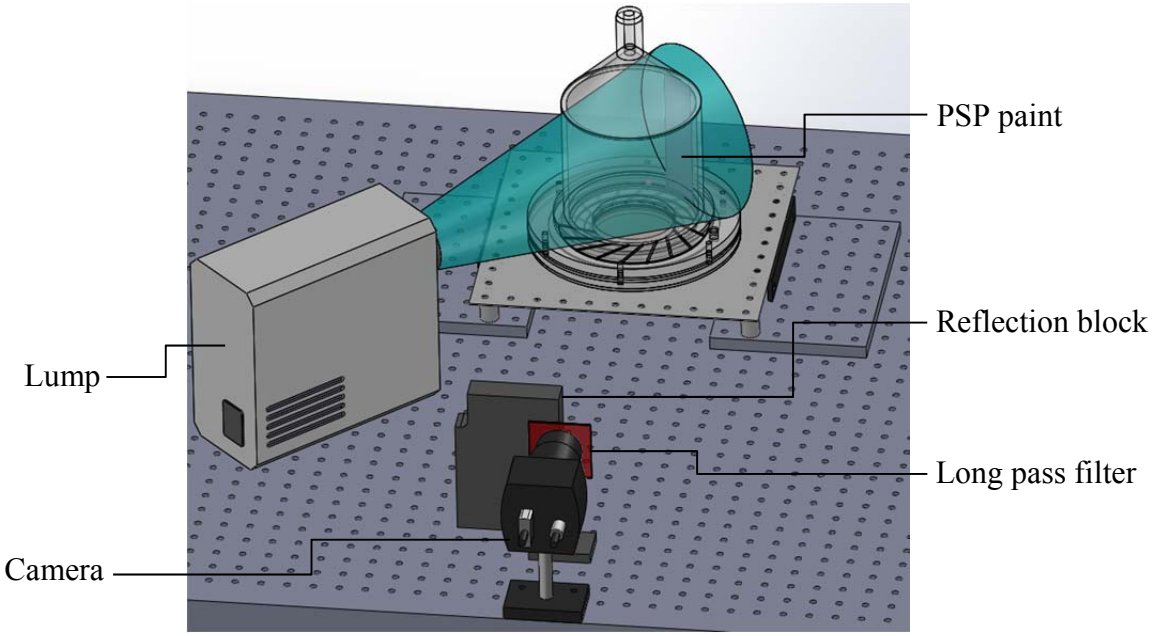

Figure 24 PSP experiment configuration

In addition to the PIV method, the PSP method is also a non-intrusive and whole-field flow visualization technique. The principle of the PSP relies on the sensitivity to the existence of oxygen for a specific luminescent chemical for example the Platinum tetra (pentafluorophenyl) porphine (PtTFPP), which absorbs 380 nm – 520 nm wavelengths light as the excitation and emits > 600 nm fluorescent radiation as the electrons at excited state jump back to ground state. When oxygen is in contact with the chemical, the fluorescent emission is suppressed and converted to molecular vibration in a form of heat called oxygen quenching. Therefore, the more oxygen molecules in contact with the paint, the darker the paint appears to be. On the image receiver side, the receiving intensity field I is a function of position, pressure, temperature, paint thickness, illumination, chemical degradation and time. The maximum spatial resolution depends on the optical performance of the image receiver. Disregarding the parameter variations beyond the scope, a simple relation between the partial pressure of oxygen P to the emission intensity field of the paint I at a certain temperature T is given by the Stern-Volmer equation.

$$\frac{I_{ref}}{I} = A(T) + B(T)\frac{P}{P_{ref}}$$

where I_{ref} is the reference intensity field. P_{ref} is the reference pressure field. In this application, the reference pressure is 101.325 kPa; the temperature during measurement

is controlled at 70 °F; the light intensity field in the ambient air is taken as the reference intensity field.

In order to perform the PSP measurement on the curved surface in the reactor, a polymer thin film is used as the substrate for the paint to allow bending tolerance. A black insulation layer is painted on the substrate to provide stable optical and attaching background surface for the PSP paint. Nine layers of the PSP chemical compound are painted on the film following a standard PSP painting procedure by Innovative Scientific Solutions (ISSI) Inc. The overall thickness of a painted film is 0.17 mm. In order to measure the 1-D propagation of wall shield flow concentration, the paint is attached to the inner wall covering area of 130 mm in axial length of the cylindrical part and 13 mm in width as shown in Figure 25. The periphery of the paint is further smoothed. The excitation source is a 150W/3200 K color temperature halogen lamp with SM1 lens mount. A 500 nm SM1 short-pass filter lens is mounted on the lamp head to filter the longer wavelength light. A 52 mm 600 nm long-pass filter is mounted on the camera lens to allow the longer wavelength emission from the measuring volume to pass. The environmental light sources are reduced by preforming measurements in a dark test chamber.

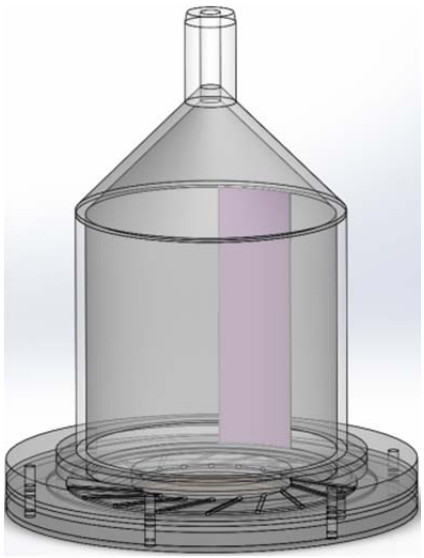

Figure 25 PSP position in the reactor

3.10 Computational Fluid Dynamics (CFD) method

3.10.1 Overview

Once the CFD code is verified using the experimental data, a parametric study on the reactor geometry can be performed using the computational fluid dynamics (CFD) method. The geometry of the CFD model is constructed using the SOLIDWORK drawing of the reactor model for the experiment. The geometry is then meshed by the software GAMBIT. The entire model is constructed of hexahedral cells. Over 99 % of the cell volumes are structural mesh. The meshed model is shown in Figure 26. The total cell number is 2.72 million. It mainly contains three sections: the internal channels and

slots for the three flows, the entrance region for the three flows interaction, and the cylindrical region constructed of radial hexahedral mesh.

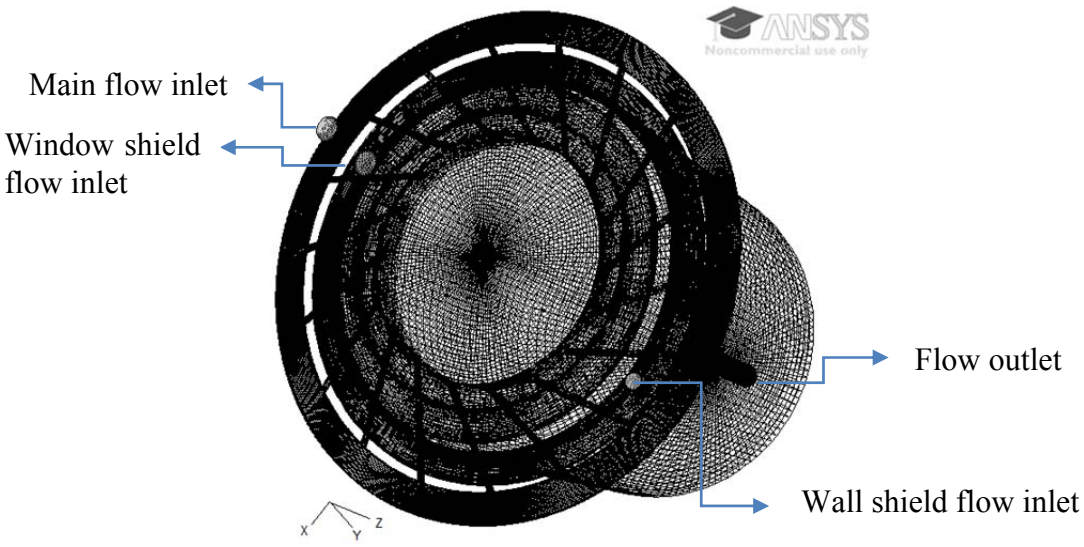

Figure 26 Computational geometry of the reactor model

3.10.2 Control equation

The governing equation is derived from the momentum conservation assuming a Newtonian fluid. The equation is valid for both laminar and turbulent flows.

$$\frac{\partial(\rho\phi)}{\partial t} + div\left(\rho \boldsymbol{u}\phi\right) = div\left(\Gamma \cdot grad\,\phi\right) + S$$

The equation shows in order of the transient term, the convective term, the diffusive term and the source term. ϕ is a generalized variable that represents physical quantities such as velocity components, temperature or species mass-concentration, etc. Γ is a generalized diffusive coefficient, S is a generalized source term.

3.10.3 Finite Volume Method (FVM)

The Finite Volume Method (FVM) is adopted by most of the commercial CFD software including the ANSYS FLENT used in this research. FVM is known for its high computational efficiency in solving complex fluid interactions by discretizing the fluid volume geometry into non-overlapped sub-volumes called cells. All quantities for calculation are located at the geometric center of the cell. The collective of these cells form the computation domain. The transports of the physical quantities between every two adjacent cells are linked mathematically by the discretized control equation. The coefficients in the control equation are changed according to the physical quantities of interest to describe the transport behavior between adjacent cells. Based on the conservation characteristic above, FVM ensures the conservation of integrated quantities.

3.10.4 Discretization scheme

The discretized control equation of CFD expresses a node value in the form of a summation of neighboring node values with weighting coefficients on each of them.

$$a_p \phi_P = \sum a_{nb} \phi_{nb} + b$$

ϕ is the transporting quantity; subscript P represents the node to be solved; a are the weighting coefficients obtained by discretization; subscript nb represents the neighboring node in space and time frames; b represents the sum of the source term and other terms not included in the previous terms.

The option of the discretization schemes to the governing equations mainly discretizes the transient and convective terms while the diffusion term is discretized by the central difference scheme by default. The central difference scheme provides second order precision but might also cause oscillating or unphysical solutions when the Peclet number P_e, defined as the ratio of convection to diffusion, is large causing negative weighting coefficients in the discretized control equations. In order to solve the oscillating issue, the first-order upwind scheme referring to the flow direction in the first-order discretized convection term ensures all the coefficients in the discretized control equation are positive. Although the first-order upwind scheme is unconditionally

stable, its truncation error tends to overestimate the diffusion effect, especially when the Peclet number is large. The hybrid scheme which shifts between the previous two schemes according to the Peclet number. Therefore the overall precision of the hybrid scheme is first-order. The power-law scheme considers the interaction between the convection and diffusion simultaneously by discretizing the exact solution of a one-dimensional convection-diffusion control equation, but this scheme loses accuracy in multi-dimension or source existing problems due to the simplified nature of the equation formulation. The second-order upwind scheme introduces a more physical mechanism of the flow by introducing more upstream information and thus reduces the false diffusion compared to that in the first-order upwind scheme. The QUICK (Quadratic Upwind Interpolation of Convective Kinematics) scheme extends the second-order up-wind scheme by adding curved interpolation instead of linear interpolation and thus has better second-order precision. The QUICK scheme is especially suitable for handling structured grids with faces normal to the flow direction than second-order upwind scheme. Therefore the QUICK scheme is usually adopted for a hexahedral grid. As for other grid types, second-order upwind scheme remains the first choice.

The transient schemes can be divided into explicit, implicit and hybrid schemes. The explicit scheme can run under limited computation memory because of its simplicity. However, in order to stabilize the convergence quality, the time step should be decreased when a finer grid size is required. The implicit scheme, although being computation memory intensive, is unconditionally stable and free of time step limitation. The hybrid

transient scheme, also called Crank-Nicolson scheme, essentially applies a central difference scheme to the transient term and thus could have second-order precision. Since an implicit scheme is involved, it's also computation memory intensive.

3.10.5 Solver

Before solving the discretized control equations, two major problems are required to be overcome. First, the control equations contain non-linear terms. Second, the interaction between pressure and velocity makes them coupled with each other in the equations. The former can be addressed by iteration starting with an initial guess. As for the latter, the equations can be solved all at once by a coupled solver or, one by one orderly by a segregated solver. Despite the fact that segregated solvers are inherently less complete and less stable than coupled solvers, from a cost-to-performance point of view, segregated solvers are still prevalent in the field. The most popular segregated solver was proposed by Patankar and Spalding (1972) by guessing an initial pressure field to solve every control equation sequentially called Semi-Implicit Method for Pressure-Linked Equations (SIMPLE), which is the default solver in FLUENT.

SIMPLE proposed by Spalding and Patankar (1972) was first based on utilizing staggered grids, which stored each velocity component on a grid network shifted about half a grid while the scalar quantities are stored on the original grid network to faithfully reflect the input pressure field. Based on this concept, current commercial programs

developed collocated grids by interpolating velocity quantities called momentum interpolation to unify the grid systems, which gives higher computation efficiency since there's only one grid network.

When the SIMPLE iteration starts, first, the coefficients of the discretized control equations are solved by an initial guessed pressure filed and a guessed velocity field. Second, a new pressure field is calculated by adding the previous pressure field to a pressure correction quantity obtained via a pressure correction equation derived from the continuity equation. Third, a new velocity field is also calculated by adding the previous velocity field to a velocity correction quantity derived from the pressure correction quantity difference. This step is the most important assumption in the SIMPLE scheme because it successfully decouples the velocity and pressure. Fourth, the additional scalar quantities, such as temperature, enthalpy etc. are calculated in their discretized control equation with the new pressure and velocity. Finally the convergences of the physical quantities are checked and repeated iterations are used until the solution remains unchanged. When the decoupling assumption is made, the scheme becomes inconsistent because the velocity correction relies on only the pressure difference. Therefore the SIMPLE scheme needs more iteration. SIMPLEC (SIMMPLE-Consistent) scheme proposed by Doormal and Raithby (1984) extends the SIMPLE scheme by recovering the consistency when deriving the velocity correction quantity in the third step above and thus tends to increase the correcting efficiency and converging rate. PISO scheme proposed by Issa (1986) uses a pressure correction equation twice for velocity

correction, which requires higher memory usage to enhance the correction efficiency. PISO scheme is especially suitable for transient problems and cases where the velocity and scalar quantities tend to be decoupled. For the highly coupled problems, for example velocity and pressure, SIMPLE/SIMPLEC is the better choice.

In most engineering applications, the mean flow field is more important than the whole resolved flow field. However, in most of the turbulent flows the mean flow is deeply affected by the turbulence. Therefore it's reasonable to include the turbulence effects in the model by introducing turbulence related parameters such as turbulent kinetic energy, k, and turbulent dissipation rate, ε, proposed by Launder and Spalding (1972).

3.10.6 Reynolds-averaged Navier-Stokes (RANS) equation

By time-averaging the control equation of momentum yields:

$$\frac{\partial}{\partial t}\left(\overline{\rho u_i}\right)+\frac{\partial}{\partial x_j}\left(\overline{\rho u_i u_j}\right)=\frac{\partial}{\partial x_j}\left[-\overline{P}\delta_{ij}+2\mu\overline{S_{ij}}-\rho\overline{u_i' u_j'}\right]$$

$\overline{S_{ij}}$ is the mean rate of shear strain; $\overline{u_i'}$ is the time-averaged fluctuating velocity components. $\overline{P}$ is the mean pressure field. The equations set under Cartesian coordinate system include a time-averaged continuity equation, 3 time-averaged momentum

equations, and usually an additional time-averaged transport equation for a scalar quantity Φ.

However the system unknowns include 5 time-averaged quantities ($\bar{u}$, $\bar{v}$, $\bar{w}$, $\bar{P}$, Φ) and 6 Reynolds stresses $-\rho\overline{u_i'u_j'}$. The 6 Reynolds stresses can either be solved individually or, by introducing a flow dependent quantity called turbulent viscosity, μ_t, which represents the scale of turbulence effect to the mean flow.

3.10.7 Linear turbulent viscosity models

The Reynolds stresses obtained from RANS can be modeled by a linear constitutive relationship with the mean rate of flow strain. According to the turbulent viscosity hypothesis by Boussinesq (1877), the deviatoric Reynolds stress is proportional to the mean rate of shear strain $\overline{S}_{ij}$:

$$-\rho\overline{u_i u_j} + \frac{2}{3}\rho k\delta_{ij} = 2\mu_t \overline{S_{ij}}$$

$$k \equiv \frac{\overline{u_i'u_i'}}{2}$$

k is the mean turbulent kinetic energy. $\overline{S}_{ij}$ is the mean strain rate. This assumption allows one to make an analogy of turbulence viscous effects on the mean flow strain to the molecular viscous effects on a laminar flow gradient. Because of this assumption, the turbulent viscosity is isotropic.

3.10.8 Two-equation models

The two-equation models solve two turbulent transport related variables in order to estimate the turbulent viscosity. In general one of the variables describes the energy of the turbulence, such as the turbulent kinetic energy k ; the other determines the scale of turbulence (length-scale or time-scale), such as the turbulent dissipation rate ε , or the specific dissipation ω depending on what type of two-equation model it is.

The weakness of the Boussinesq's approximation is that it is not valid in complex flows. The Reynolds stress tensor is not necessarily proportional to the strain rate tensor. Because of its isotropy assumption, it is valid in simple flows like 2D axisymmetric jet, maxing layers and wakes, but in complex flows, like flows with strong curvature, or strongly accelerated or decelerated flows the Boussinesq's approximation is not valid. This gives two equation models intrinsic problems to predict strongly rotating flows and other flows where anisotropy effects are significant. Two equation models also often have problems to predict strongly decelerated flows like stagnation flows.

3.10.8.1 $k-\varepsilon$ Model

By definition, two equation models include two extra transport equations to represent the turbulent properties of the flow. This allows a two equation model to account for history effects like convection and diffusion of turbulent energy. By deriving two transport equations solving for turbulent kinetic energy k and turbulent viscosity dissipation rate ε, the isotropic turbulent viscosity is determined. The isotropic Reynolds stresses are expressed as function of mean rate of strain and turbulent viscosity. The two additional equations, derived from RANS, simplified by turbulent viscosity hypothesis are:

$$\frac{\partial(\rho k)}{\partial t} + div\left(\rho k \mathbf{U}\right) = div\left[\left(\mu + \frac{\mu_t}{\sigma_k}\right) grad\, k\right] + G_k + G_b - \rho\varepsilon - Y_M + S_k$$

σ_k is the Prandtl number for turbulent kinetic energy k; G_k and G_b are the productions of k induced by the mean flow strain and buoyancy effect, which are formulated by known flow parameters; Y_M is the dissipation of k due to the local turbulence dilatation; S_k is the source term. The ε equation can be obtained by multiplying k equation by (ε/k):

$$\frac{\partial(\rho\varepsilon)}{\partial t} + div\left(\rho\varepsilon \mathbf{U}\right) = div\left[\left(\mu + \frac{\mu_t}{\sigma_\varepsilon}\right) grad\, \varepsilon\right] + C_{1\varepsilon}\frac{\varepsilon}{k}(G_k + C_{3\varepsilon}G_b) - C_{2\varepsilon}\rho\frac{\varepsilon^2}{k} + S_\varepsilon$$

σ_ε is the Prandtl number for turbulent dissipation ε ; C_ε are constants based on homogenous isotropy assumption in dissipation scales. S_k is the source term of ε. The turbulent viscosity in high Reynolds number is then expressed as:

$$\mu_t = C_\mu \frac{k^2}{\varepsilon}$$

$$\sigma_k = 1.0 \quad \sigma_\varepsilon = 1.3 \quad C_{1\varepsilon} = 1.44 \quad C_{2\varepsilon} = 1.92 \quad C_\mu = 0.09$$

3.10.8.2 RNG Model

Yakhot and Orzag (1986) developed a k-ε model based on the renormalization group (RNG) method. When the turbulence is in a rotating or swirling mean flow, the final turbulent viscosity is modified as a function of swirl flow parameters and the original turbulent viscosity in the k-ε model to represent the mean flow result influenced by the small scale turbulence. Besides enhancing the diffusion term in the k equation, the RNG model considers the swirling effect by adding an additional term in the ε equation, which makes the largest difference between the RNG model and the standard model.

$$\frac{\partial(\rho k)}{\partial t} + div\left(\rho k \mathbf{U}\right) = div\left[\alpha_k \mu_{eff}\, grad\, k\right] + G_k + G_b - \rho\varepsilon - Y_M + S_k$$

$$\frac{\partial(\rho\varepsilon)}{\partial t} + div\left(\rho\varepsilon \boldsymbol{U}\right) = div\left[\alpha_\varepsilon \mu_{eff}\, grad\, \varepsilon\right] + C_{1\varepsilon}\frac{\varepsilon}{k}(G_k + C_{3\varepsilon}G_b) - C_{2\varepsilon}^{*}\rho\frac{\varepsilon^2}{k} + S_\varepsilon$$

$$C_{2\varepsilon}^{*} = C_{2\varepsilon} + \frac{C_\mu \eta^3 (1-\eta/\eta_0)}{1+\beta\eta^3}$$

The parameter $\eta \equiv (2S_{ij}\cdot S_{ij})^{1/2} k/\varepsilon$ indicates the extent of mean rate of strain. The turbulent viscosity in high Reynolds number is then expressed as:

$$\mu_t = C_\mu \frac{k^2}{\varepsilon}$$

$$\alpha_k = \alpha_\varepsilon = 1.39 \;\; C_{1\varepsilon} = 1.42 \;\; C_{2\varepsilon} = 1.68 \;\; \eta_0 = 4.38 \;\; \beta = 0.012 \;\; C_\mu = 0.0845$$

For the flow with strong swirl, the strain is high, the coefficient $C_{2\varepsilon}^{*}$ is decreased, the dissipation increases, the kinetic energy decreases, therefore the turbulent viscosity decreases. With the modified term the RNG model is more suitable for rotating or swirling flows.

3.10.9 Wall treatment

Either k - ε or RNG models are for high Reynolds number turbulence models. An additional fluid treatment is required to solve the fluid flow in the near wall region where the flow is dominated by molecular viscosity.

High Reynolds number treatment also known as wall functions approach relies on log-law velocity profile and therefore the first computational cell must have its centroid in the log-layer. Use of high Reynolds number treatment enhances convergence rate and often numerical stability. None of the current approaches can deal with the buffer layer. Therefore the first computational cell should be either in the viscous sub-layer or in the log-layer.

Low Reynolds number treatment integrates every equation up to the viscous sub-layer via modified k - ε model for high Reynolds number. Therefore the first computational cell must have its centroid in $y^+ \sim 1$. This results in very fine meshes close to the wall. Other wall treatments are the blending techniques switching between high and low Reynolds number treatments. They cannot be regarded as the correct representation of the buffer layer.

3.10.10 Reynolds Stress Transport Model (RSTM)

The Reynolds stress transport model (RSTM) provides closure for the Reynolds-Averaged Navier Stokes equation by solving additional transport equations for the six independent Reynolds stresses. The formulations are as followed.

$$\frac{\partial}{\partial t}\left(\rho\overline{u_i'u_j'}\right)+\underbrace{\frac{\partial}{\partial x_k}\left(\rho\overline{u_k}\,\overline{u_i'u_j'}\right)}_{C_{ij}}=-\underbrace{\frac{\partial}{\partial x_k}\left[\rho\overline{u_i'u_j'u_k'}+\overline{p'u_i'}\delta_{kj}+\overline{p'u_j'}\delta_{ki}\right]}_{D_{T,ij}}$$

$$+\underbrace{\frac{\partial}{\partial x_k}\left[\mu\frac{\partial}{\partial x_k}\left(\overline{u_i'u_j'}\right)\right]}_{D_{L,ij}}-\underbrace{\rho\left(\overline{u_i'u_k'}\frac{\partial\overline{u_j}}{\partial x_k}+\overline{u_j'u_k'}\frac{\partial\overline{u_i}}{\partial x_k}\right)}_{P_{ij}}-\underbrace{\rho\beta\left(g_i\overline{u_j'\theta}+g_j\overline{u_i'\theta}\right)}_{G_{ij}}$$

$$+\underbrace{\overline{p'\left(\frac{\partial u_i'}{\partial x_j}+\frac{\partial u_j'}{\partial x_i}\right)}}_{\phi_{ij}}-\underbrace{2\mu\overline{\frac{\partial u_i'}{\partial x_k}\frac{\partial u_j'}{\partial x_k}}}_{\varepsilon_{ij}}$$

where the equation can be rewritten in the form of

$$\frac{\partial}{\partial t}\left(\rho\overline{u_i'u_j'}\right)+C_{ij}=D_{T,ij}+D_{L,ij}-P_{ij}-G_{ij}+\phi_{ij}-\varepsilon_{ij}$$

$D_{T,ij}$, G_{ij}, ϕ_{ij}, ε_{ij} which contain non-closed terms were further modeled to reduce the number of unknowns to close the equation set. By deriving 6 Reynolds stress transport equations, providing two additional transport equations, solving for k and ε, the isotropic turbulence assumption in the turbulent viscosity hypothesis is removed from the RANS equations. The six Reynolds stresses in the RANS equations are individually resolved. The RSTM model is good for predicting complex flow such as highly strained flow, secondary flow, separation, rotating and swirling flow. However, the fidelity is questioned because of the closure assumptions, especially the pressure strain, ϕ_{ij}.

In this research, the RNG, $k-\omega$, RSTM, and LRR models are used to simulate flows along curved boundaries under strong swirling flow effect. The swirl flow dominated option is activated in the RNG model since the swirl number is larger than 0.5.

4 RESULTS

4.1 PIV measurements

The PIV images are captured from two orientations: side view through the transverse reactor wall and top view through the reactor window as shown in Figure 27.

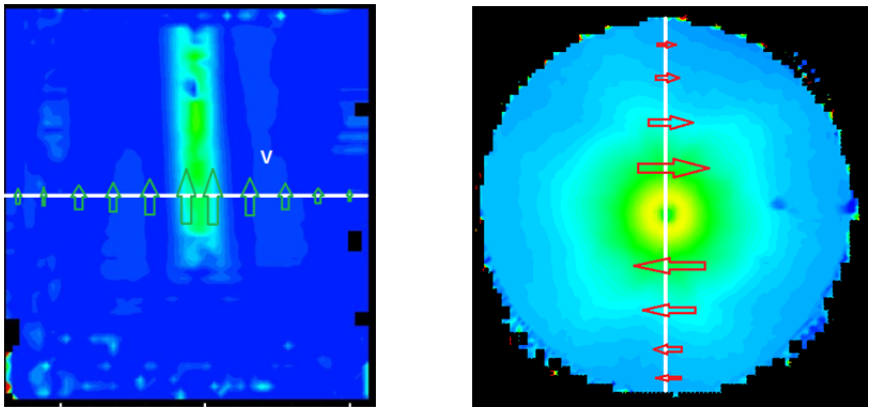

(a) (b)

Figure 27 Illustration of the two orientations in PIV measurement (a) side view (b) top view

4.1.1 Optical noise identification

The velocity gradients can be identified by the existence of vortices. As is mentioned, the existence of the velocity gradient will decrease the SNR value of the image correlation. On the other hand, when velocity gradients exist, the vorticity field tends to show additional none-zero contours, especially around the edge of the captured flow

field and in the central region of the vortex. In order to verify the existence of the vortices, additional side view contours across those vortices patterns are captured as shown in Figure 28, however, no special flow pattern around the area is detected. The vortices around the edge of the flow field are caused by cut-off of particle image. For example, the top view PIV vorticity fields show a common positive vortices ring in red around the edge of the flow field while the flow rotating direction is clockwise. Since the region out of the rotating flow field on the image plane contains no particle image, this blank region is considered as zero-velocity during correlation and thus leads to an artificial velocity gradient between the boundary of the particle-active region and the particle-free region. In the PIV measurement, when the image is captured through the reactor window, the inner geometry behind the window within the range of field of view will also cause zero-velocity region and thus creates artificial velocity gradient. As for the vortices in the central region of the side view PIV, e.g. Figure 29, the vorticity contour shows the vertical vortices patterns in pairs containing positive and negative counterparts on the two sides of the vortex line due to the transition of fluid motion. Another kind of artificial velocity gradient is the irregular local vortices in the middle of the flow field. For example, these vorticity patterns can be found in shape of circular spots in the top view contours as shown in Figure 28, and in shape of stripes in the side view contours. It's usually caused by the blockage of particle information due to reflecting light speckle of the light sheet, lower transparency of the reactor wall or lack of tracking particles in that region. These local vortices patterns tend to appear in pairs because of the opposite directions of velocity gradients on the two sides of the region.

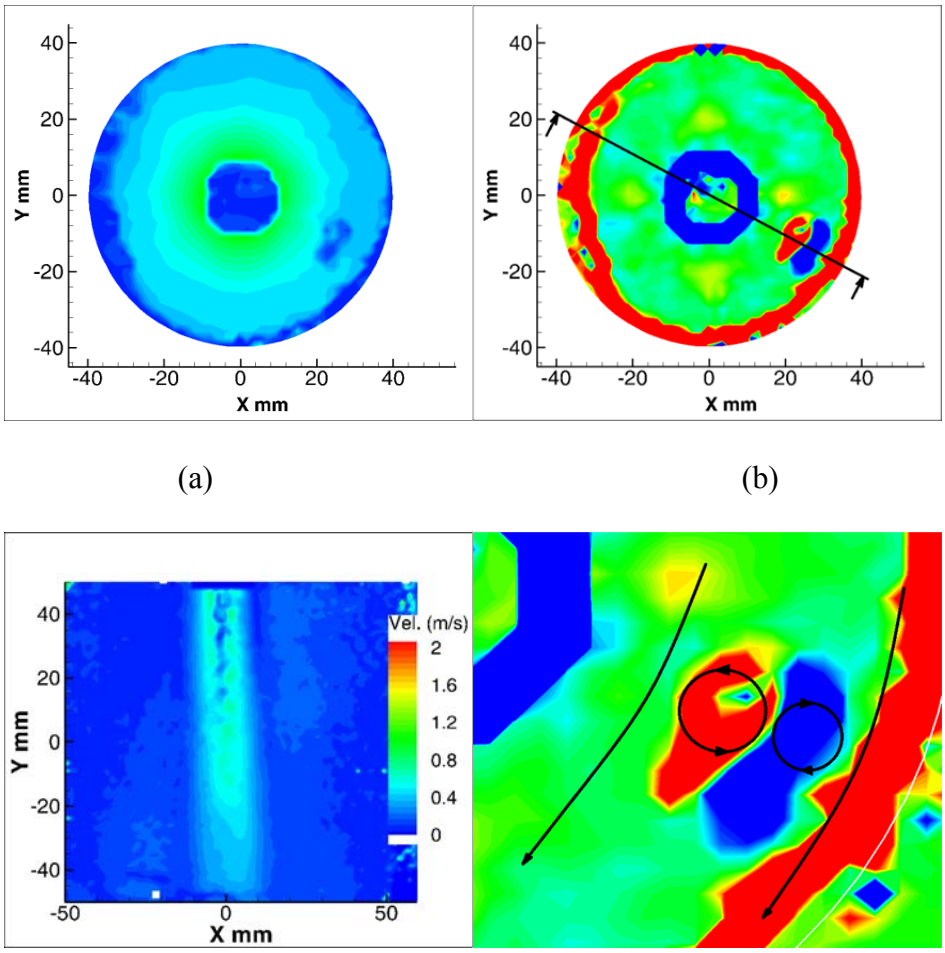

Figure 28 Local noises in PIV measurement (a) velocity contour (b) vorticity contour with indication of additional capturing plane (c) contour on the additional capturing plane across the noises (d) noise spot with indication of local flow motion

4.1.2 Off-axis measurement

Figure 29, Figure 30 and Figure 31 show the velocity magnitude and vorticity contours at three Z traverse positions at 0 mm, 12.7 mm and 25.4 mm using the reference CFD setting as the base case. The arrow lines in the velocity contour indicate the direction of the particles. A vortex line is clearly observed along the boundary of the opposite vortices in the 0 mm deviation vorticity contour.

When the axis of the reactor deviated from the light sheet plane, the tangential components of velocity become dominant. Those tangential components form irregular vorticity patterns as shown in the contours. The appearance of the vorticity patterns is an indication of misalignment between the light sheet and the vortex line. During the capture, the vortex line precesses around the geometric axis of the reactor. Thus the vector fields are obtained from ensemble averages. When the light sheet is aligned with the vortex line statistically, the result shows the irregular vortices stripes vanished. The averaged field shows an axis-symmetric upward-moving jet along the vortex line, surrounded by a downward-moving flow between the edge of the vortex funnel and inner wall while the vectors everywhere else are negligible in magnitude.

The contours show locally blank area near the wall due to the velocity averaging and lack of tangential components. The velocity vectors at the bottom of the reactor are difficult to obtain since the region is dominated by strong fluid motion perpendicular to

the light sheet plane. It's noticed that in the deviated contours, the irregular vortices patterns expand radially outward as the cyclone fluid approaches the entrance and exit of the reactor. It's also noticed that the velocity contours on the left side of the deviated images are more chaotic than those on the right side because of the perspective and focal length between the camera and the light sheet plane.

During the capture, a drifting vortex line is observed. Along the vortex line the distribution of vortices indicates an upward-moving flow with the highest axial velocity in the vortex funnel decaying toward the reactor wall. It is also observed that the flow at the bottom of the reactor is dominated by the main flow which doesn't allow the particle displacement to be captured. There is no significant global mean flow direction between the edge of the vortex funnel and the near wall region in the side view orientation. Also, within this region the fluid motions are identified by only local small displacements of tracking particles implying a primary out-of-plane motion.

The vortices contour along two sides of the axis of the reactor shows that the fluid is accelerating upward while approaching the vortex line. It also shows that the in-plane motion of the fluid in the region between the vortex funnel and the wall are moving relatively slow. The vortices near the wall region remained after the ensemble averaging are the artificial vortices as a result of particle image boundary.

In the 0.5 inch deviated contour, the averaged tangential velocity is 0.993 m/s with 0.992 m/s horizontal component and 0.022 m/s vertical upward component. In the 1.0 inch deviated contour, the averaged tangential velocity magnitude is 0.511 m/s with 0.509 m/s horizontal component and -0.044 m/s vertical downward component.

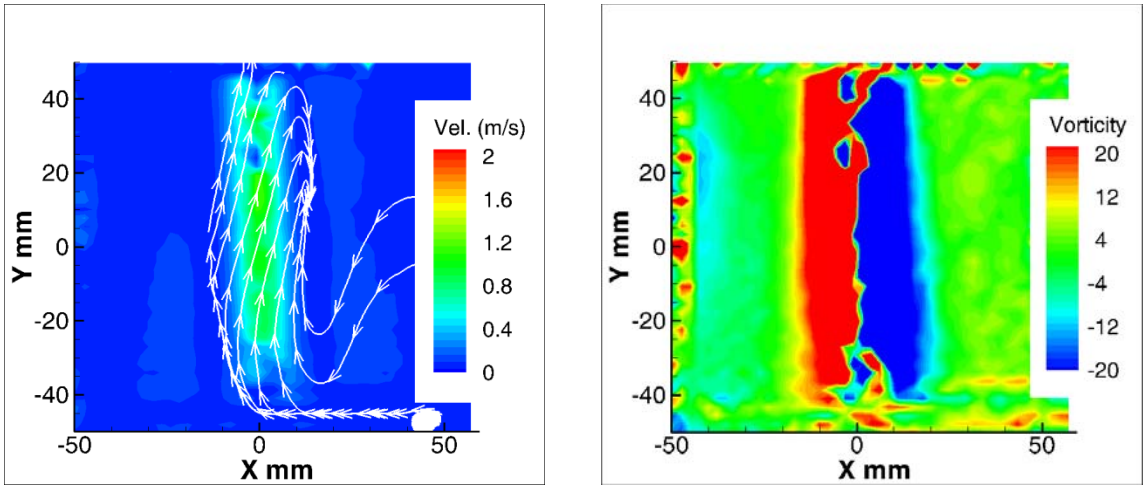

Figure 29 Velocity and vorticity contours of atmospheric air case – 0 mm deviation

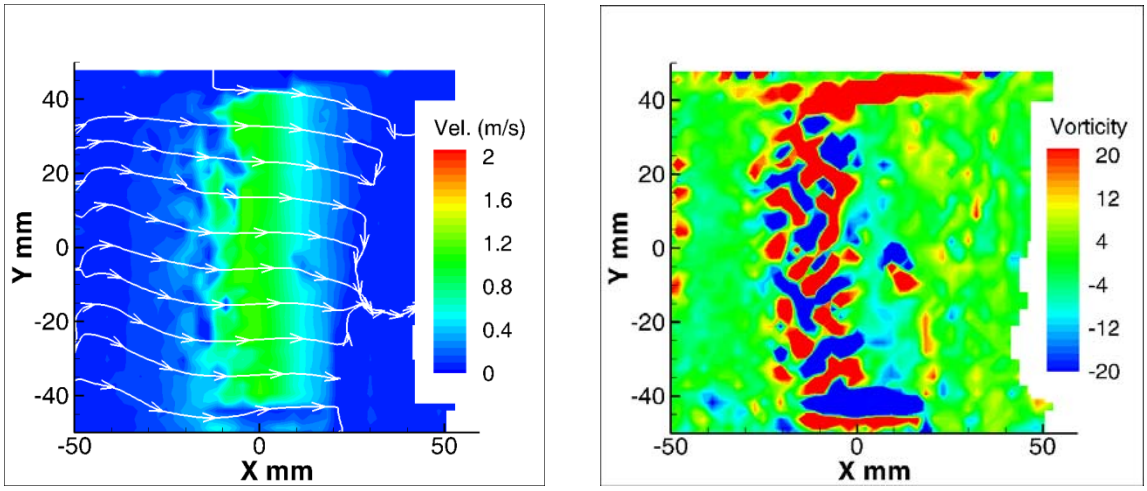

Figure 30 Velocity and vorticity contours of atmospheric air case – 12.7 mm deviation

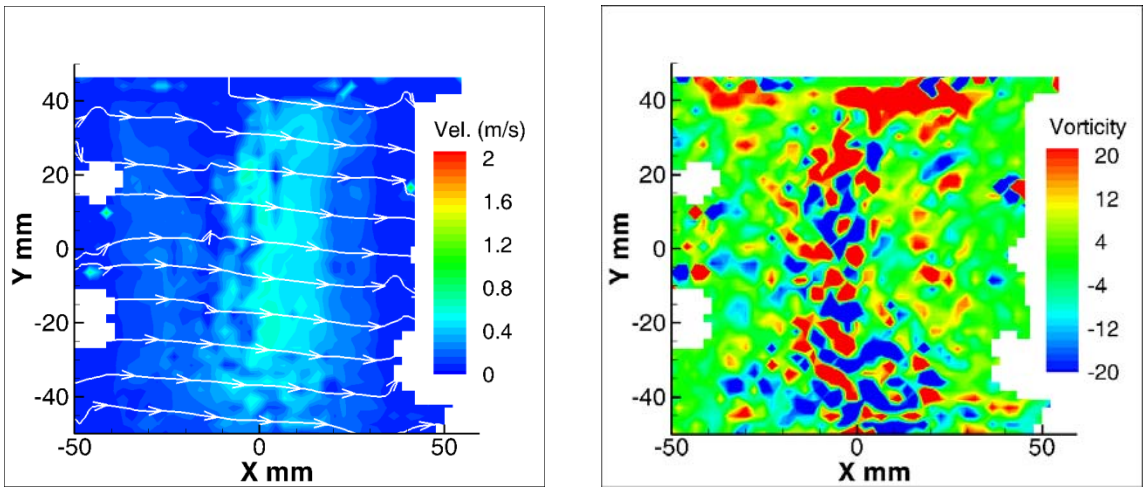

Figure 31 Velocity and vorticity contours of atmospheric air case – 25.4 mm deviation

4.1.3 Flow rate effect to the cyclone flow - atmospheric case

One of the performance indicators of a solar reactor is the residence time. The longer the residence time the more chance the hydrogen rich fuel can be dissociated. Because the operating pressure and temperature need to be controlled within the reaction active condition and material tolerance, the only adjustable flow parameter is the volume flow rate. Figure 32, Figure 33, Figure 34 and Figure 35 quantify the effects of changing the main flow rate and wall shielding flow rate respectively to the overall fluid behavior. The percentage of flow rates are adjusted between 50 % and 150 % with respect to the base case using reference CFD settings.

When the main flow rate is manipulated, the result shows that as the main flow rate is decreased to 50 %, the vortex funnel is no longer detectable although the flow field is

still rotational according to the top view measurements. A relatively significant velocity gradient is shown on the bottom right corner of both the contours as a result of a concentrated wall shield flow discharging from the annular slot at the entrance of the reactor.

In the 75 % main flow rate case, the vortex funnel is captured. Compared to the base case the velocity magnitude in the axial direction is weaker, especially when close to the bottom of the vortex funnel. The diameter of the vortex funnel tends to shrink when it approaches the bottom of the reactor. The gradually changing magnitudes in the vertical direction shows an accelerating tendency in the vortex funnel when the fluid approaches the exit, implying a drawing effect to the fluid from the periphery to the vortex funnel. A vortex line is clearly defined by the large gap between the stable vortices structures on the two sides of the vortex line. On the vortex line no velocity gradient is detected.

When the main flow rate is increased to 125 %, a stronger vortex funnel with higher axial velocity magnitude along the vortex line is captured. Velocity fluctuations start to emerge in the periphery region between the edge of the vortex funnel and the inner wall. In the vorticity contour lots of local vortices exist in this region compared to the previous flow rate results. The outer edge of the vortices that determine the vortex line are shattered and connected to the local vortices, which implies a local scale phenomena of fluid turning from a primarily horizontal rotating motion around the periphery region to an axial motion toward the vortex funnel. It’s noticed that a transverse stripe across the

flow field is caused by the light sheet reflection. The particle information is thus blocked and shows zero velocity.

The fourth case shows the contours when the flow increases to 150 % of the main flow rate. A large scale of fluid turning due to higher rotating speed compared to the previous case is detected. As the rotating speed further increases, the drawing effect to the fluid from the periphery to the vortex funnel becomes stronger following the potential flow theory. The vorticity contour also shows that in order to compensate the vacancy of the peripheral fluid that goes to the vortex funnel, a secondary flow that carries fluid reversely from near the exit toward the entrance zone of the reactor is captured. Compared with the previous contours of weaker main flow rates, when the vortex funnel is moving upward, the vortices on the left side of periphery region of the contour should be positive in red instead of negative in blue according to velocity gradient distribution. Between the up-moving vortex funnel flow and the reversed secondary flow, there's a neutral fluid layer acting as a transition buffering zone.

In this case, when the rotating speed increases by increasing the main flow rate, the scale of the vortex funnel maintains the same, the velocity gradient in the up-moving jet passage increases, therefore beyond the limitation of PIV dynamic range, no higher central velocity vectors are detected compared to the previous case. A slight tilt of the vortex funnel by 2.3° from the bottom right to top left of the image is detected as a result

of the non-uniform distribution of the wall shield flow shown in the 50 % main flow case.

According to the results of measurements, an overlapped comparison of axial velocity vector profiles of changing the main flow rate is shown in Figure 36. It proves the existence of the reversal secondary flow with maximum magnitude at 30 mm of radius from the vortex line. The neutral fluid layer exists at location range between 10 mm – 20 mm radius. The maximum axial velocity is proportional to the main flow rate except the lowest main flow rate case because of the viscosity-dominated effect. But even the lowest main flow rate case also show the existence of the secondary flow at the same position of radius as the rest of the three cases.

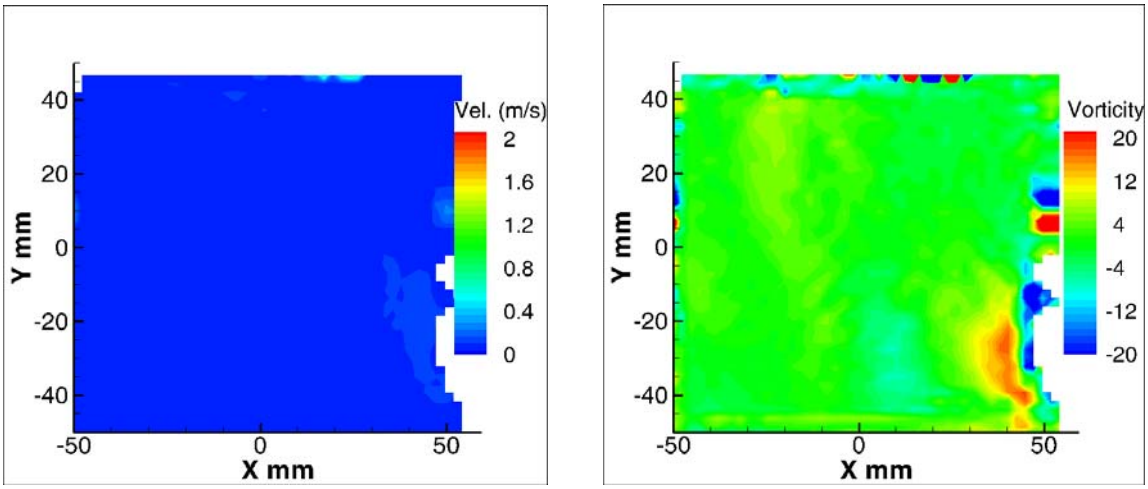

Figure 32 Velocity and vorticity contours of atmospheric case – 50% main flow

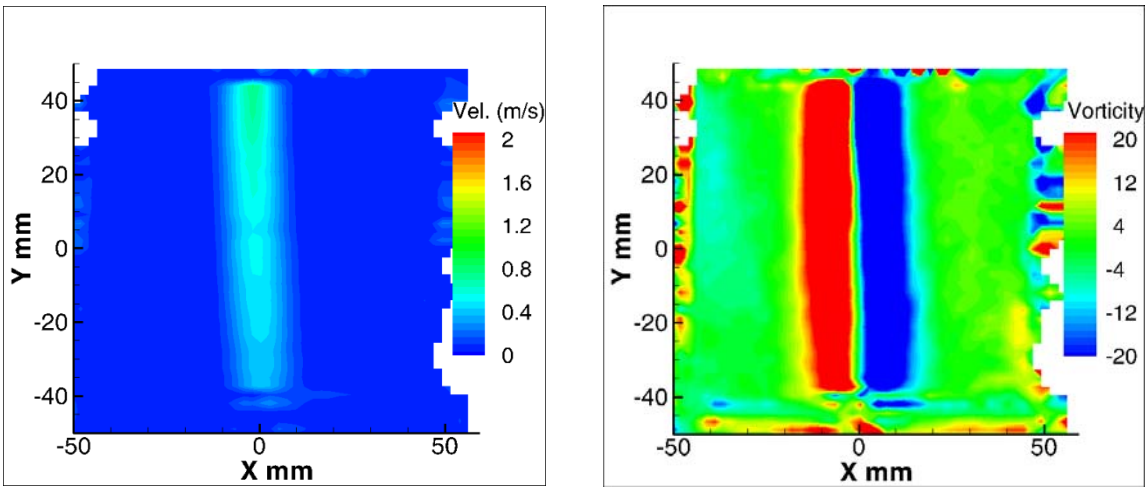

Figure 33 Velocity and vorticity contours of atmospheric case – 75% main flow

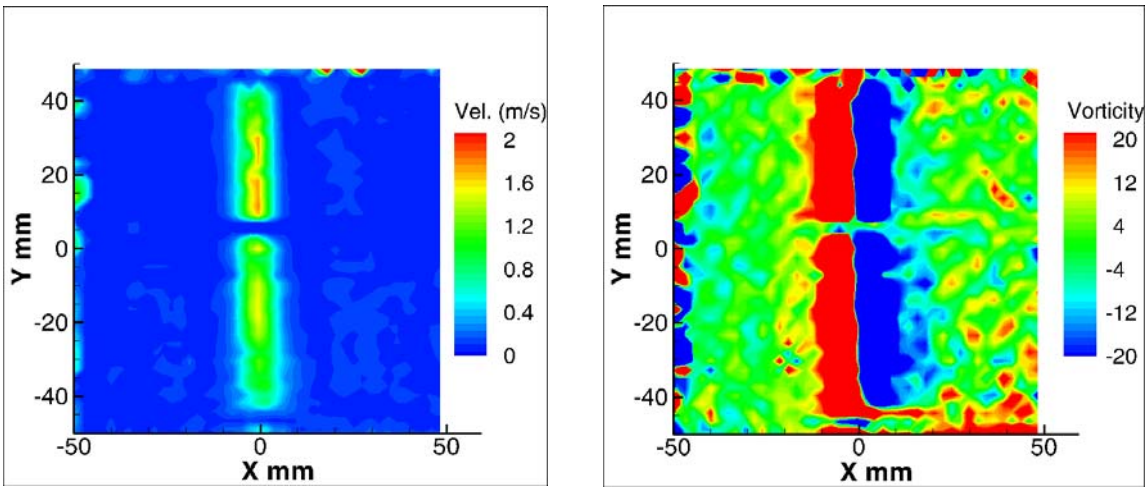

Figure 34 Velocity and vorticity contours of atmospheric case – 125% main flow

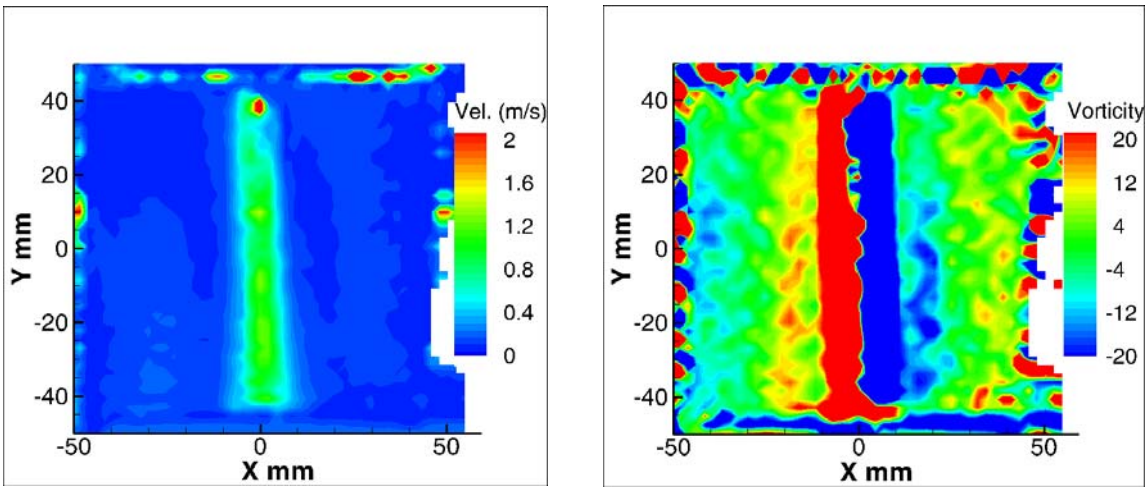

Figure 35 Velocity and vorticity contours of atmospheric case – 150% main flow

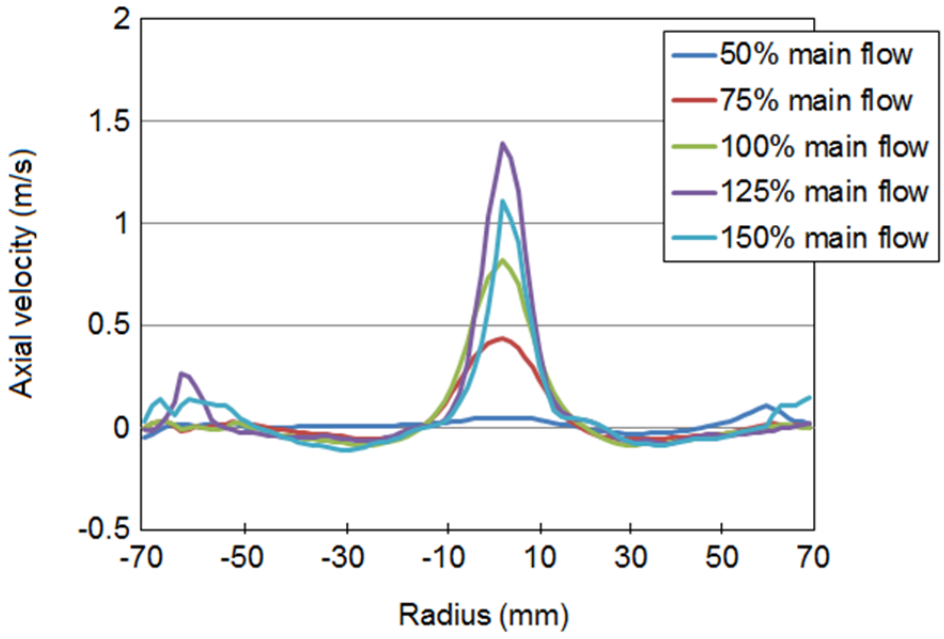

Figure 36 Axial velocity magnitude extracted from the side view

In order to investigate the effect of the wall shield flow to the overall fluid behavior, the wall shield flow rate is manipulated shown in the Figure 37, Figure 38, Figure 39 and

Figure 40. When the flow rate is decreased to less than 100 %, the vortex funnel is stable with a clearly defined vortex line in the vorticity contours. The secondary flow is detected although the fluid turning is mitigated. When the wall shield flow rate increases to more than 100 %, the vortex funnel begins to destabilize due to the over-disturbance of the wall shield flow. The reversal secondary flow is disrupted and shrunk by the wall shield flow. Without enough supply by the secondary flow, the continuity of the vortex line becomes intermittent instead of a clear continuous path. When the wall shield flow reaches 150 %, the flow field becomes wall shield flow dominated. The secondary flow is no longer detected. The vortex funnel starts to collapse due to the lack of supply from the secondary flow. The above observations indicate that when the wall shield flow is less than the CFD setting, the flow field is dominated by the main flow, otherwise the flow field will become wall shield flow dominated.

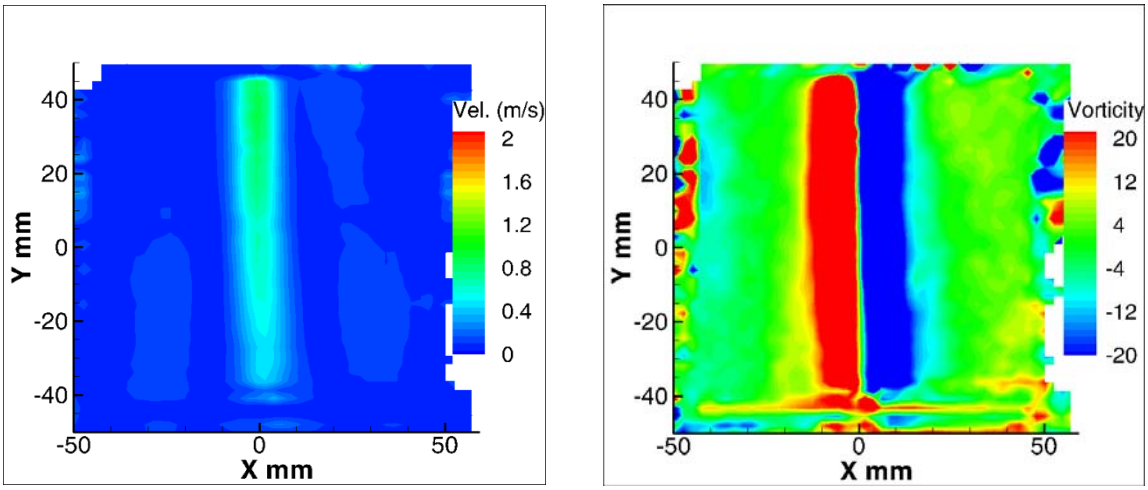

Figure 37 Velocity and vorticity contours of atmospheric case – 50% wall shield flow

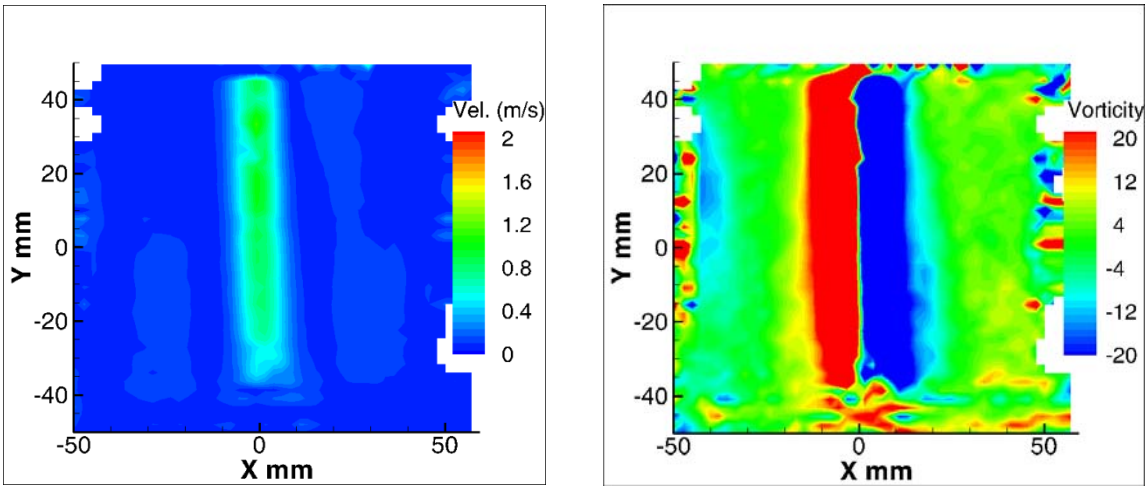

Figure 38 Velocity and vorticity contours of atmospheric case – 75% wall shield flow

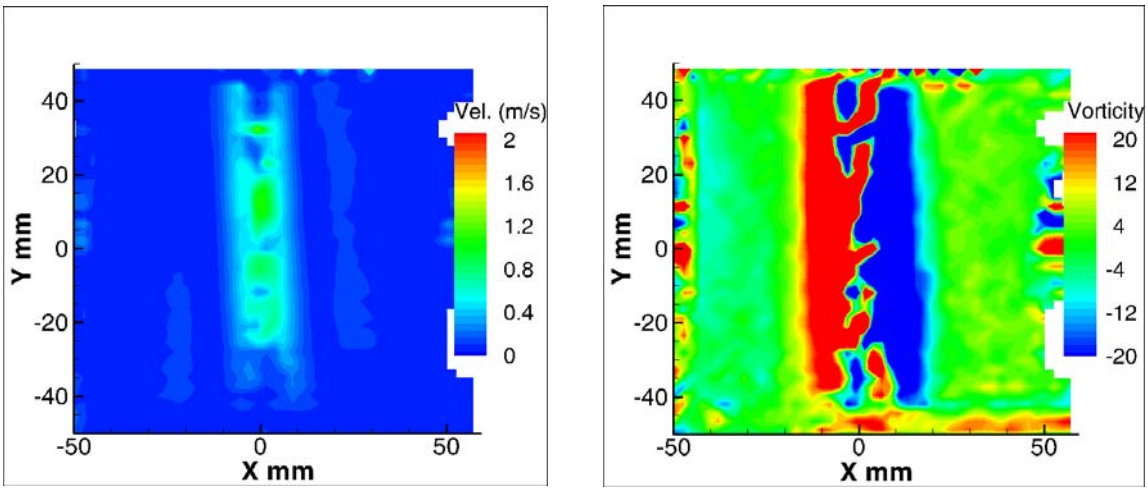

Figure 39 Velocity and vorticity contours of atmospheric case – 125% wall shield flow

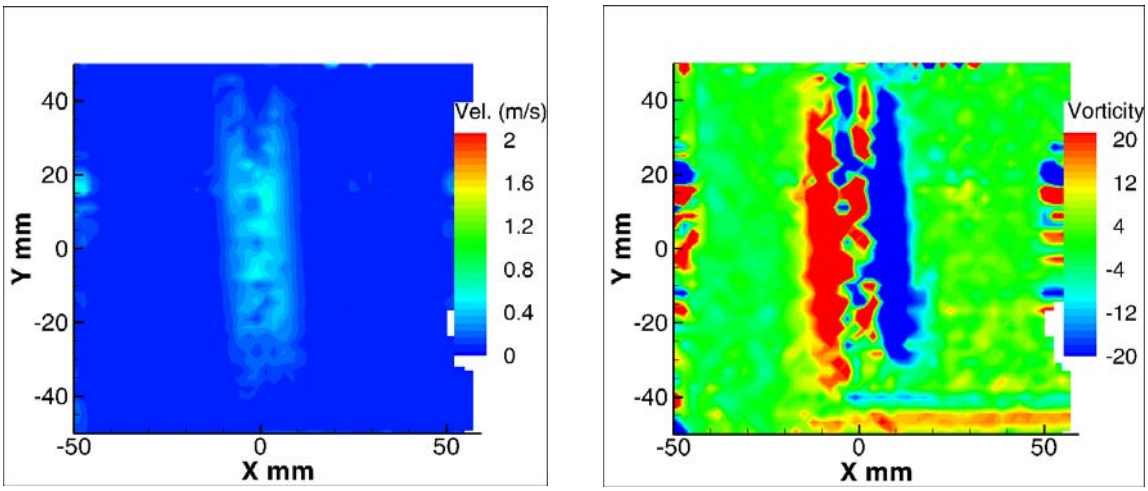

Figure 40 Velocity and vorticity contours of atmospheric case – 150% wall shield flow

Since the change of the main flow rate has major impact on the fluid behavior while the wall shield flow primarily affect the stability of the cyclone structure, a series of PIV top view images of the tangential component subjected to the main flow variation are shown in Figure 41, Figure 42, Figure 43, Figure 44 and Figure 45. The tangential components show a forced-free (Rankine) vortex feature since the fluid dynamics around the center of the vortex funnel is dominated by viscous effect. The fluids in opposite directions on the two sides of the vortex line counteract each other by shear. The rest of the periphery fluid is dominated by angular momentum conservation and approximates potential flow profile due to less viscous effect at lower tangential velocities. When the main flow is more than 100 %, the fluid velocity at the center of the vortex funnel are primarily in the axial direction and therefore, the tangential velocity magnitudes in that region approximate to zero. The drawing effect proportional to the flow rate also exists in the

top view image. As is mentioned, some artificial vortices caused by local noise are captured in the flow field. The vector-free area is filled with black color.

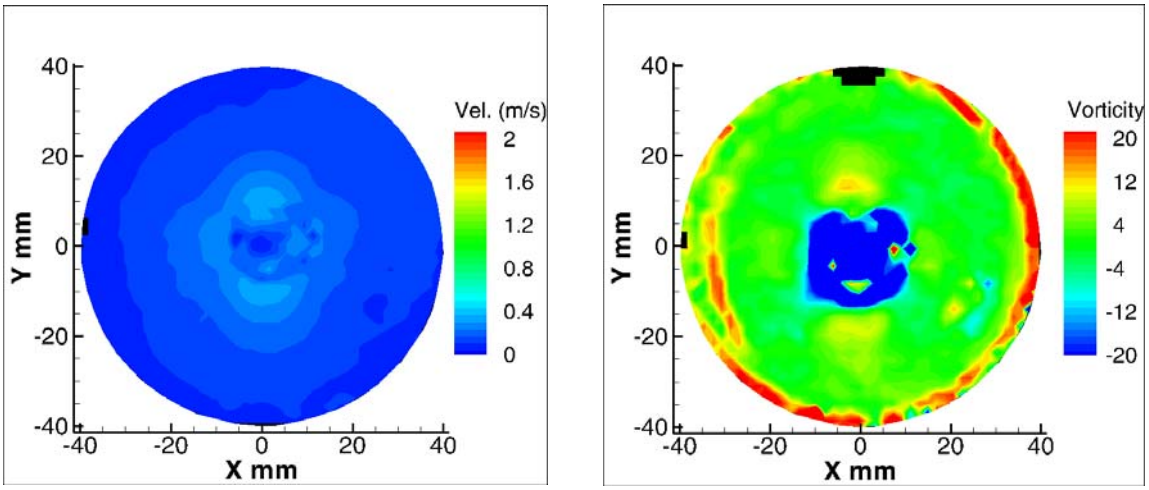

Figure 41 Velocity and vorticity contours of atmospheric case – 50% main flow

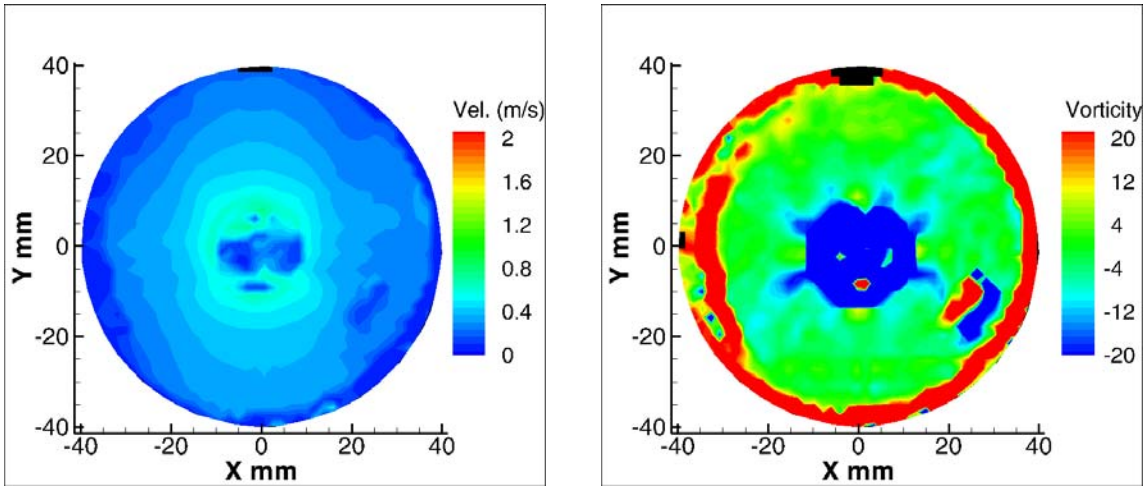

Figure 42 Velocity and vorticity contours of atmospheric case – 75% main flow

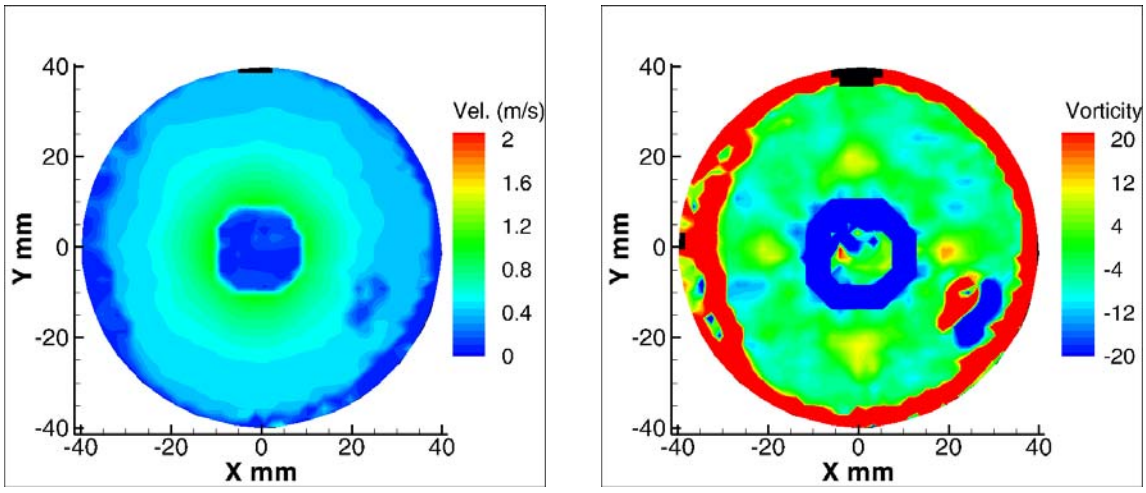

Figure 43 Velocity and vorticity contours of atmospheric case – 100% main flow

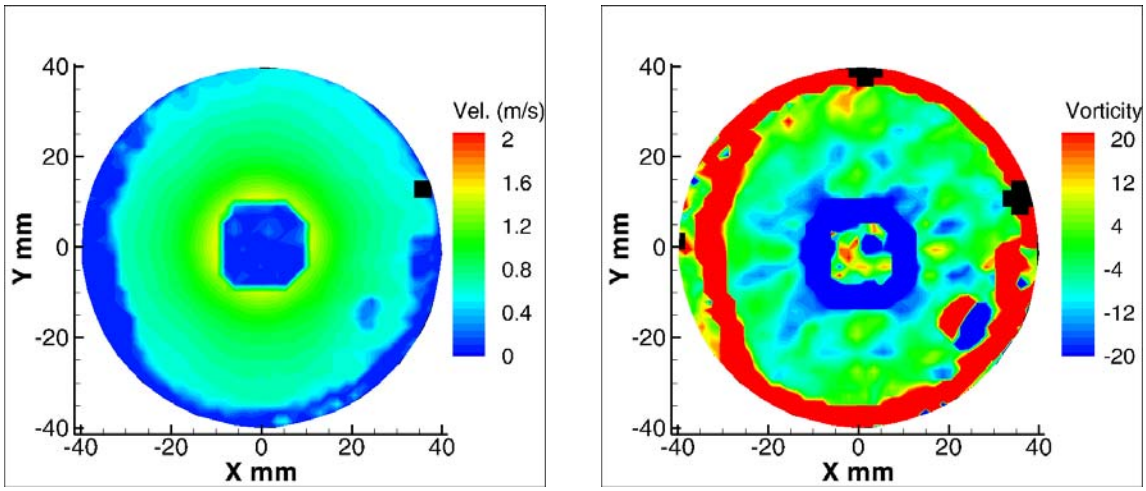

Figure 44 Velocity and vorticity contours of atmospheric case – 125% main flow

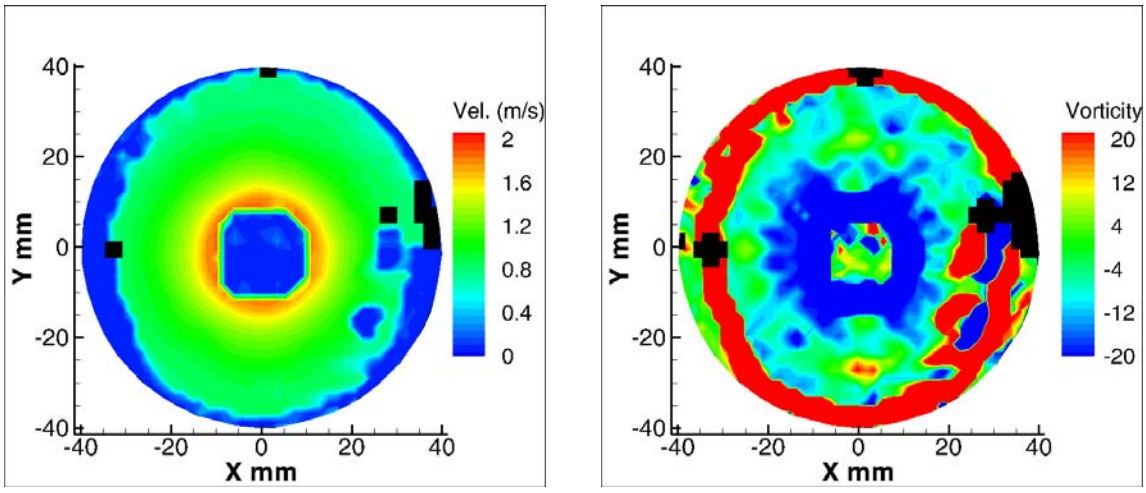

Figure 45 Velocity and vorticity contours of atmospheric case – 150% main flow

The rotational flow dynamics due to the main flow rate variation is shown in Figure 46 and Figure 47. The axial symmetry of the tangential profiles is observed. The maximum magnitude is proportional to the main flow rate. A superposition of vortex funnel edge is observed when main flow rate increases.

At the location of 12.7 ± 0.5 mm radius, the tangential velocity of the 100 % main flow case is 0.99 m/s and is equal to the tangential velocity from the previous deviated side view velocity contour. At radius of 25.4 ± 0.5 mm, the velocity is 0.51 m/s and is again matched with the deviated side view contour. The relative positioning error can come from the accuracy during the data extraction in the top view image and vector line-averaging in the side view image.

When apply the formulation $V_{\tan} \cdot r^n = C$ to fit the free vortex portion of the tangential profiles, the exponential n falls in between 0.66 and 0.76 compared with 0.4 - 0.8 by Cortes (2007), except the 50 % main flow case with the n value of 1.24 larger than the theoretical value, 1 ,indicating that the tangential momentum is too weak because of the viscosity-dominated effect. When the same procedure is applied within the forced vortex funnel, n falls in between -0.8 and -1.08 with respect to -1 for a theoretical forced-vortex.

The swirl number of the cyclone flow field is calculated by extracting the flow data according to the definition of the non-dimensional formulation

$$S_n = \frac{G_\theta}{RG_x} = \frac{\int_0^R u_{axial} u_{\tan} r^2 dr}{R\int_0^R u_{axial}^2 r dr}$$

where G_θ is the axial flux of tangential momentum, G_x is the axial flux of axial momentum, R is the radius of the reactor window. The swirl numbers are 3.34 in the 50 % main flow case, 1.26 in the base case and 2.64 in the 150 % main flow case. The reason the 50 % case has the highest swirl number is that the axial velocity is almost zero due to the insufficient fluid rotation. It's noticed that the flux integrals in the formulation are always taken positive in the secondary flow region where the fluid axial velocities are negative.

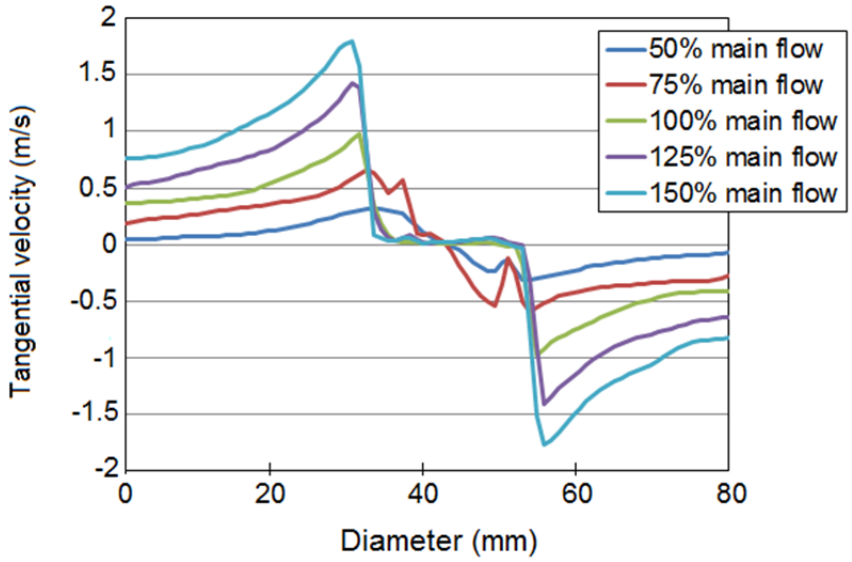

Figure 46 Symmetry of the tangential velocity profiles from the top view image

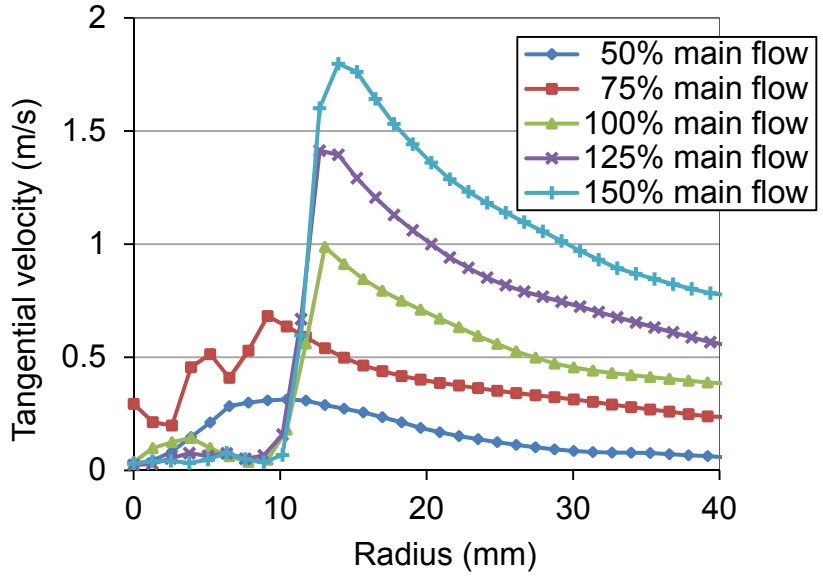

Figure 47 Tangential velocity magnitude extracted from the top view image

Since the pressure-velocity coupling dominates the vortex profile, by putting the velocity profiles obtained into the cylindrical momentum equation, the static pressure variation

can be estimated. Only the force balance between the centrifugal force and the pressure gradient terms is considered to simplify the problem

$$\rho \frac{V_{\tan}^2}{r} = \frac{dP}{dr}$$

After integration and piecewise summation the equation can be rewritten as

$$P(r) = P_0 + \rho C_1^2 \frac{r_{peak}^{2n_1}}{2n_1} + \rho C_2^2 \left[\frac{1}{2n_2 r_{peak}^{2n_2}} - \frac{1}{2n_2 r^{2n_2}} \right]$$

where the subscript 1 and 2 refer to the variables in the forced vortex and free vortex ranges respectively. The normalized static pressure variations are shown in Figure 48. The deviated profile for the 50 % main flow case indicates weak fluid momentum.

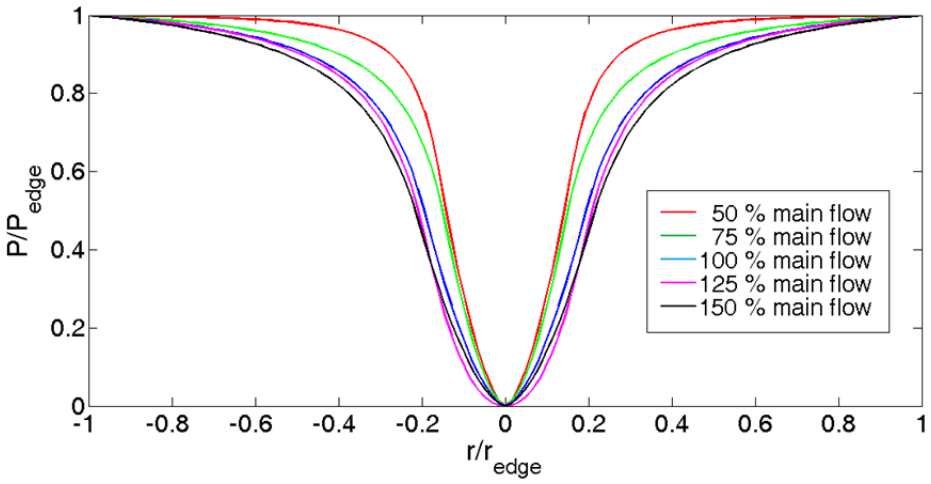

Figure 48 Pressure gradient variations across radius

4.1.4 Residence time

The effectiveness of the methane conversion can be increased by increasing the residence time of the fluid. A longer residence time can be achieved by either reducing the volumetric flow rate or generating stronger vortices that keep the particles in the reactor for a longer time. In calculating the residence time, the axial flow rate is extracted from the center of the vortex to the edge of the velocity contour instead of the total axial flow rate over the entire cross-section of the reactor. It's noticed that the magnitude of the velocity vectors in the region between the edge of the vortex funnel and the wall is relatively small and thus contain larger uncertainty due to the 3-D effect. Also the radius effect further amplifies the error of the axial flow rate in that region. During the visualization of the particles in the PIV capture, the tracking particles accumulate to higher particle concentration surrounding the vortex line. Since the residence time is used to determine the optimal flow setting to solve the carbon particle clogging problem, it's reasonable to consider all available flow regions and flow characteristics in calculating the axial flow rate. A flow rate ratio s defined as the ratio of circulating flow rate to the total axial flow rate is evaluated to quantify the resident time.

$$s = \frac{\sum \left(u_{\tan} \cdot r \right)}{\sum \left(u_{axial} \cdot r \right)}$$

where $u_{\tan}$ and u_{axial} are the tangential and axial velocity at the corresponding radius r. The number s can be used to obtain the maximum swirling effect to represent the residence time. Figure 49 shows the result of the flow rate ratio versus the main flow rate. The result indicates the flow rate ratio reaches a local maximum when the main flow rate is 75 % of the reference CFD case setting, which implies this is the optimal setting for increasing the residence time to avoid too strong axial and rotational flow rates beyond this point. By treating the flow rate ratios as intensities, a sub-pixel estimator can be applied by taking advantage of the neighborhood values, the result shows that the optimal percentage of main flow rate is 82.3 % using peak centroid estimator, 79.3 % using parabolic peak estimator and 82.8 % using Gaussian peak estimator.

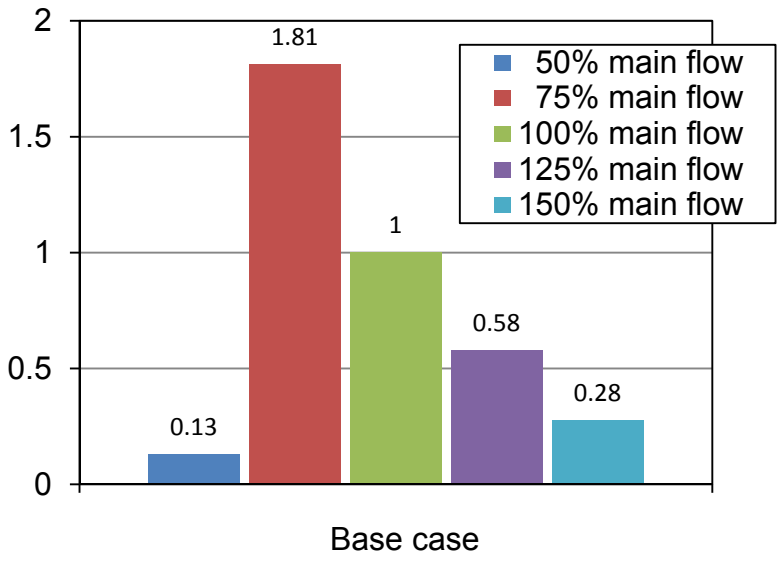

Figure 49 Flow ratio of tangential and axial components normalized with the base case

4.1.5 Cyclone flow field reconstruction

4.1.5.1 Atmospheric case

In order to explore the whole cyclone flow structure, the PIV measurements are performed on eight cross section planes shown in Figure 50 and Table 7. The positions of the light sheet and the camera are remained fixed while the reactor moves with the traverse. In the top view capture, the pinhole effect exists when the distance between the reactor and the camera changes. Therefore, the captured flow fields are compared with a pinhole model according to the reactor geometry. The fixed distance between the light sheet and camera is 558.8 mm (22 inch). The offset between the reactor window and the 0 mm (0 inch) traverse position is 17.907 mm with 1.1 % RMS error. This positioning error between the original data and the pinhole model comes from manual data extraction. The physical diameters of the flow field through the 80 mm reactor window change from 82.65 mm at 0 mm (0 inch) position to 101.76 mm at 101.6 mm (4 inch) position. The maximum 1-D image dilation is about 25 %. The calibrated velocity vector fields are shown in Figure 51.

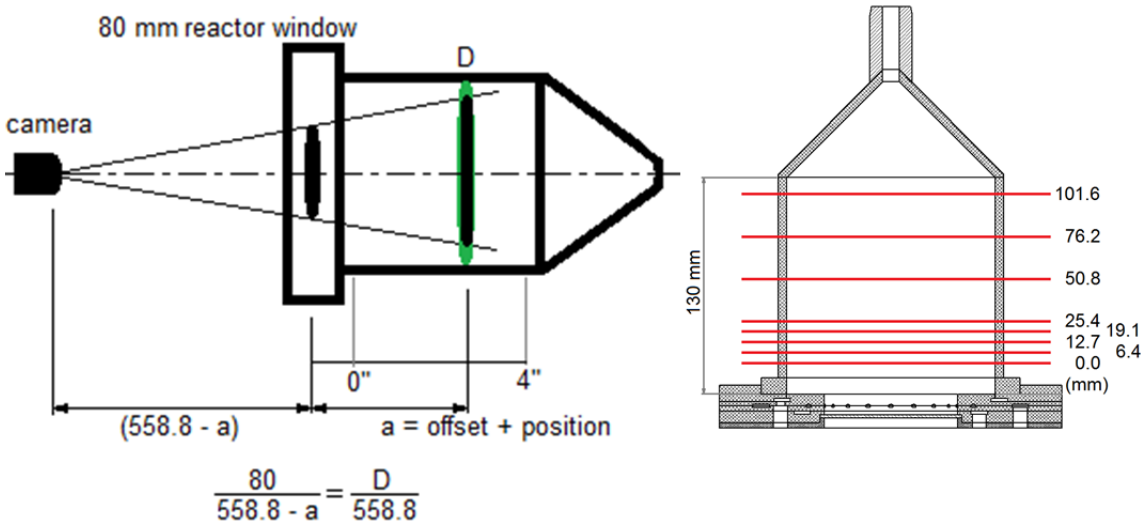

(a) (b)

Figure 50 Top view measurement (a) spatial calibration (b) traverse positions of capture

Cross-section#	Z traverse (mm)	Offset (mm)	Diameter of field of view (mm)
1	0	17.91	82.65
2	6.40		83.63
3	12.70		84.64
4	19.10		85.67
5	25.40		86.72
6	50.80		91.22
7	76.20		96.20
8	101.60		101.76

Table 7 Spatial calibration for atmospheric air case due to pinhole effect

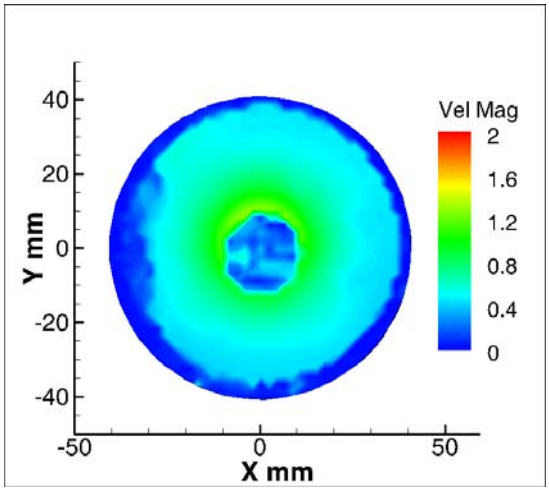

(a)

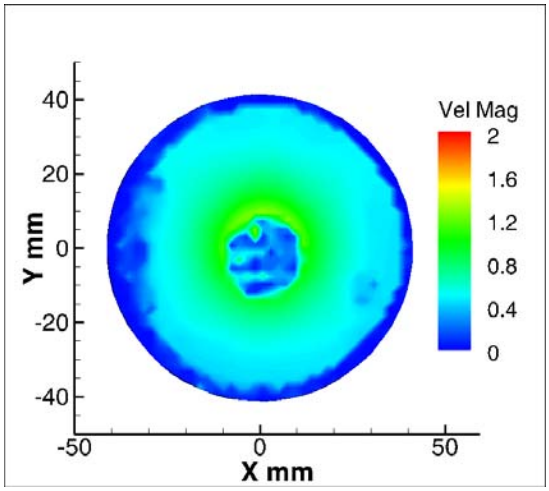

(b)

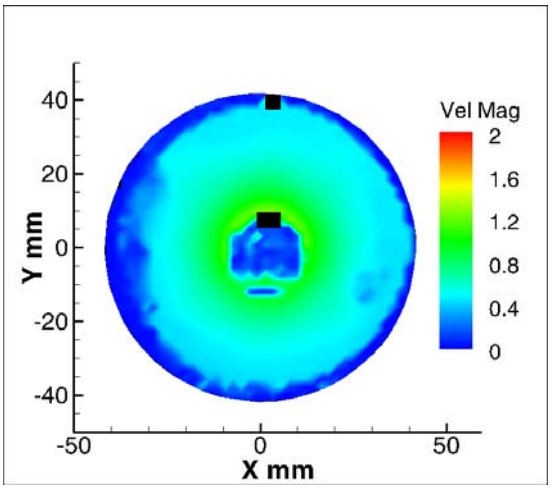

(c)

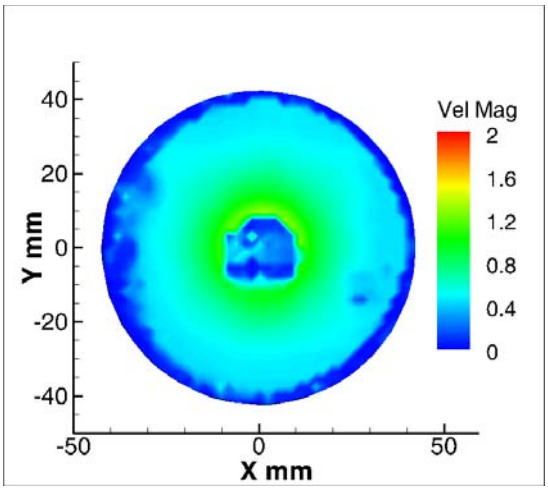

(d)

Figure 51 Calibrated velocity magnitude contours at 8 traverse cross section planes (a) 0 mm (b) 6.4 mm (c) 12.7 mm (d) 19.1 mm (e) 25.4 mm (f) 50.8 mm (g) 76.2 mm (h) 101.6 mm

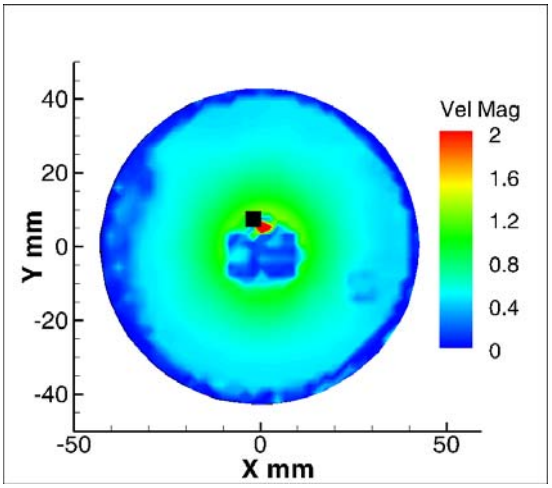

(e)

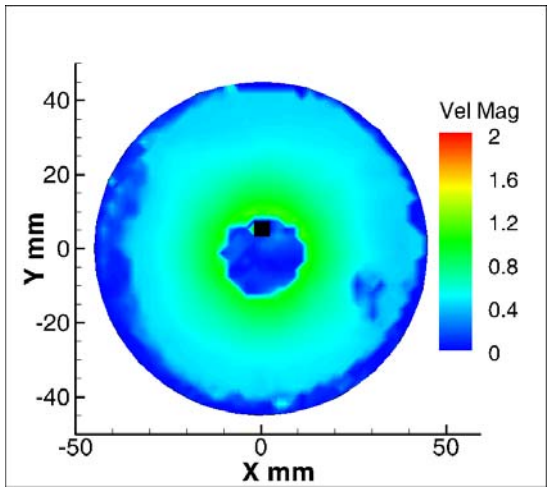

(f)

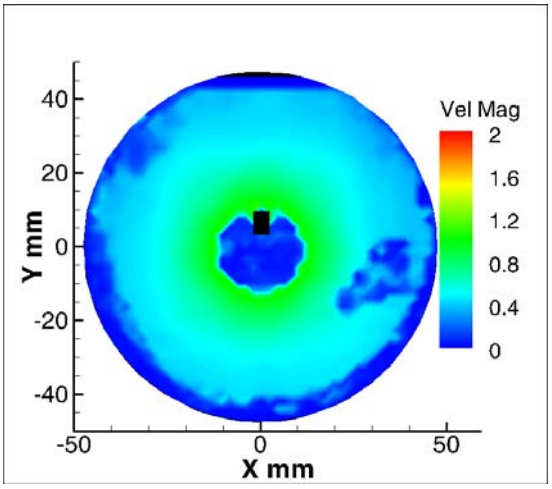

(g)

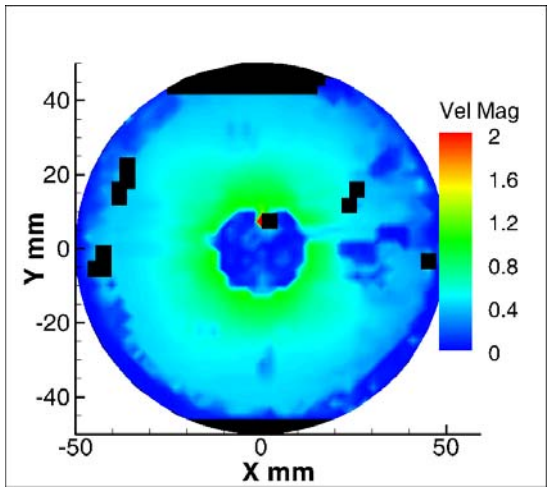

(h)

Figure 51 Continued

The overlapped result as shown in Figure 52 from above contours can provide as a map to reconstruct the rotating flow field. The spatial evolution shows that the diameter of the vortex funnel expands by 8 mm in 101.6 mm axial distance, the resulting tilt angle of the

vortex funnel is about 2.3°, same as the previous calculated value from the side view image. The velocity magnitude decreases along with the expansion indicating a vortex stretching behavior. The tangential velocity profiles in the region between the edge of the vortex funnel and the inner wall tend to be overlapped with each other. The similar decaying profiles imply a synchronized tangential fluid motion at a fixed radius. Therefore the majority of the flow motion in the 3-D space of the reactor except near vortex funnel can be obtained by a single velocity contour. By applying least-square method to $u_{\tan} \cdot r^n = C$, the exponential n is 0.80 instead of 1 in a theoretical free vortex.

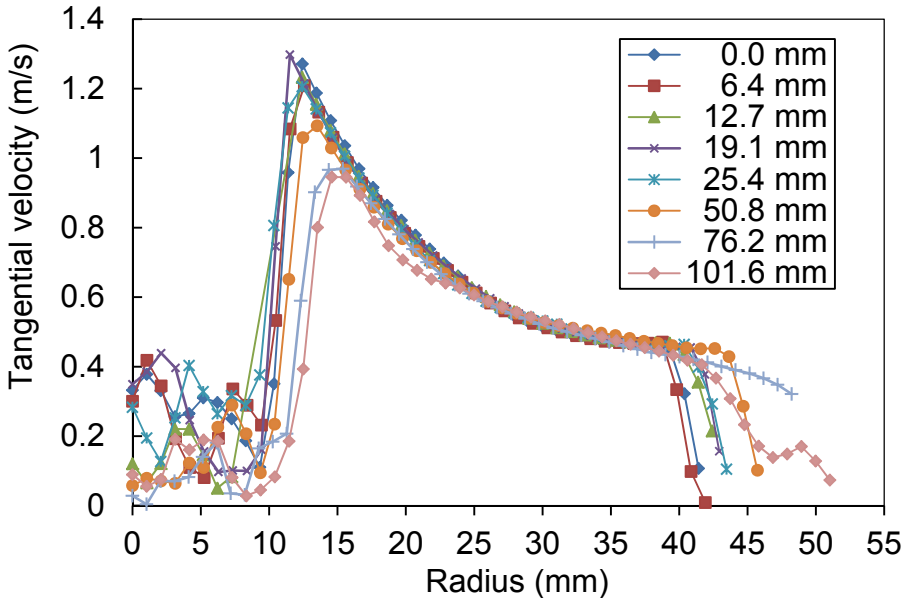

Figure 52 Tangential velocity distributions at 8 capture cross section planes

4.1.5.2 Vacuum case

For the vacuum air case, the velocity vector fields are captured at 33 kPa vacuum pressure in the same fashion. Figure 53, Figure 54 and Figure 55 show the spatial evolution of the flow field on nine traverse cross-section planes spaced by 12.7 mm. It's noticed that the orientation of the Y-Z plane in the following figures is same as that of the X-Y plane in the previous side view measurement.

The corresponding 2-D turbulence intensity is also calculated on an ensemble-averaged base. The contour of lowest velocity magnitude near the geometrical center shows the position of the vortex funnel. The positive vorticity rim at the edge of the vorticity contour indicates the clockwise rotation of the vortex. Table 8 shows a pinhole effect calibration. It's noticed that the offset in this case is different to that of the atmospheric air case. The spacing of capturing cross-sections is fixed to allow observation of a more significant vortex funnel distortion. At cross-section 1 of the image series, a strong jet discharging from the bottom of the image caused by non-uniform distribution of the clockwise main flow is captured. The jet made by 3 of the 18 radial channels carries higher volume flow rate and impinges the inner wall on the far side. The jet is postulated to drive the fluid along the path out of the window viewing range to circulate around the vortex funnel. In the vorticity contour it's seen that at downstream of the jet, the fluid separates from the inner wall, circulates through the geometrical center of the reactor and finally merges with the jet at upstream to complete the circulation. Therefore the

vortex funnel is deviated and tilted from the reactor axis as a result of non-uniform distributions of the main flow and the wall shield flow. The vortex funnel tilts to the –Y direction, same as the tilting profile in the previous side view images.

Cross-section#	Z traverse (mm)	Offset (mm)	Diameter of field of view (mm)
1	0	19.05	82.82
2	12.7		84.82
3	25.4		86.91
4	38.1		89.11
5	50.8		91.43
6	63.5		93.87
7	76.2		96.44
8	88.9		99.15
9	101.6		102.03

Table 8 Spatial calibration for vacuum air cases due to pinhole effect

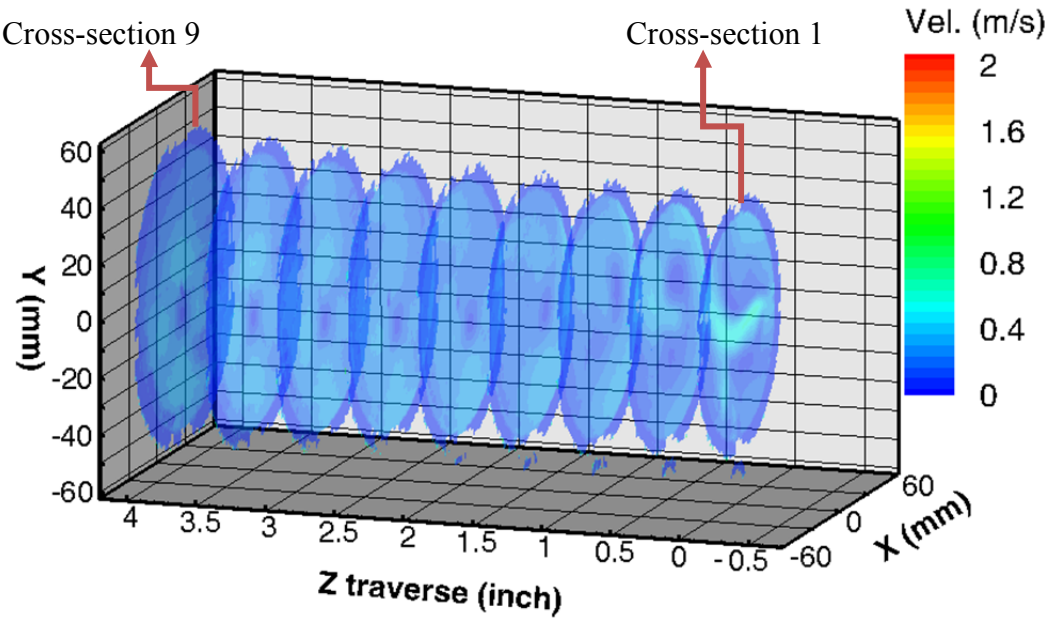

Figure 53 Velocity magnitude contours of 33 kPa absolute case

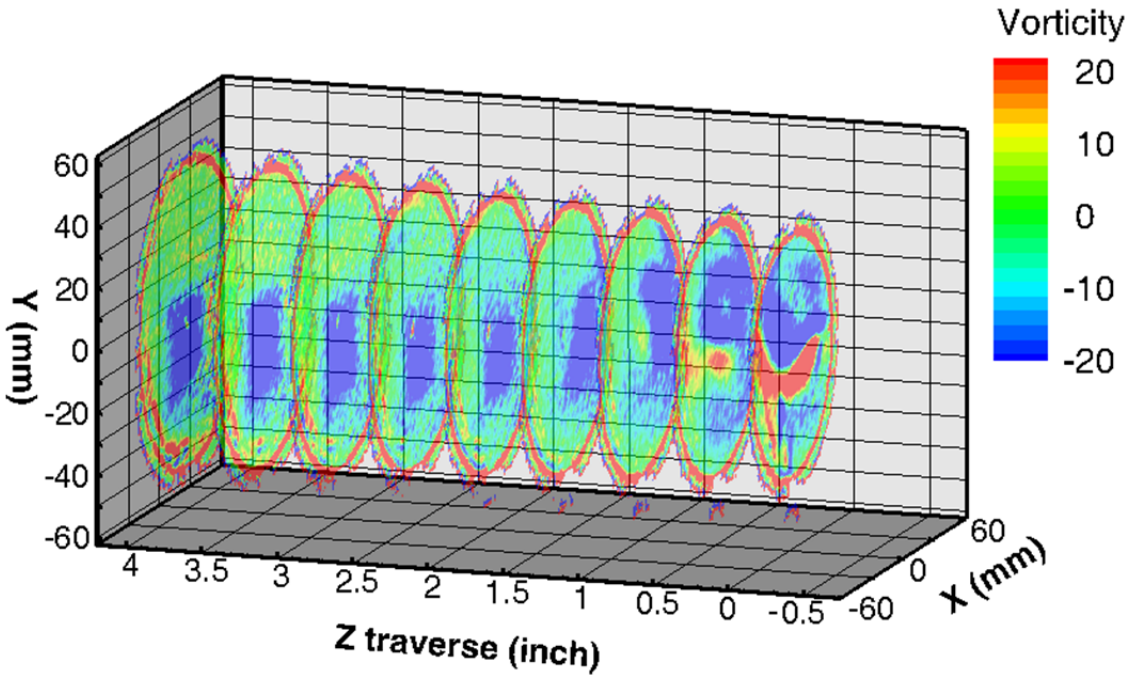

Figure 54 Vorticity magnitude contours of 33 kPa absolute case

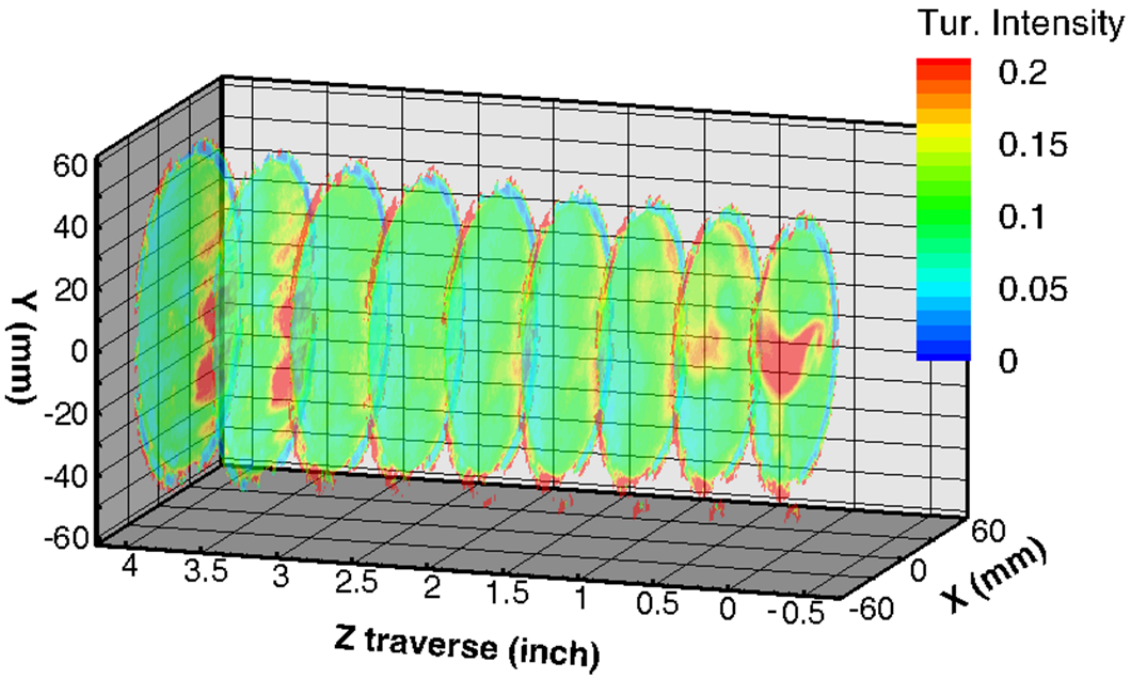

Figure 55 Turbulence intensity contours of 33 kPa absolute case

4.1.6 Pressure effect

In order to relate the operating pressure to the change of the flow dynamics in the reactor, additional vacuum case measurements are performed at 50 kPa and 67 kPa respectively with the same volumetric flow rates for the three inlet flows. The results are shown as follow.

In 50 kPa case, the contours in Figure 56, Figure 57 and Figure 58 show higher momentum level with stronger fluid rotation compared to the contour of the 33 kPa case. The vorticity at the center of the contour is also more concentrated. The non-uniform distribution effect of the main flow jet is reduced, however, the vortex tilting remains due to the influence of the wall shield flow. When the pressure further increases to 67 kPa as shown in Figure 59, Figure 60 and Figure 61, the flow becomes axis-symmetric. The axial flow region with extremely low tangential velocity at the center of the vortex funnel shrinks, surrounded by fluid of high tangential velocity. The vorticity and turbulence intensity contours also show axis-symmetric patterns.

When the pressure recovers to 101 kPa as shown in Figure 62, Figure 63 and Figure 64, the vorticity contour shows a more significant positive vorticity ring in yellow surrounding the negative vorticity in blue at the center. This reversing vorticity ring between 15 mm to 25 mm radius indicates the radial deceleration of the tangential speed taking place around the vortex funnel. The vorticity out of the positive vorticity ring

returns to near zero vorticity magnitude showing the same tendency in the previous tangential velocity distributions.

It's seen that as the operating pressure increases, the flow rotation is enhanced because of the increase of momentum level of the fluid. The tangential velocity is proportional to the operating pressure. The structural integrity of the vortex funnel becomes more concentrated and aligned to the reactor axis by its rotating nature.

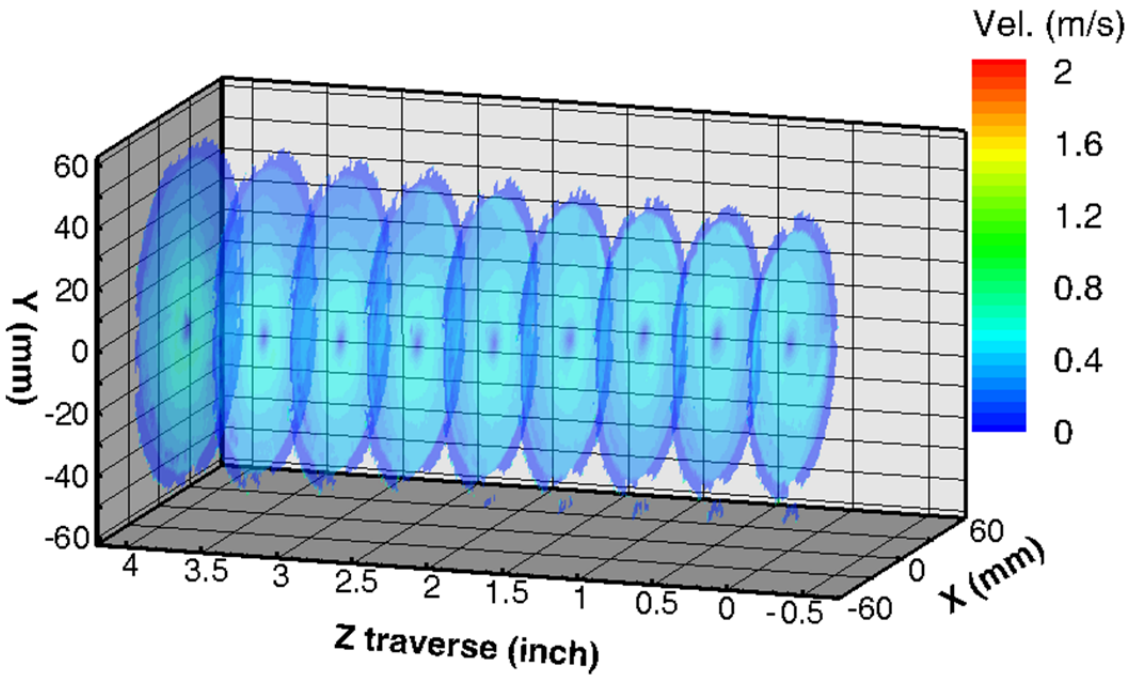

Figure 56 Velocity magnitude contours of 50 kPa absolute case

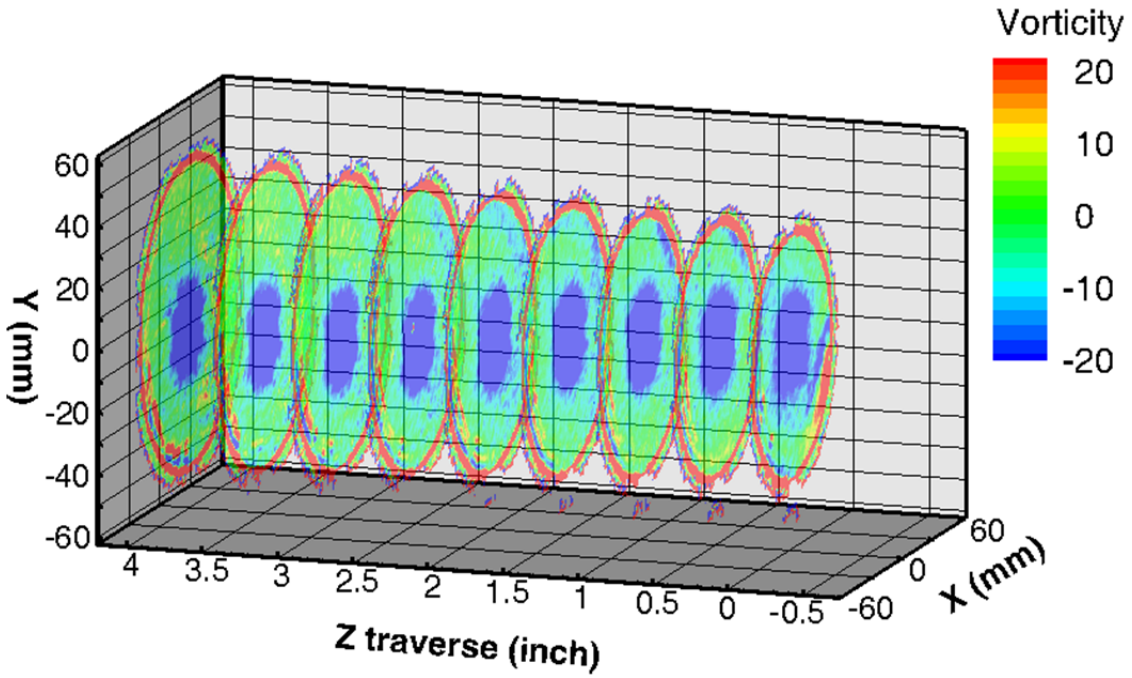

Figure 57 Vorticity magnitude contours of 50 kPa absolute case

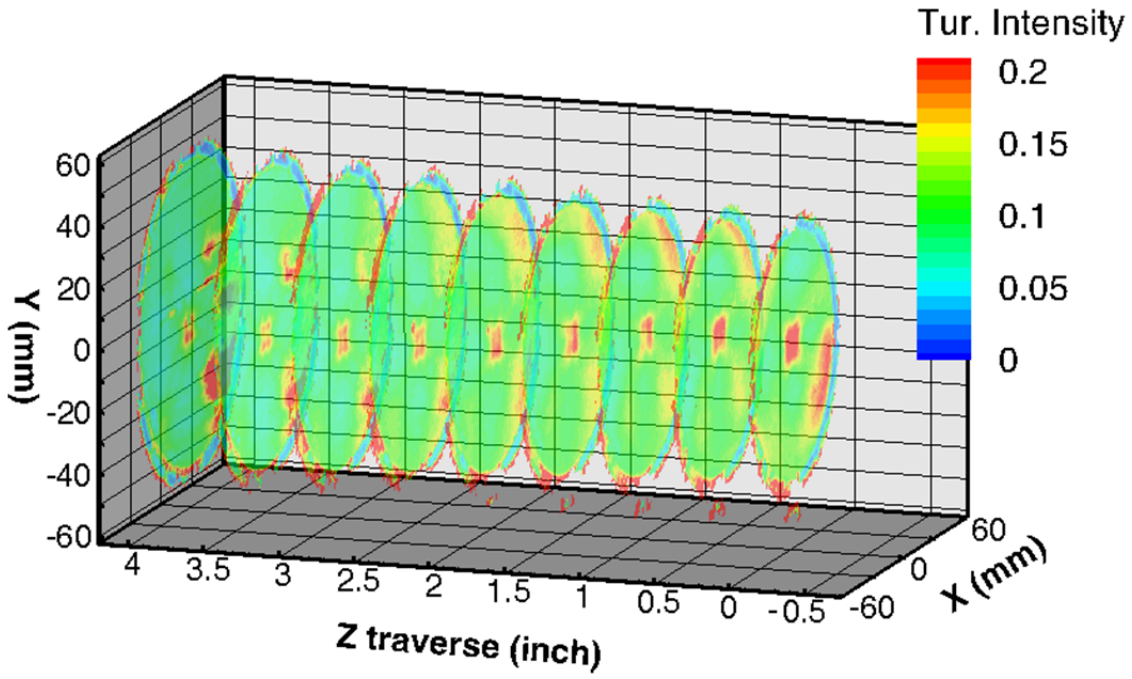

Figure 58 Turbulence intensity contours of 50 kPa absolute case

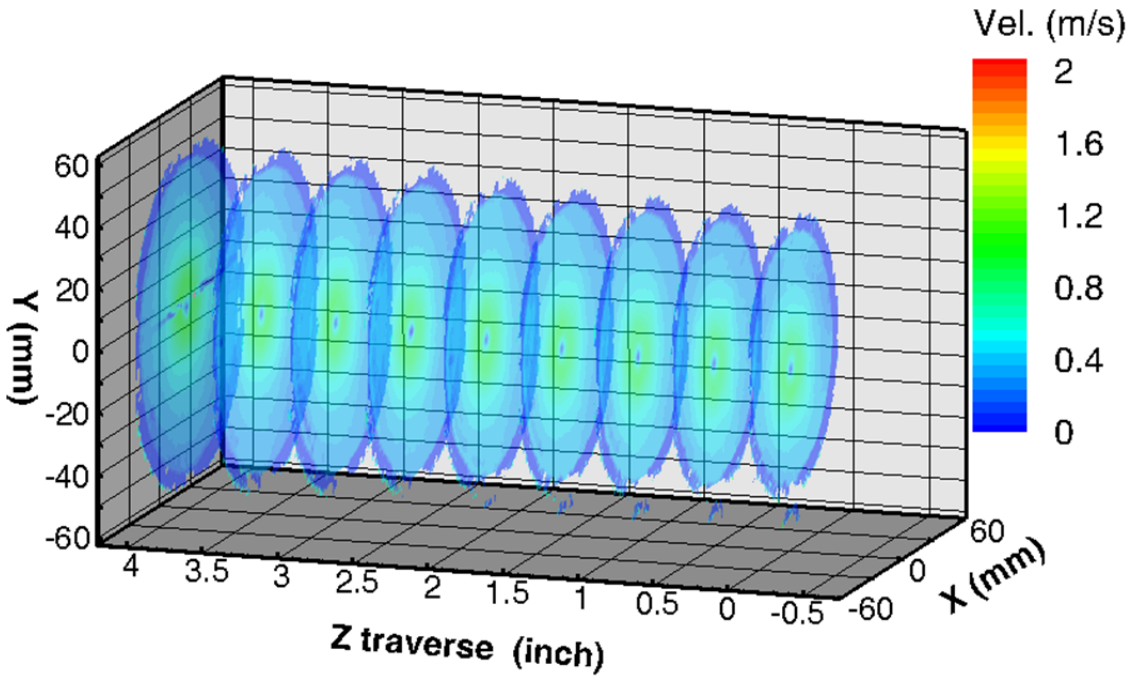

Figure 59 Velocity magnitude contours of 67 kPa absolute case

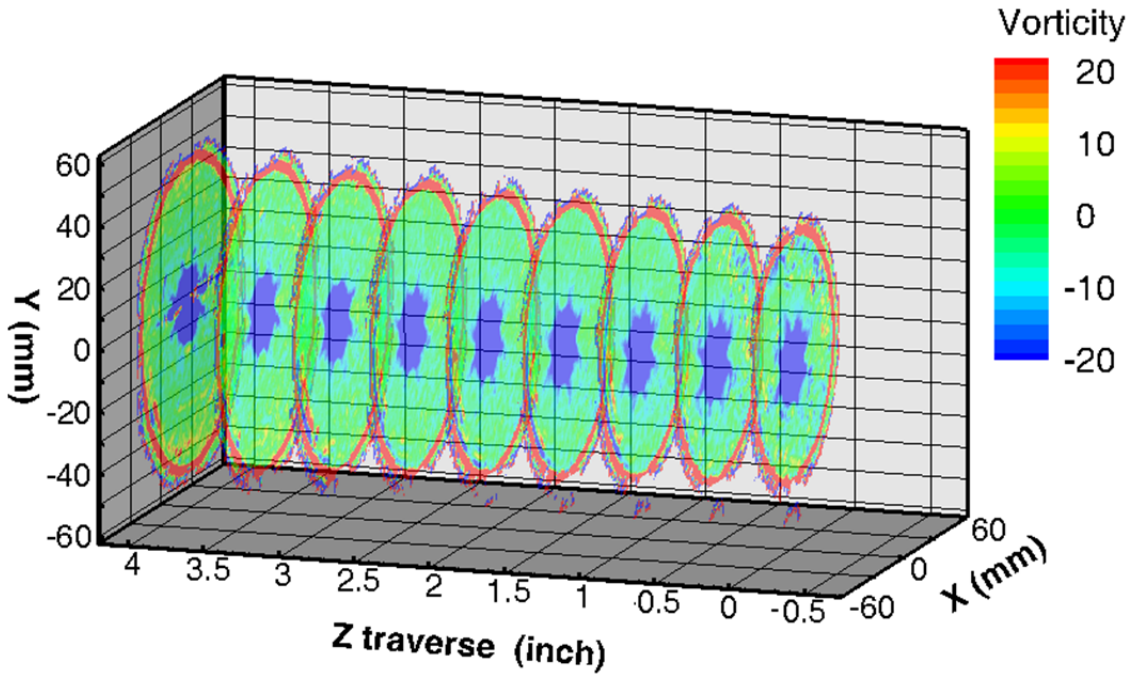

Figure 60 Vorticity magnitude contours of 67 kPa absolute case

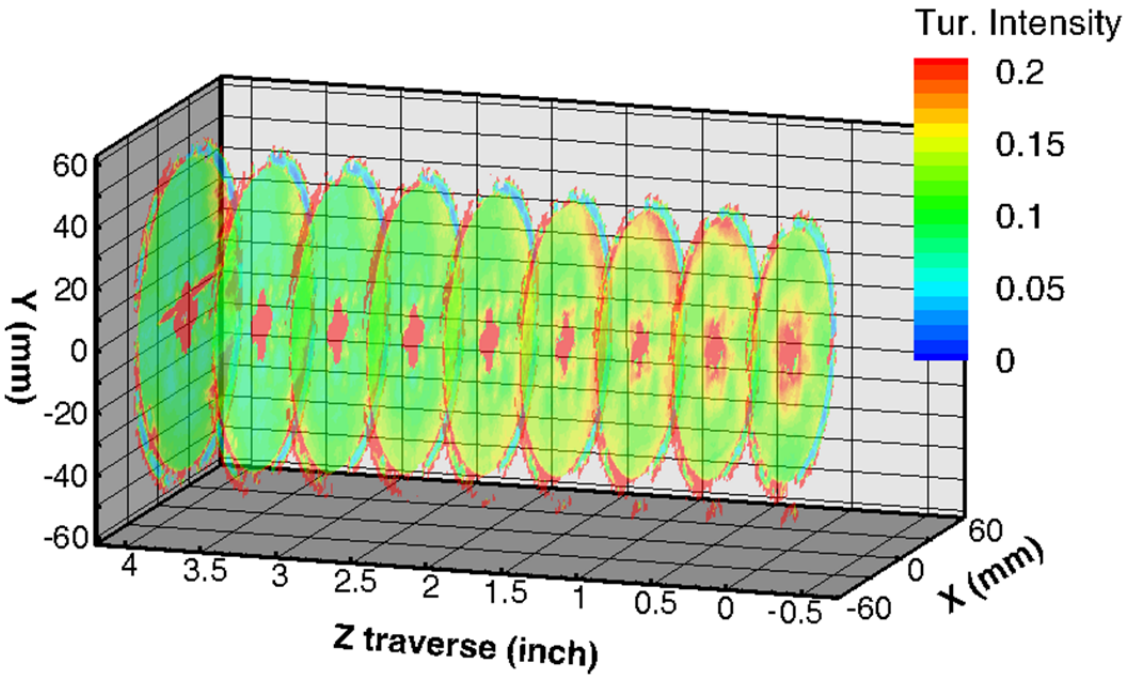

Figure 61 Turbulence intensity contours of 67 kPa absolute case

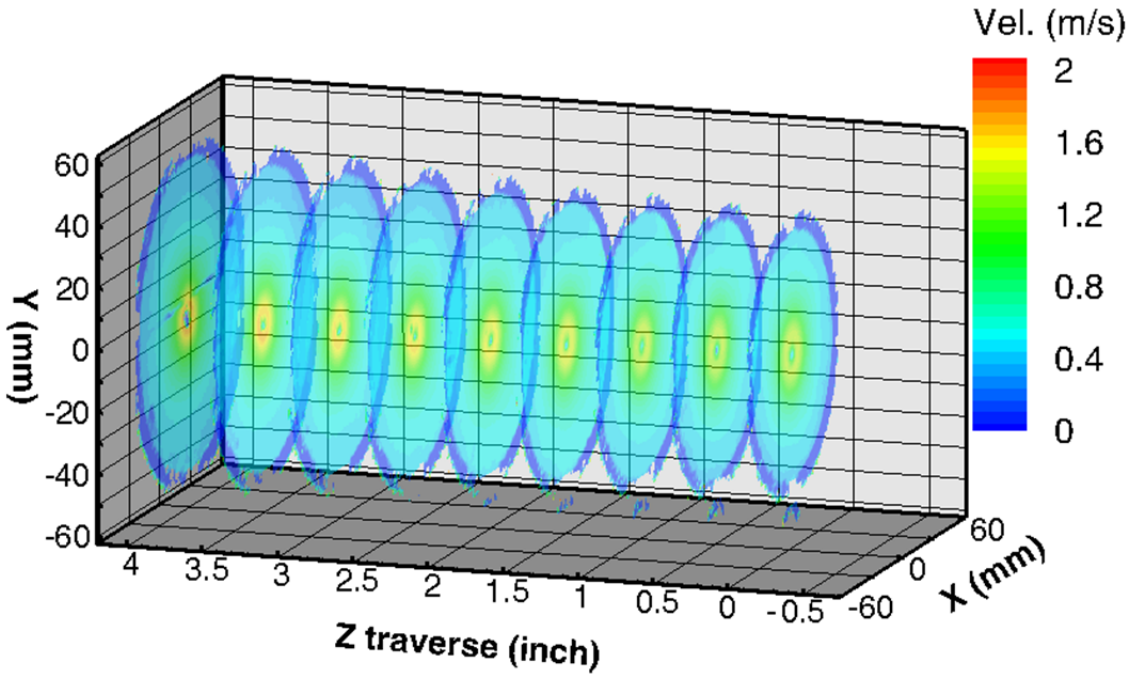

Figure 62 Velocity magnitude contours of 101 kPa absolute case

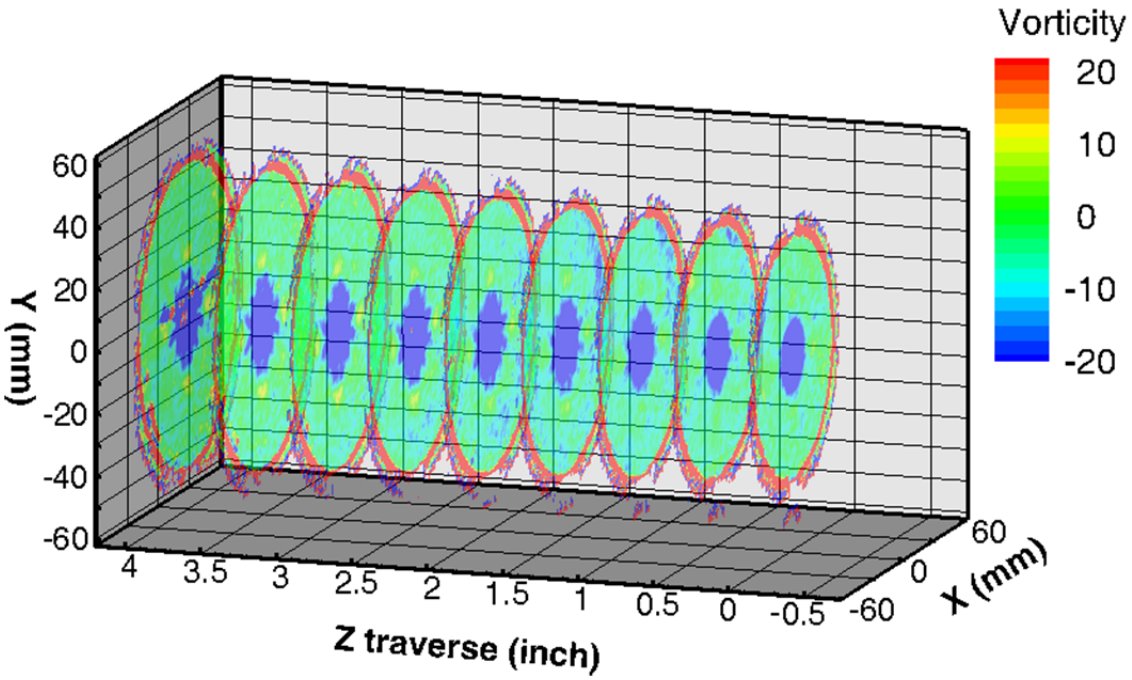

Figure 63 Vorticity magnitude contours of 101 kPa absolute case

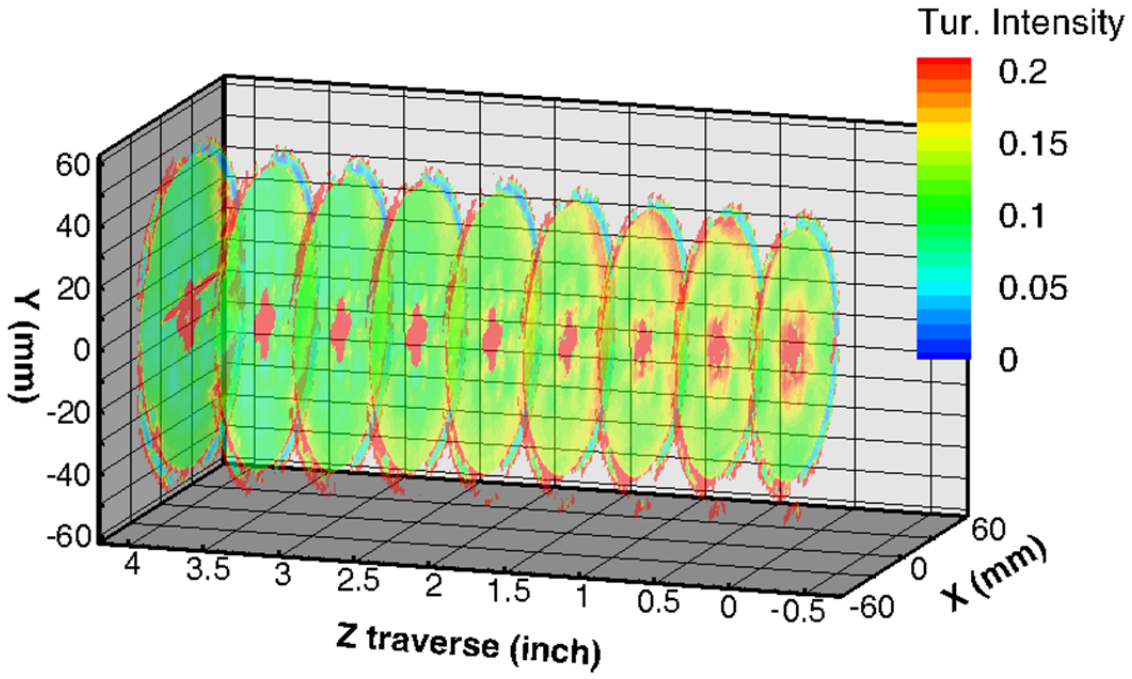

Figure 64 Turbulence intensity contours of 101 kPa absolute case

4.1.7 Flow rate effect to the cyclone flow – vacuum case

In the 33 kPa case, the flow fields at different main flow rates and wall shield flow rates are compared. The main flow rate changes from 50 % to 150 % of the CFD setting, the same strategy is applied to the wall shield flow rate. The results are shown in Figure 65, Figure 66 and Figure 67. It's seen that when the main flow decreases or the wall shield flow increases, the vortex structure starts to collapse, vice versa. The main flow rate is more dominant than the wall shield flow in maintaining the vortex funnel. A larger main flow rate will lead to a more stable vortex funnel aligned to the axis of the reactor while the main flow rate lower than the CFD setting leads to a radially expanded vortex funnel.

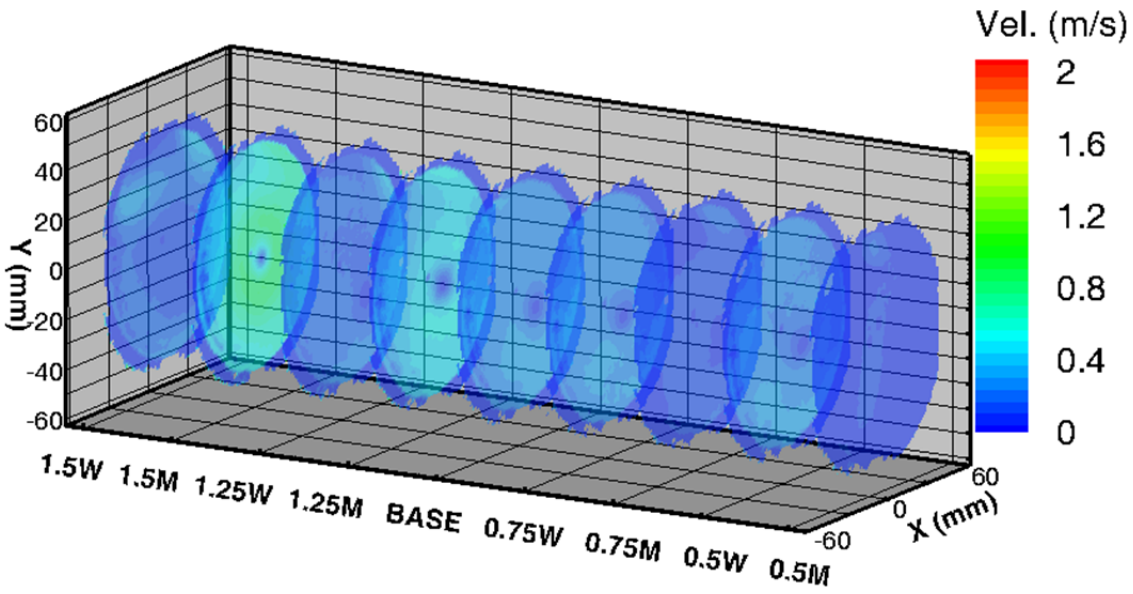

Figure 65 Velocity magnitude contour at different flow rates, from left to right: 150% wall flow, 150% main flow, 125% wall flow, 125% main flow, Base case, 75% wall flow, 75% main flow, 50% wall flow, 50% main flow

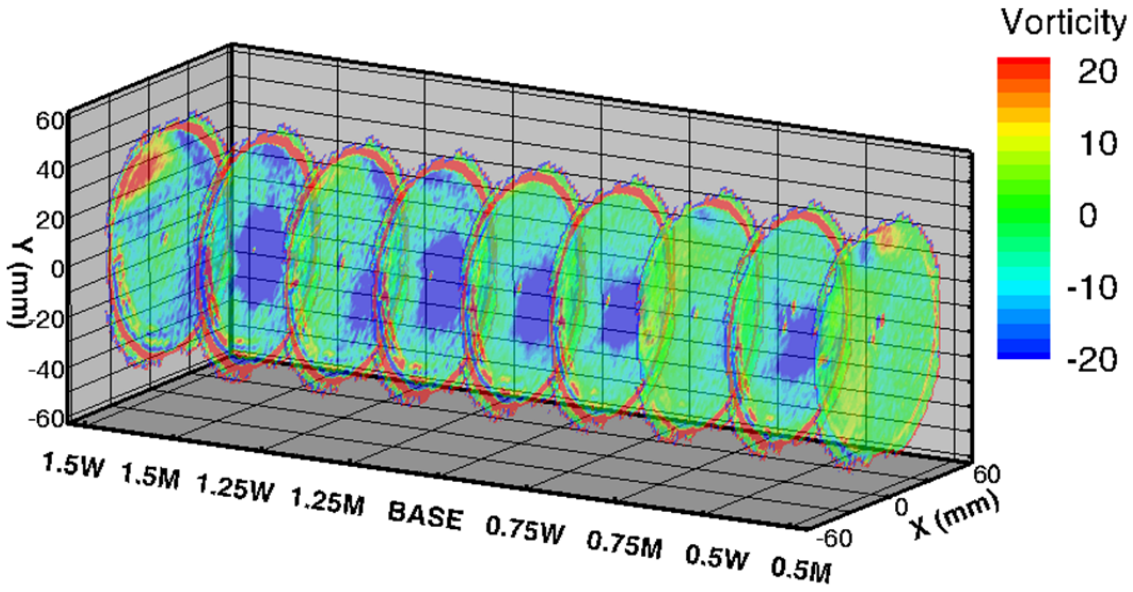

Figure 66 Vorticity contour at different flow rates

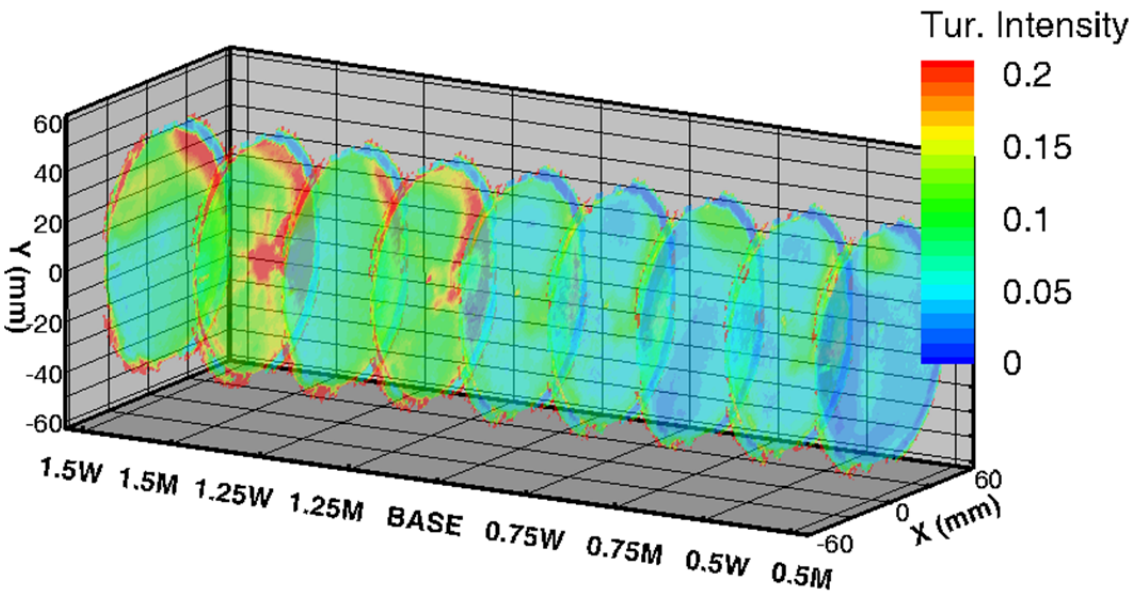

Figure 67 Turbulence intensity contour at different flow rates

4.1.8 PIV using carbon particles

In order to approach the real two phase flow condition in a solar reactor, the tracking particles are replaced by the 50 nm size SUPER-P carbon particles. The solid particles are extracted, dried and loaded into a pulsed vibrating solid injector located between the rotameters and the reactor model. The flow fields are captured from the entrance zone to the exit of the reactor as shown in Figure 68, Figure 69 and Figure 70. The non-uniform tracking particle distribution is captured at the entrance zone, and a self-homogenization process during spatial evolution is observed. The clockwise spiral path of the vortex core matches the result of the liquid particle experiment at same flow condition except the particle species used. Downstream of the cyclone, a helical vortex funnel is captured. The average flow speed considering the radius effect is 0.23 m/s compared to the result of 0.19 m/s obtained in the liquid particle measurement in the vacuum case at 1/3 atm. It's noticed that although the path of the vortex funnel in this case matches the result in the vacuum case, the vorticity contour in this case is more chaotic than the previous cases, and the turbulent intensity contour is higher than the previous cases because of the existence of local velocity gradient. The higher velocity gradient can be caused by the variations of the particle size, humidity, particle surface condition, centroid image correlation, static charge, scattering signal quality etc. However, apart from the local gradient, the measured flow speed and vortex evolution using solid carbon particles still proves that the previous cases using the TEG liquid particles are valid and can correctly predict the solid carbon particle trajectory and eliminate the local gradient effect.

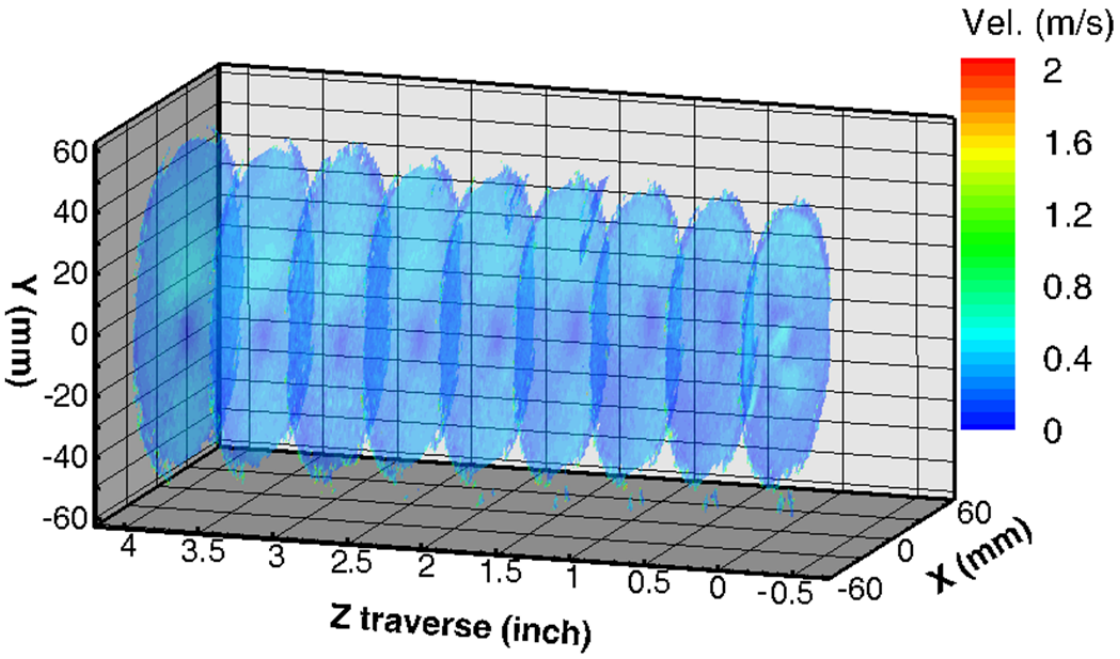

Figure 68 Velocity contour of 33 kPa absolute case with carbon particle

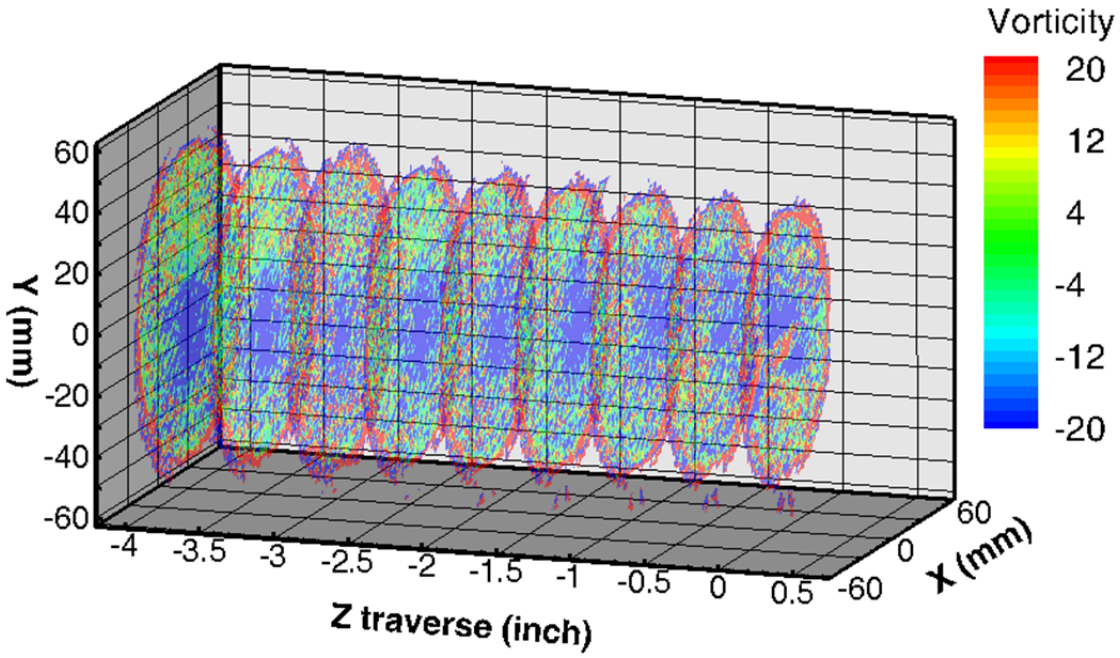

Figure 69 Vorticity contour of 33 kPa absolute case with carbon particle

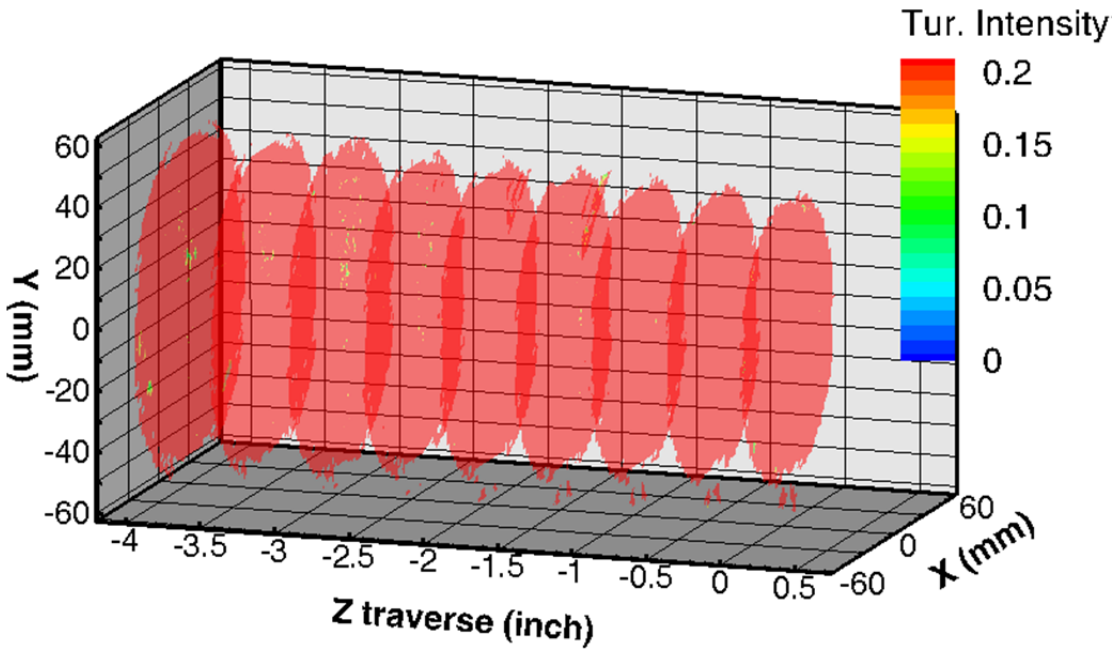

Figure 70 Turbulent intensity of 33 kPa absolute case with carbon particle

4.2 PIV uncertainty analysis

The propagation of uncertainty is the effect of variables' error on the uncertainty of a function based on them. For a typical digital PIV measurement, the source of uncertainty primarily comes from experimental setup, calibration, data acquisition and reduction. As is known, the uncertainty equation defined by Adrian (1986)

$$\frac{\sigma_u}{u_{\max}} = \frac{\sigma_x}{\Delta x_{\max}} = \frac{\sigma_X}{M \Delta x_{\max}}$$

The calibration induces uncertainty due to misalignment between the calibration plate and the image plane as shown in Figure 71. According to the uncertainty analysis by Nishio (2008), the reciprocal magnification factor α is defined as

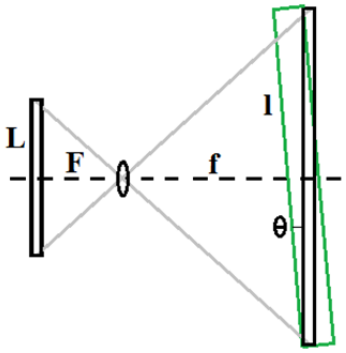

Figure 71 Parallelism deviation between light sheet and calibration plane

$$\alpha = \frac{f}{F} = \frac{l\cos\theta}{L} \approx \frac{l(1-\theta^2/2)}{L}$$

where L is the dimension of recording medium; l is the size of the light sheet; F is the distance between the image plane to the lens; f is the distance between the lens to the measuring volume. θ is a small angle misaligned between the light sheet and the calibration plane, The sensitivity factor regarding variable, for example α can be obtained by differentiate α with respect to the rest of variables individually. Table 9 shows the sources of uncertainty, bias limits to each of the sources and the corresponding sensitivity factors.

Category	#	Error sources (x_i)	Bias limit $u(x_i)$	Sensitivity factor (c_i)
Calibration board	1	Distance between reference dot images	0.707 pixel	$\partial\alpha / \partial L = l / L^2$ mm/pix^2
	2	Physical spacing of reference dots	0.02 mm	$\partial\alpha / \partial l = 1 / L$ 1/pix
Optical system	3	Image distortion due to lens aberration	0.005 L pixel	$\partial\alpha / \partial L = l / L^2$ mm/pix^2
	4	Image distortion due to CCD	0.0056 pixel	$\partial x / \partial X = \alpha$ mm/pix
Experiment setup	5	Calibration board positioning	0.5 mm	$\partial\alpha / \partial f = l / L / f$ 1/pix
	6	Parallelism of calibration board to light sheet	2°	$\partial\alpha / \partial\theta = l \cdot \theta / L$ mm/pix
Visualization	7	Lase power fluctuation	0.1 d_p *1.414 mm	$\partial X / \partial x = 1 / \alpha$ pix/mm
Image detection	4	Image distortion due to CCD	0.0056 pixel	1
	8	Viewing angle of camera	2°	$\partial\alpha / \partial\theta = l \cdot \theta / L$ mm/pix
Data processing	9	Miss-match error	0.1 pixel	1
	10	Sub-pixel error	0.03 pixel	1
Timing effect	11	Pulse delay fluctuation	2 ns	1
	12	Pulse timing error	5 ns	1
Experiment	13	Particle trajectory	0.01 % of U mm/s	1
	14	3-D effect	1 % of U mm/s	$u_m = u + w \cdot \tan\theta$
Positioning	15	Image centroid position	0.5 pixel	$\partial x / \partial X = \alpha$ mm/pix
	16	Non-uniform particle distribution	1/4 interrogation spot pixel	$\partial x / \partial X = \alpha$ mm/pix
	17	Origin correlation	2 pixel	$\partial x / \partial X = \alpha$ mm/pix
	18	Magnification factor	Sum of error 1-6	$\partial x / \partial\alpha = X$ pix

Table 9 Error sources of PIV

The total uncertainty on determining particle velocity can be expressed as

$$u_C = \sqrt{u_u^2 + (u_x \partial u / \partial x)^2 + (u_t \partial u / \partial t)^2}$$

Take atmospheric air case for example. The measuring conditions are listed in Table 10, the analysis are further divided into two orientations of capture. The first captures the axial velocity component of the vortex transversely from the side of the reactor (side view); the other captures the tangential velocity components through the reactor window in axial direction (top view).

Uncertainty analysis			
Orientation of measurement	SIDE	TOP	
Field of view	146	146	mm
Mean flow speed	0.51	0.51	m/s
Calibration			
Ref. physical plane size	90	91.42	mm
Ref. image plane size	1262	1281	pixel
Magnification Factor	0.071	0.071	mm/pix
Flow visualization			
Particle avg. diameter	0.001	0.001	mm
Std. deviation of diameter	0.0001	0.0001	
Particle avg. specific gravity	938	938	
Light sheet thickness	1	1	mm
Time interval	150	150	μs
Optical system			
Physical pixel size	7.4	7.4	μm
Distance from target to lens	508	508	mm
Focal length of lens	50	50	mm
F-number	8	8	
Perspective angle	<2°	<2°	
Data processing			
Recursive spot size	32	32	pixel

Table 10 PIV experimental setup

The detailed propagation of uncertainty is calculated in Table 11, Table 12, Table 13 and Table 14.

#	Bias limit u(xi)		Sensitivity factor ci		Uncertainty u(xi)*ci		combined u(xi)*ci	
1	0.707		5.65E-05	5.57E-05	4.00E-05	3.94E-05		
2	0.02		7.92E-04	7.81E-04	1.58E-05	1.56E-05		
3	6.31	6.41	5.65E-05	5.57E-05	3.57E-04	3.57E-04		
4	0.0056		5.65E-05	5.57E-05	3.16E-07	3.12E-07		
5	0.5		1.40E-04	1.40E-04	7.02E-05	7.02E-05		
6	0.035		0.002	0.0025	8.74E-05	8.74E-05	0.0004	0.0004
7	0.000141	0.000141	14.02	14.01	1.98E-03	1.98E-03		
4	0.0056		1	1	5.6E-03	5.6E-03		
8	0.035		0.0025	0.0025	8.74E-05	8.74E-05		
9	0.1		1	1	0.10	0.10		
0	0.03		1	1	0.03	0.03	0.105	0.105
11	2.00E-09		1	1	2.00E-09	2.00E-09		
12	5.00E-09		1	1	5.00E-09	5.00E-09	5.39E-09	5.39E-09
13	0.138	0.138	1	1	0.138	0.138		
14	65.96	0.733	1	1	65.96	0.733	65.96	0.75

Table 11 Bias limits and sensitivity factors of PIV

Velocity error sources	u(xi)		ci		u(xi)*ci		
Magnification factor α	0.0004	0.0004	7151	7146	2.69	2.69	mm/s
Image displacement ΔX	0.105	0.105	475	476	49.7	49.8	mm/s
Time interval Δt	5.39E-09	5.39E-09	1	1	5.39E-09	5.39E-09	mm/s
Experiment Δu	65.96	0.75	1	1	65.96	0.75	mm/s
					82.6	49.8	mm/s

Table 12 Uncertainty of velocity

Positioning error sources	u(xi)		ci		u(xi)*ci		
Image centroid position	0.5	0.5	0.071	0.071	0.036	0.036	mm
Non-uniform particle distribution	8.0	8.0	0.071	0.071	0.571	0.571	mm
Origin correlation	2.0	2.0	0.071	0.071	0.143	0.143	mm
Magnification factor	0.0004	0.0004	1024	1023	0.385	0.385	mm
					0.70	0.70	mm

Table 13 Uncertainty of displacement

Time interval error sources	u(xi)		ci		u(xi)*ci		
Pulse delay fluctuation	2.00E-09	2.00E-09	1	1	2.00E-09	2.00E-09	s
Pulse timing error	5.00E-09	5.00E-09	1	1	5.00E-09	5.00E-09	s
					5.39E-09	5.39E-09	s

Table 14 Uncertainty of time

Based on the above parametric analysis, the velocity uncertainty dominates the accuracy of the PIV measurement while the uncertainties in displacement and time are negligible. The velocity uncertainties are 16.20 % and 9.77 % for side and top views images respectively. The above results are based on the mean flow speed equal to 0.51 m/s in the atmospheric air case. In the vacuum air case, the mean flow speed decreases to 0.2 m/s, the corresponding uncertainty increases to 28.0 % and 24.8 % for the side and top view images respectively. It's seen that the uncertainty of the side view measurement is higher than the other. The primary error sources are the miss-match error and the 3-D effect. The miss-match error comes from the pairing loss during image processing and is prevalent in all PIV applications. In conventional digital PIV system the miss-match error is also the primary source of measurement uncertainty.

In a rotating flow, the 3-D effect as a result of out-of-plane motion is more dominant than the other. For example, in Figure 72, assuming the view of camera is in positive Z direction of traverse, when a perspective angle θ exists between the light sheet and the viewing direction of camera as shown on the right of the figure, an additional component R2 will be included in the image besides the R1' component. In a vortex flow, the moving direction of the tracking particles is nearly perpendicular to the light sheet plane

which has only a very small vector component in the light sheet plane. Therefore the projected velocity component R2 is relatively large compared to the in plane motion R1'.

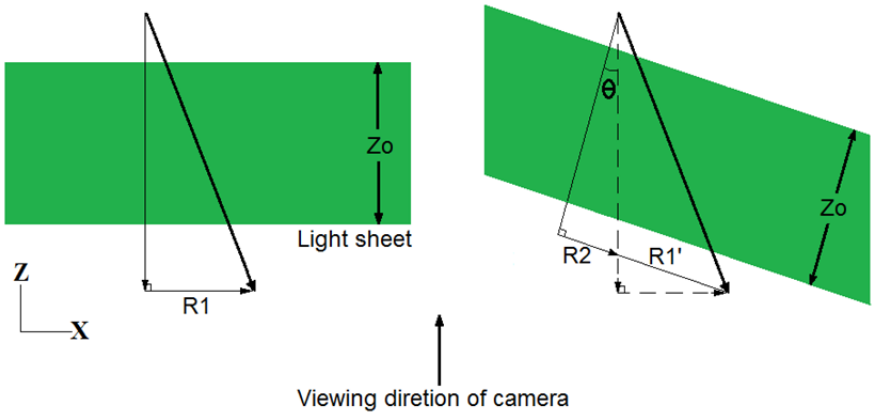

Figure 72 3-D effect on measuring a vortex flow by PIV

The remedy to reduce the measurement uncertainty under a fixed experimental setup can be done by either increasing the time interval or reducing the field of view by optical zoom-in while considering the robustness of the vector availability at high speed region.

When the time interval is increased, the uncertainty decreases when the particle displacement increases as shown in Figure 73. However, a larger time interval will increase the chance of losing particle image pairs in high speed region of the flow field, for example the vortex funnel of a cyclone flow where the flow rotates very fast compared to the periphery. On the other hand, decreasing the time interval will lead to an increasing uncertainty dominated by miss-match error. According to a system

parametric analysis, when the time interval is equal to 100 μs, the uncertainty due to miss-match error is equivalent to that of the 3-D effect. The uncertainty becomes miss-match error dominated when the time interval is less than 100 μs. In an optical analysis, the maximum time intervals to avoid in-plane and out-of-plane motions are 194 and 85 μs. In the experiment, an empirical value of time interval is set to 150 μs as a result of the above considerations.

The pressure effect to the measurement uncertainty is discussed. Figure 74 shows that the uncertainty decreases as the pressure increases. Essentially the operating pressure is proportional to the mean flow velocity. In Figure 74 the uncertainty is inversely proportional to the mean flow speed corresponding to different operating pressures. When the mean flow velocity is low, the 3-D effect becomes less significant compared to fixed miss-match error.

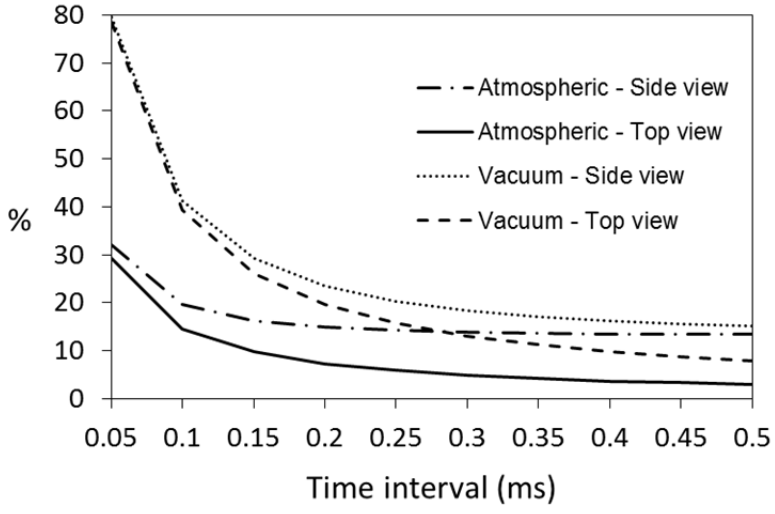

Figure 73 Time interval effect to uncertainties of atmospheric and 33 kPa vacuum cases

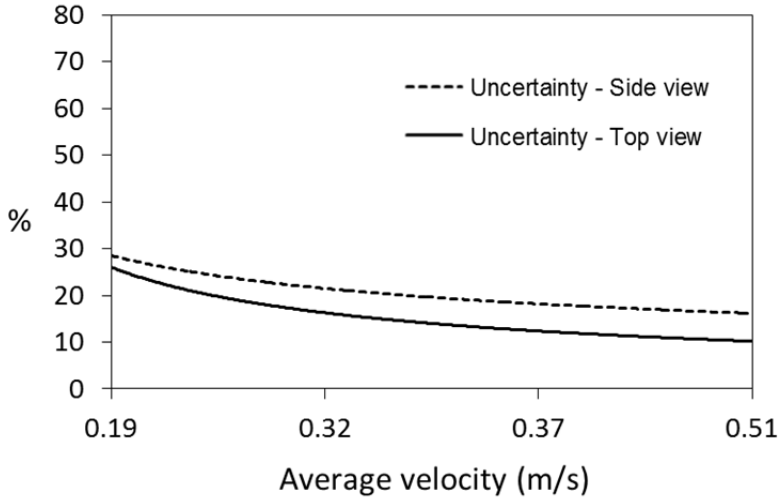

Figure 74 Mean flow speed effect to uncertainties of atmospheric and the vacuum cases

4.3 PSP measurement

4.3.1 PSP calibration

According to the principle of PSP method, one of the two gas species used in the measurement contains oxygen while the other doesn't. Therefore, the main flow and the window shield flow use air as the oxygen-containing gas; the wall shield flow uses carbon-dioxide as the oxygen-free gas since the molecular weight of carbon-dioxide is close to that of Argon in a real solar reactor. During the measurement, the volume flow rates are 10 LPM for the main flow, 10 LPM for the wall shield flow and 1 LPM for the window shield flow.

For calibrating the partial pressure of oxygen in terms of light intensity field, the main flow made of air and the wall shield flow made of carbon-dioxide are premixed with specific volumetric ratios before entering the reactor, while the window shield flow is turned off. Due to the use of compressed gas sources, long gas hoses are used to minimize the temperature variation with respect to the ambient temperature and to reach homogeneous concentration of oxygen in the reactor for calibration. The pressure variation can be ignored by maintaining the ambient static pressure within the open-end reactor. The light intensity fields at five different partial pressures of oxygen, as shown in Figure 75, are captured for used as a calibration series for interpolation. By taking 10

LPM wall shield flow rate as the base case, the percentage of oxygen in terms of the wall shield flow rate fraction, x, is shown in the following equation.

$$O_2\% = \frac{2.31}{11+10x} \times 100\%$$

In the PSP calibrations, the wall shield flow rate fraction x changes from 50 to 150 % with respect to the base case, the corresponding volumetric percentage range of oxygen in calibration is between 14.4% and 8.9 %.

Upon acquiring the calibration image series, a data reduction is performed via a binning process before further image processing. Since the variation between the intensity and the partial pressure of oxygen on each pixel is not linear, the calibration image series are processed via a self-developed MATLAB script to establish the calibration matrix. Noise filtering is done by subtracting the dark background from the calibration images. A quadratic polynomial curve-fit is applied to the calibration images series. The robustness of the obtained calibration matrix is inspected by observing the curve-fit deviation at nine selected points shown in Figure 76 (a). The maximum pressure deviation is 1.2 % at point 4 of the image. A relatively large noise at point 4 is expected since the region is severely affected by the non-uniform concentrated illumination due to the characteristic of the lamp bulb. The pressure field from measurement is obtained via data point interpolation. In Figure 76 (b), the results from an example measurement are marked as the red dots.

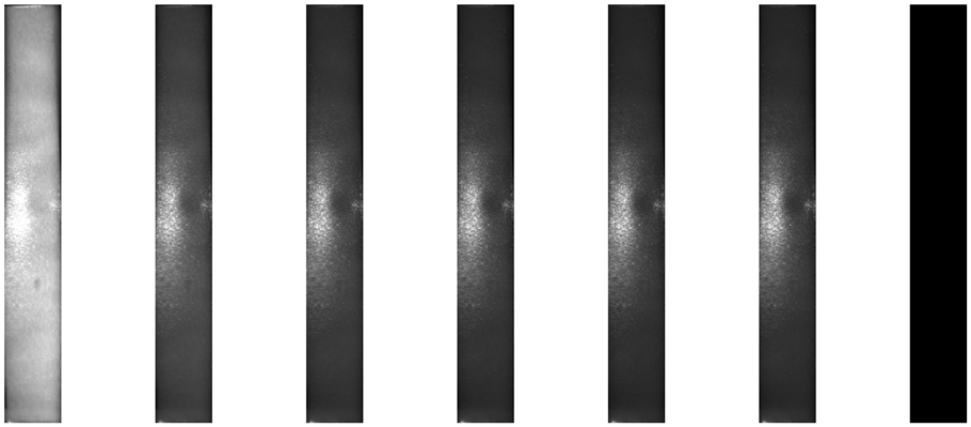

(a) (b) (c) (d) (e) (f) (g)

Figure 75 Calibration series of the wall shield flow (a) 150% (b) 125% (c) 100% (d) 75% (e) 50% (f) reference field (ambient air) (g) dark field (ambient air)

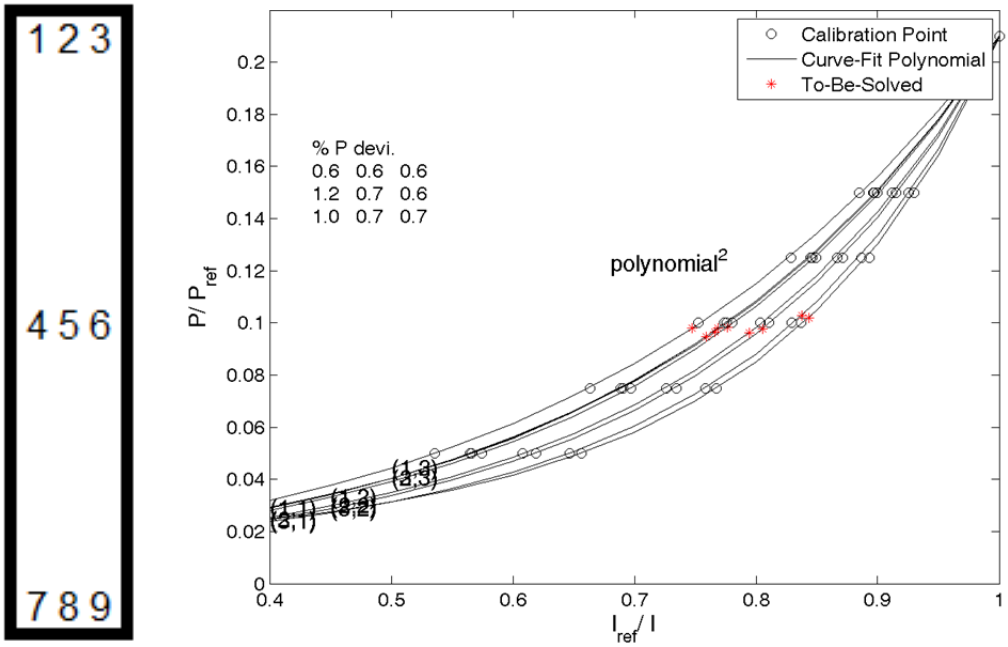

(a) (b)

Figure 76 9-points calibration (a) inspecting positions (b) curve-fit of the pressure ratio to the intensity ratio

4.3.2 PSP measurement result

The primitive result shows that the oxygen concentration variations is two-dimensional, therefore the paint area is expanded horizontally by adding another two paint unit. The measurement result is shown in Figure 77. The oxygen percentage contour resolution is less than 0.5 %. The oxygen percentage contours shows that except the bottom left area of the paint, the wall shield flow mix with the main flow and reach a uniform concentration quickly after being injected into the entrance zone. At the bottom left corner of the contours, higher oxygen concentrations are measured. According to the shape of the concentration spots and the circulating direction of the cyclone flow, it's found that the effectiveness of the wall shield flow is dominated by the upstream wall shield flow condition. For example, the thickness of the paint blocks the wall shield flow path when the wall shield flow is discharged via the 0.2 mm entrance slot, which leads to weaker protection downstream. Therefore the higher oxygen concentration spots are the result of the main flow impingement. The non-uniform distribution of the wall shield flow through the internal channel can also cause the higher oxygen concentration spot.

By comparing the contour at different wall shield flow rate, when the wall flow rate increases, the protection against the main flow impingement becomes stronger since the higher flow momentum can better prevent main flow impingement. Therefore, the wall shield flow is proved to be able to relieve the main flow contact on the inner wall.

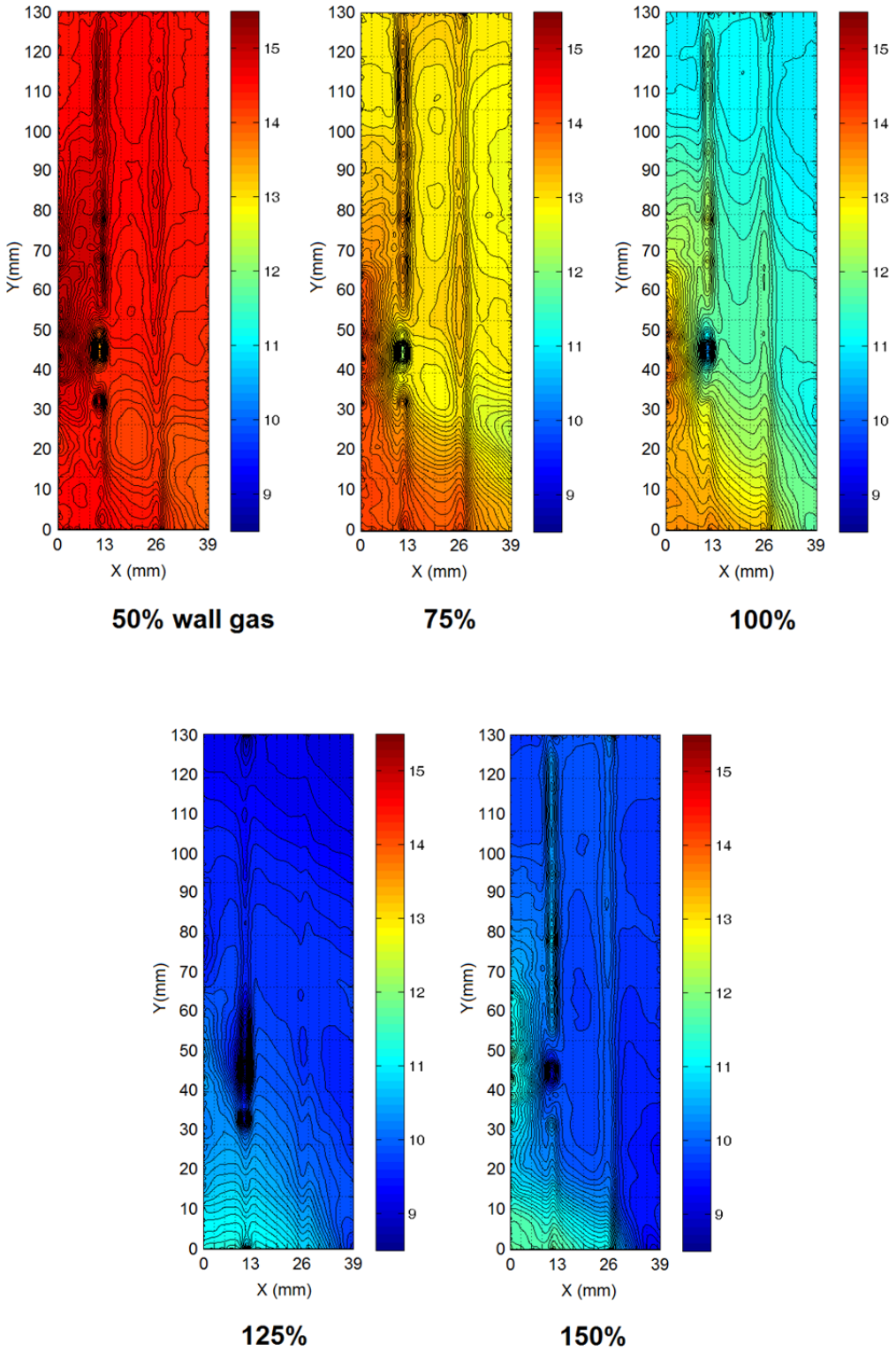

Figure 77 Volumetric oxygen percentage contours at different wall shield flow rates

4.4 PSP uncertainty analysis

Figure 25 shows the detailed position of the PSP paint on the inner wall of the reactor. Except the pressure and temperature included in the calibration formulation, the error sources of a conventional PSP measurement come from model displacement, paint thickness, optical distortion, illumination variation and chemical degradation.

Since the calibration is performed independently before each measurement, the influence of the model displacement, the paint thickness and the chemical degradation to the measuring error is removed. The thickness effect can be further reduced by a well-controlled painting process and image binning. Also the paint is located at middle of the far side of the inner wall when the view of camera sees through the center of reactor, the optical distortion is minimized before further spatial calibration. Therefore the temperature and illumination variations are the two major error sources.

In order to minimize the influence of the light distribution to the measurement, the calibration and measurement are conducted after 30 minutes of light source operation to ensure minimum light intensity variation. Furthermore, the calibration is established in order from the case of oxygen-free concentration to the case with ambient air content since the oxygen quenching response can be detected more quickly than the fluorescing process does. Also an experiment after a long warm-up time can reduce the temperature difference and fluctuation during both the calibration and the measurement.

4.5 CFD simulation result

4.5.1 Boundary condition

The boundary conditions of the room temperature cases are set to be the same as the flow conditions of the PIV measurement in the previous work, shown in Table 15 below. According to the setup of the 1/3 atm vacuum case measurement, the bulk density of the reactor fluid is 0.397 kg/m^3. In the simulation validation, the inlet pressure, temperature, velocity and outlet pressure are kept the same as the experimental setup. Both the mass flow rate and inlet velocity options are tested separately to exam the pressure field variation effect to the computational convergence according to the fixed outlet pressure setting. The turbulent intensity and hydraulic diameter are used as the boundary turbulent parameters. For the single reactor exit, pressure outlet with specified turbulent intensity and hydraulic diameter is used for better iterating convergence. In the particle tracking model, the carbon particles are released from the main flow inlet surface since the solid particles formed in the real solar reactor originate from the main flow fuel gas.

In the high temperature case, the operating temperature is set to 1500 ^{o}K where the gas compositions reach steady state provided enough residence time (Weimer 2000). The inlet and outlet boundary conditions are shown in Table 16. The ideal gas assumption is applied to all above cases since the gas compressibility effect can be neglected for low pressure or high temperature operating condition here.

B.C. Flows	Velocity inlet (m/s)	Mass inlet (kg/s)	Pressure inlet (kPa)	Pressure outlet (kPa)
Main	2.99	6.62E-5	33.51	33.51
Wall	8.13	6.62E-5	33.51	
Window	0.30	6.62E-6	33.51	

Table 15 Boundary conditions of vacuum case at room temperature

B.C. Flows	Velocity inlet (m/s)	Mass inlet (kg/s)	Pressure inlet (kPa)	Pressure outlet (kPa)
Main	2.99	3.92E-5	101.325	101.325
Wall	8.13	3.92E-5	101.325	
Window	0.30	3.92E-6	101.325	

Table 16 Boundary conditions of solar reactor at 1500 $^{\circ}$K

4.5.2 Heat transfer analysis

According to the simulation result by Hirsch and Steinfeld (2004b), the carbon particles as a product of the decomposition reaction affects the efficiency of the solar reactor in the form of interaction of radiation between the carbon particles and the reactant fluid. A higher carbon particle concentration leads to a larger optical thickness and thus a higher attenuation of radiation occurs. A large optical thickness is beneficial in absorbing the solar energy and reducing the temperatures of both reactant and the reactor wall.

In the PIV measurement, the average diameter of the carbon particles is 50 nm in average granular size to ensure the tracking accuracy, the corresponding marginal incident wavelength of Rayleigh scattering is 500 nm. Therefore the image signal of the seeding particles from a 532 nm laser light sheet is primarily Mie-scattering.

The absorption coefficient, a_λ, and scattering coefficient, σ_λ, can be calculated from the following equations, where N, f_v, d, $Q_{a\lambda}$, $Q_{s\lambda}$ are number of the particles per unit volume, volume fraction of the particles in the measuring space, particle diameter, absorption and scattering efficiency factors. An attenuation coefficient K_λ is defined as the sum of the two coefficients.

$$a_\lambda = \frac{\pi d^2}{4} Q_{a\lambda} N = \frac{3 f_v}{2d} Q_{a\lambda}$$

$$\sigma_\lambda = \frac{\pi d^2}{4} Q_{s\lambda} N = \frac{3 f_v}{2d} Q_{s\lambda}$$

$$K_\lambda = a_\lambda + \sigma_\lambda$$

The theoretical Mie-solution is obtained from the BHMIE code developed by Bohren and Huffman (1983) assuming homogeneous spheres to obtain the absorption and scattering efficiency factors as functions of the size parameter $\pi d / \lambda$ and the complex form of refractive index $n + i\kappa$ of the particle. The refractive index of carbon particle is approximated by the properties of acetylene soot shown in Figure 78 since acetylene was found the major intermediate product of the methane dissociation reaction in recent methane decomposition experiments. The above equations show that the common fraction term determines the scale of absorption and scattering while the efficiency factors determine the distribution from total attenuation.

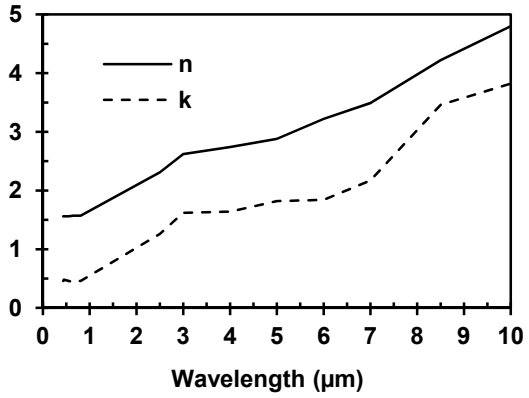

Figure 78 Refractive index of soot, extracted from Dalzell and Sarofim (1969)

The attenuation analysis in Figure 79 shows that the absorption and scattering coefficients of the tracking particles are higher in short wavelength range and decaying as wavelength increases in the Mie-scattering wavelength range. The scattering coefficient is relatively high at 532 nm wavelength of the PIV laser. For this size of the particles, the absorption dominates the radiative attenuation.

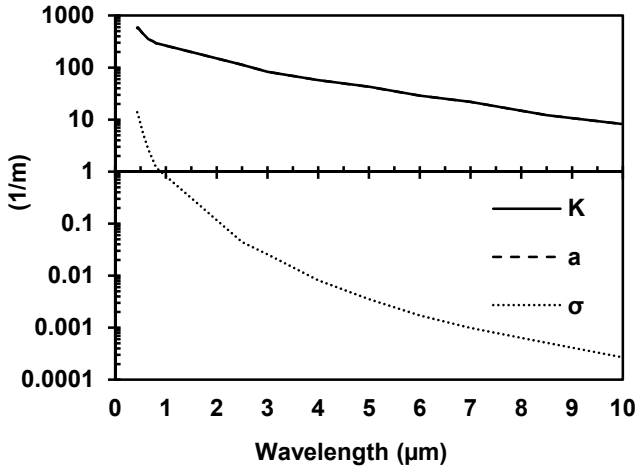

Figure 79 Attenuation, absorption and scattering coefficients of 50 nm carbon particles

In order to obtain the global absorption and scattering coefficients over the spectrum to simplify the problem, the Rayleigh scattering can be neglected when increasing the size of the carbon particle. The radiative properties for the particles of 1, 10 and 20 μm sizes are compared in Figure 80. A particle size larger than 1 μm gives lower but more constant radiative properties across the band. Also, the larger particles tend to have more scattering than absorption, while the particles smaller than 1 μm has higher absorption than scattering. Therefore, properties of 10 μm particles where the absorption and scattering parameters are nearly constant are chosen. Table 17 contains the parameters for the CFD simulation.

Parameter	**Value**
Particle mass flow rate (kg/s)	4.6×10^{-5}
Particle density (kg/m^3)	2000
Total fluid volumetric flow rate (LPM)	21
Particle diameter (m)	1×10^{-5}
Particle size parameter	26.51
Inlet temperature (K)	300
Viscosity (kg/m-s)	1×10^{-8}
Absorption coefficient of particle – a (1/m)	8
Scattering coefficient of particle– σ (1/m)	12
Radiation intensity (kW/m^2)	1361
Total solar power (kW)	6.8

Table 17 Radiative properties of carbon particles

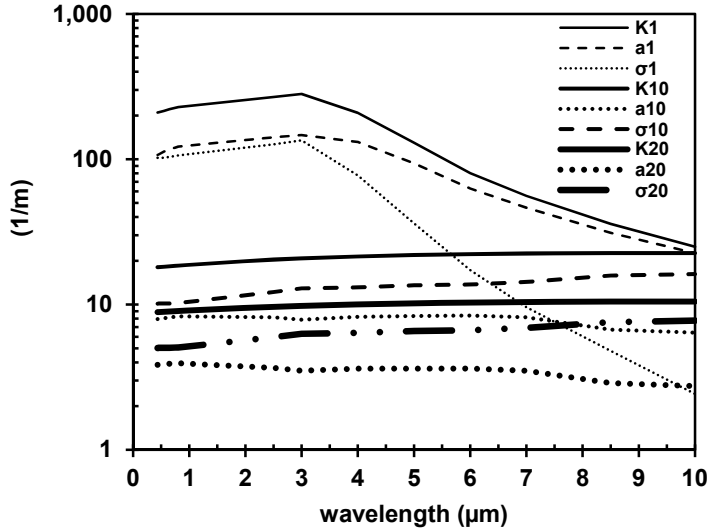

Figure 80 Attenuation, absorption and scattering coefficients of 1, 10 and 20 μm carbon particles

4.5.3 Fluid dynamics

When the operating pressure is at 1/3 atmosphere absolute pressure, where the gas density is kept same as the real solar reactor, the air flow is not uniformly distributed in the buffering channels before entering the reactor. Four of the radial jets carry more flow momentum than other jets and form a merged jet stream in the entrance zone. The merged jet stream impinges on the opposite side of the inner wall and moves downstream in clockwise direction along the wall surface. Due to the effect of this unbalanced jet impingement, the shape of the vortex line changes from an expected straight path to a helical path. The position of the vortex core tends to deviate from the geometric axis of the reactor and moves clockwise corresponding to the swirling motion

of the merged jet stream. For example, the vortex core deviates to above the geometry center at the beginning as shown in Figure 81.

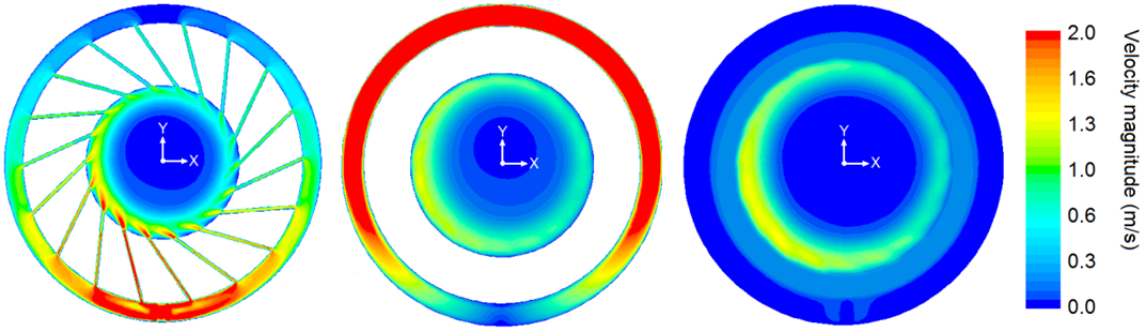

(a) (b) (c)

Figure 81 Fluid velocity contours in buffering channels of **(a)** main flow **(b)** wall shield flow **(c)** window shield flow at 300 $^{\circ}$K, 1/3 atm

In Figure 82 the cross section velocity contour of the reactor fluid show the overall fluid velocity magnitude is about 0.2 m/s, which predicted the PIV measurement of the vacuum case at 1/3 atm. In Figure 82 (a) the vortex core begins at a position deviated from the axis of the reactor in +Y coordinate and moves toward -Y coordinates downstream, and gradually move back to the center line of the reactor. In Figure 82 (b) the vortex core beginning at a -X position moves toward +X then move back to -X coordinates. The combined moving path of the vortex core from part (a) and (b) indicates a helical vortex line starting in the 2nd (-X, +Y) quadrant on the X-Y plane and move clockwise towards downstream to the exit of the reactor, which coincides with the PIV measurement result.

Figure 83 shows the spatial evolution of the vortex core at positions corresponding to the positions in the PIV measurement of the vacuum case. The CFD vortex core path successfully predicts the PIV measurement result. As the fluid moves to downstream, the fluid momentum becomes more uniformly distributed as a result of turbulence momentum transport and mixing. A significant difference of fluid velocity distribution between experiment and simulation in the entrance zone is observed. The turbulence models are less accurate while simulating the Rankine vortex flow rather than a cyclone separator flow, for example, the vortex funnel tends to be more radially expanded outward while the free vortex is suppressed compared with the experimental results due to cyclone separation.

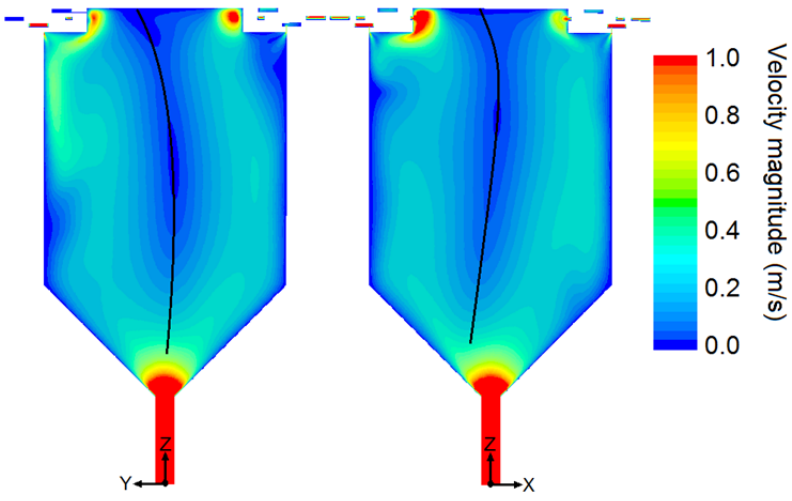

(a) (b)

Figure 82 Fluid velocity contours on (a) Y-Z (b) X-Z cross-section plane of the reactor at 300 °K, 1/3 atm

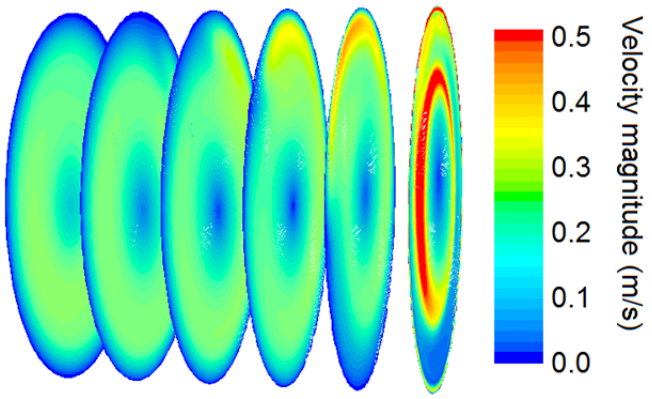

(f) (e) (d) (c) (b) (a)

Figure 83 Fluid velocity contours on cross-section planes of **(a)** z = 0 mm **(b)** z = 25.4 mm **(c)** z = 50.8 mm **(d)** z = 76.2 mm **(e)** z = 101.6 mm **(f)** z = 127 mm in the cylindrical zone of reactor at 300 $^{\circ}$K, 1/3 atm

In order to compare the temperature effect in the CFD simulation, two case simulations at 1500 $^{\circ}$K are performed. Figure 84 and Figure 85 show the case where the three flows operate at 1500 $^{\circ}$K. The inlet mass flow rates of the three flows are 40 % lower than those of the room temperature vacuum case in order to maintain the inlet velocities. Therefore the average velocity magnitude is about 20 % less than the room temperature case. It‘s seen that the spatial evolution of the helical vortex line is the same as that of the room temperature case. However, at the near wall region of the conical part, the fluid shows lower velocity magnitude than the room temperature case as an indication of dissipating fluid momentum.

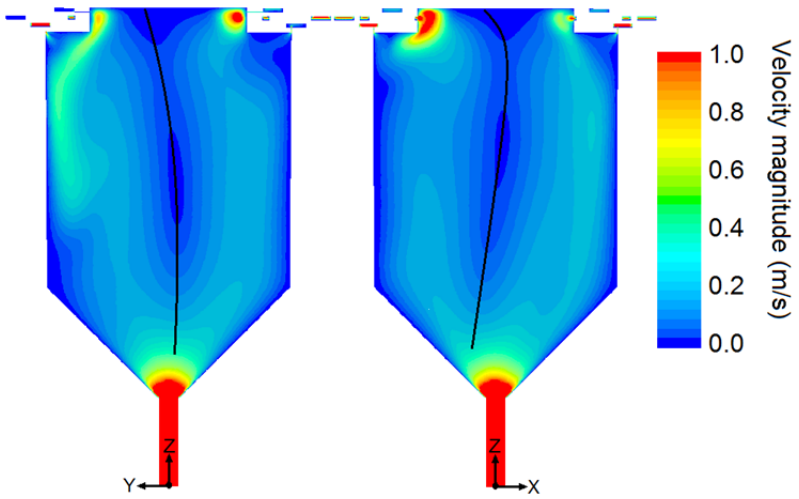

(a) (b)

Figure 84 Fluid velocity contours on **(a)** Y-Z **(b)** X-Z cross-section plane of the reactor at 1500 °K, 1 atm

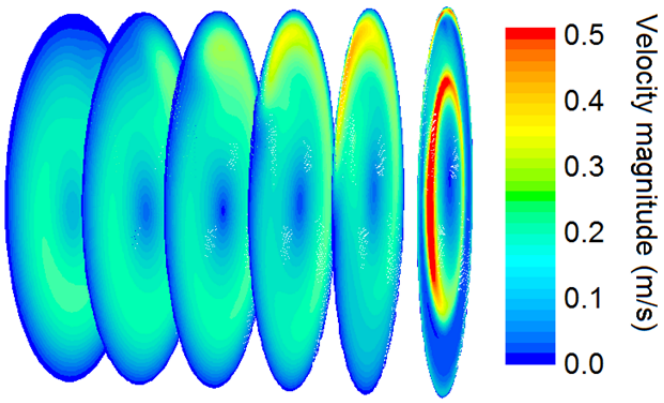

(f) (e) (d) (c) (b) (a)

Figure 85 Fluid velocity contours on cross-section planes of (a) z = 0 mm (b) z = 25.4 mm (c) z = 50.8 mm (d) z = 76.2 mm (e) z = 101.6 mm (f) z = 127 mm in the cylindrical zone of reactor at 1500 °K, 1 atm

The other case using 1500 °K main flow and 300 °K shield flows as boundary conditions is shown in Figure 86 and Figure 87. The mass flow rates of the wall shield flows are higher than the main flow and thus a more chaotic flow pattern is expected. The vortex structure is counteracted by the strong momentum of the shield flows. A strong wall shield flow close to the supply inlet extends further than the previous two cases as a direct result of increased mass rate. On the other hand, the wall shield flow on the opposite side of the supply inlet diminishes at near 1/4 length of the cylindrical part as a result of unbalanced fluid momentum distribution. It's seen that the wall shield flow becomes dominant and produces reversing flows between the middle and the top of the reactor.

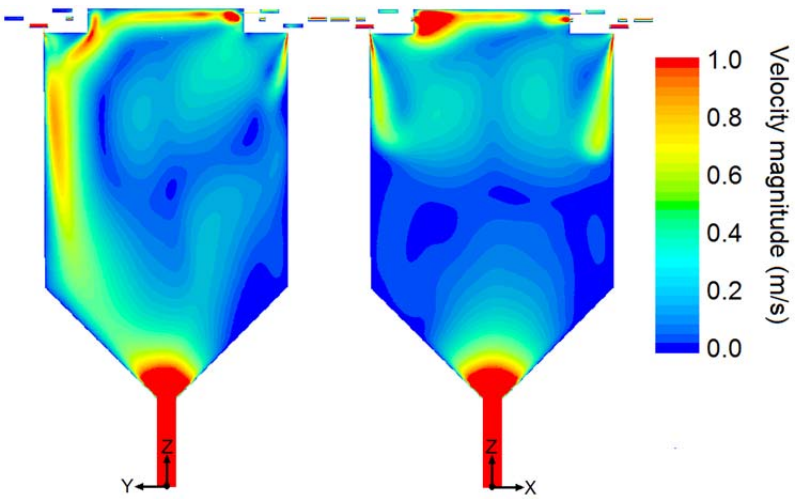

(a) (b)

Figure 86 Fluid velocity contours on (a) Y - Z (b) X - Z cross-section plane of the reactor at 1500 °K, 1 atm using 300 °K shielding flows at the inlets

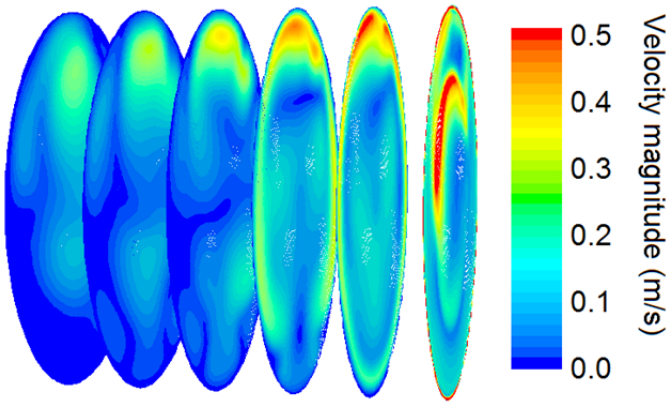

(f) (e) (d) (c) (b) (a)

Figure 87 Fluid velocity contours on cross-section planes of (a) z = 0 mm (b) z = 25.4 mm (c) z = 50.8 mm (d) z = 76.2 mm (e) z = 101.6 mm (f) z = 127 mm in the cylindrical zone of reactor at 1500 °K, 1 atm using 300 °K shielding flows at the inlets

When the DO radiation model and DPM model with 10 μm solid particles are applied to the simulation, the radiation energy heats the flow at the entrance zone up to above 1500 °K. The reactor wall is assumed to be thermal adiabatic. The average speed of the fluid is between 0.3 to 0.7 m/s shown in Figure 88 and Figure 89. The velocity of the fluid becomes more axis symmetric compared to the previous room temperature cases as a result of general increment of fluid speed by the irradiation heat. The momentum of the fluid is redistributed, smoothing the velocity shear by the increasing fluid speed. It's also seen that, except the entrance zone, where the fluid is not fully heated to a high temperature, the vortex line returns to nearly a straighter path compared to the helical path in previous cases due to the overall increase of fluid injection. The Reynolds number in the flow field is about 230, thus the inlet fluid is laminar.

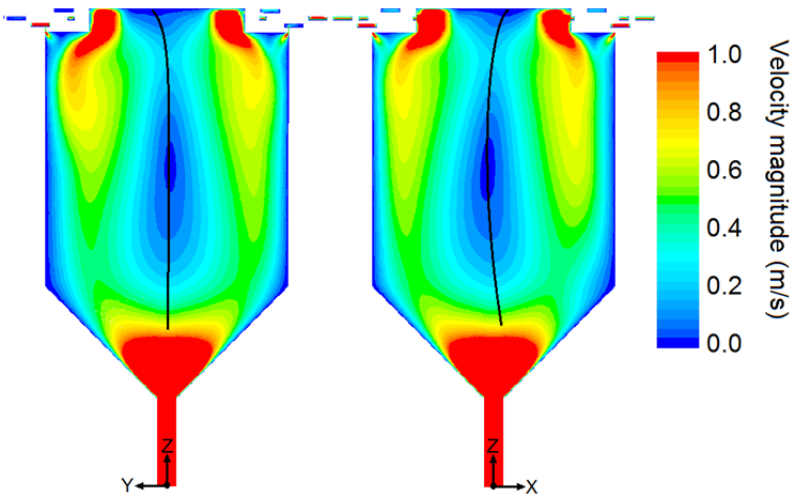

(a) (b)

Figure 88 Fluid velocity contours on **(a)** Y-Z **(b)** X-Z cross-sectional plane at 1 atm using 300 °K inlet gases heated by concentrated solar flux

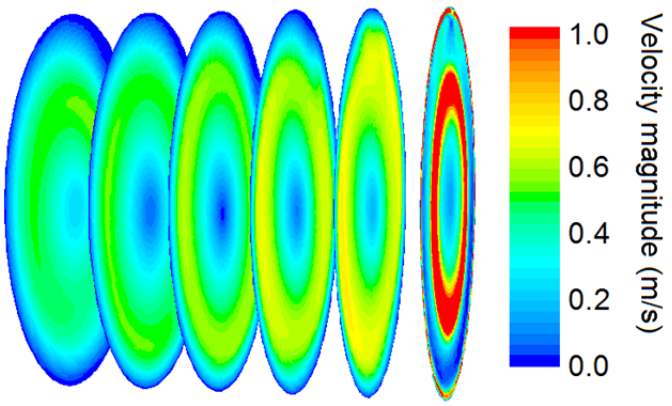

(f) (e) (d) (c) (b) (a)

Figure 89 Fluid velocity contours on cross-sectional planes of (a) z = 0 mm (b) z = 25.4 mm (c) z = 50.8 mm (d) z = 76.2 mm (e) z = 101.6 mm (f) z = 127 mm in the cylindrical zone of reactor at 1 atm using 300 °K inlet gases heated by concentrated solar flux

Figure 90 shows the static temperature distribution of the fluid. The main flow reaches 1200 °K before entering the entrance zone as a result of thermal conduction. The internal averaged temperature is 1800 °K under 1361 kW/m^2 direct solar heat flux through the diffusive reactor window. The total thermal energy input according to the solar flux is 6.8 kW. The temperature near the inner wall is higher than the fluid at center because of the strong irradiation absorption for solid wall than the semi-transparent fluid.

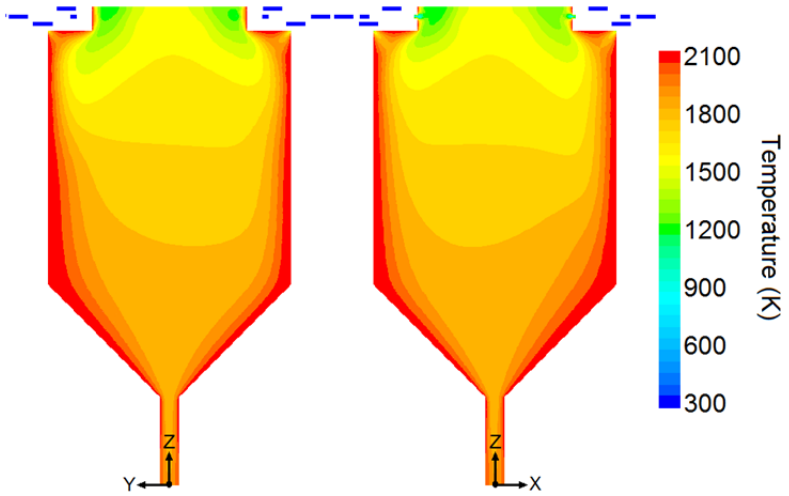

(a) (b)

Figure 90 Fluid temperature contours on **(a)** Y-Z **(b)** X-Z cross-sectional plane at 1 atm using 300 °K inlet gases heated by concentrated solar flux

Figure 91 shows the particle tracking of the Discrete Phase Model (DPM). The 10 μm solid particle enters the reactor via the channels of the main flow. Due to the radiation flux from above the reactor, the particles are heated near the end of the radial channels to around 1000 °K, and the density decreases drastically at the entrance zone then maintain

a constant value in the reactor except near the wall, where thermal radiation emission from the opaque reactor wall surface makes the additional increment of particle temperature. It's seen that the temperature near the center of the reactor is lower than that near the wall region due to solid surface emission.

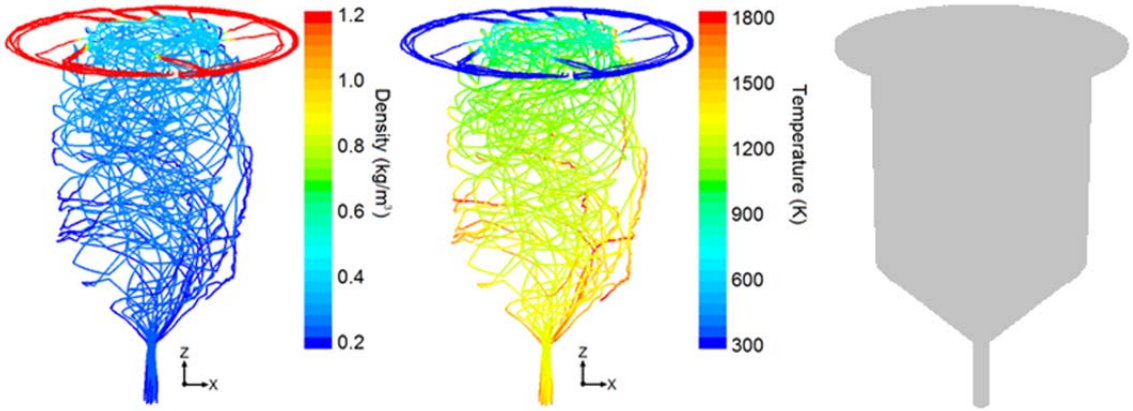

(a) (b) (c)

Figure 91 Particle tracking trajectory by DPM model in contour of **(a)** density **(b)** temperature **(c)** fluid domain geometry

In the simulation it's also observed that when the mass flow rates increase, the non-uniform momentum distribution is reduced because the inner channels are filled with adequate mass with enough momentum to propagate further and thus creates a more uniform distribution of flow in the inner channels.

The three dimensional geometry CFD model with fine mesh grids on the inner wall, center and internal channels is able to simulate the flow pattern of the air cyclone in a

solar reactor. A room temperature case using air as the dummy fluid is validated by the PIV measurements under same known boundary conditions. The patterns of the vortex core are the same between the CFD simulation and the PIV experiment. Compared to the high temperature case, the flow field in the room temperature case is proved to be not axial-symmetric due to the insufficient momentum level in the reactor. This drawback is counteracted by increasing the fluid temperature via solar radiation energy into the reactor. The vortex line returns to nearly a straight line as the fluid momentum increases by heating. In the high temperature cases, the shield flows seems to be not effective enough to extend to the downstream of the reactor to protect the reactor wall from particle deposition. This drawback can be compensated for by either inject more fluid as shown in the high temperature case with more mass flow rate for the screening flows or replace the flow species of the original flow to heavier gas species, for example, argon to achieve the purpose. A careful redesign at the shield flow entrance is also necessary to prevent separation.

By comparing the previous cases, the CFD model is less accurate in predicting the location of the peak tangential velocity than the vortex flow core and the mean velocity magnitude of a cyclone structure in the reactor. However, in Figure 89 the Rankine vortex is recovered better than the previous CFD case, although the force vortex is still over expanded. In general, the hexahedral mesh CFD model is capable of simulating a cyclone structure in a solar reactor at high temperatures up to 1500 $^{\circ}$K, although the free

vortex is not significant due to the limitation of the CFD modeling with limited boundary conditions.

The methodology and result in this CFD analysis are proved to be a useful guideline to predict the flow dynamics in cyclone flow structure in regions where PIV cannot reach in a real solar reactor due to either the temperature or physical barriers.

5 SUMMARY AND CONCLUSIONS

A step-by-step study of fluid dynamics of the solar cyclone reactor is demonstrated. Both experimental and numerical methods are used to investigate the details of the fluid interaction. The results from the two approaches are verified by one another under the same setup condition at room temperature. A high temperature simulation is performed to further explore the in-sight of a real solar reactor. Both fluid dynamics and heat transfer are considered in the high temperature case. A physical explanation from the thermodynamic and heat transfer point of view is given.

5.1 Summary

1. A thermodynamics parametric study to a reference CFD design of a high temperature solar cyclone reactor with auxiliary flows was analyzed. The temperature profile decays from the highest temperature near the flow entrance toward the outlet. The average fluid temperature is 837 $^{\circ}$K at atmospheric pressure. The averaged Reynolds number is 545.

2. A transparent solar reactor model as well as the real-time flow monitoring and control system for optical measurement was designed, manufactured, assembled, calibrated and tested. The inlet flow rates were calculated according to the ideal gas law. The controlled pressure accuracy is up to 0.01 kPa. The temperature variation is less than 0.2 $^{\circ}$K.

3. A 3-D light tracing simulation was performed according to the geometry of the reactor. The path of the light sheet through the cylindrical part and the conical part of the reactor model were determined. The interval of the light sheets between each traverse position was maintained before and after the light deflection.

4. An optimal optical setting to the PIV system was analyzed. The dynamic velocity range (DVR) is 34; the dynamic spatial range (DSR) is 330 at f-number equal to 8. The optimal DVR is 36; the optimal DSR is 256 at f-number equal to 10. The image size is 1.84 pixels. The PIV system is diffraction limit dominated.

5. An Ekman layer analysis was performed. The Ekman number is to the power of 10^{-5}. The Ekman layer thickness is less than 10^{-3} mm. A Coriolis Effect enhanced secondary flow was induced and experimentally observed.

6. A PIV experiment was designed, assembled, calibrated and performed to acquire the internal fluid dynamics at different operating conditions. A stereo flow field was reconstructed. A Rankine vortex profile was observed. The mean flow velocities were 0.51 m/s in the atmospheric case and 0.19 m/s in the 33 kPa vacuum case. The Reynolds number of the vacuum case is 544, same as the thermodynamic analysis result. The reversed secondary flow around the vortex funnel was captured and quantified.

7. A residence time evaluation was performed according to the PIV result. A reduction of main flow to 82 % of the reference CFD setting causes the highest flow rate ratio between the swirl flow and the axial flow. The effect of changing flow rates was discussed.

8. The uncertainty analysis to the PIV system was evaluated. The bias limits and sensitivity factors according to the experimental setup were determined. The maximum uncertainty is 16.2 % from the side view and 9.77 from the top view in the atmospheric case; 28 % and 24.8 % respectively in the vacuum case.

9. A particle tracking analysis to the fidelity of the two particles species applied in the PIV measurement was performed. The liquid tri-ethylene glycol particle is 1 μm; the solid carbon particles are 50 nm. The two particle species adopted in the PIV measurement ensure over 99 % magnitude response with the cut-off frequency response above 46 kHz. The stagnation circulation of the carbon particles during steady state PIV measurement was observed.

10. An interrogation spot size effect to the signal strength attenuation was simulated using a synthetic flow field. The three times signal degradation by half the interrogation spot size was observed. The influence of the flow condition to the correlation signal strength was described.

11. A PSP measurement was performed to obtain the scale of the flow mixing on the wall region. An early separation and mixing between the main flow and the wall shield flow was identified. A jet impingement phenomenon was found on the inner wall near the entrance zone. A tendency of increasing wall shield flow rate to protect the inner wall from the main flow was observed. The experiment result coincides with the CFD simulation result.

12. A CFD simulation was performed according to the room temperature experiments. The path of the vortex core was identical to the measurement in the PIV experiment. A high temperature simulation using real solar reactor inlet conditions was performed. The thermal and radiation property of the particle, fluid and reactor wall were calculated. The result showed that the reaction has highest temperature on the inner wall.

5.2 Conclusion

The fluid dynamics and heat transfer in a solar cyclone reactor were experimentally and numerically analyzed. A transparent room temperature reactor model was designed and manufactured. A multi-task flow control and measurement platform was designed and calibrated. The light sheet reflection and refraction were controlled by utilization of light absorption materials and ray tracing analysis respectively. The reliability and robustness of the experimental facility configuration was validated through thermodynamic and optical parametric analysis. The space and time resolution of the measurement was

optimized for the measuring subject. The whole turbulent flow 3-D structure was reconstructed via particle imaging velocimetry (PIV) and pressure sensitive paint (PSP) techniques.

The flow parameters that affect the flow dynamics and performance of a solar reactor were investigated. When the main flow is increased to above 50 % with respect to the reference CFD case, the axial velocity of the fluid becomes proportional to the main flow rate, while the tangential velocity of the fluid is always proportional to the main flow rate. An increased main flow rate will enhance both swirling and axial fluid transports in the vortex funnel, which leads to a strong cyclone structure and reversing secondary flow. The swirl number increases to two times of the base case as the main flow rate reach 150 %. On the contrary, an increased wall shield flow will increase the instability of the vortex structure.

The optimal operating point of the flow inlet condition to achieve maximum residence time of fluid was obtained. The result shows that the optimal main flow rate deviated from the reference CFD case by 18 % lower. The swirl number was larger than 0.5 and required RSM model to account for the physics of free vortex.

A comparison of particle-fluid dynamics between using liquid TEG particles and the solid carbon particle was presented. The tracking capability of both particles was analyzed. The reliability of using 1 μm liquid particle to perform PIV measurement was

validated. A higher vorticity and turbulent intensity was observed in the carbon particle-fluid due to more irregular shape and size for solid type particles. The Stokes number is 6.5×10^{-3} for liquid particles and 3×10^{-4} for carbon particles via the Stokes flow analysis.

A CFD modeling and simulation were presented. The numerical model was validated by the experimental data. A 1500 °K flow dynamics simulation was conducted using air and reactor fluids respectively. The discrete ordinate (DO) model was used as the radiation model; the discrete phase model (DPM) was used as the particle tracking model.

The CFD result showed that the fluid was heated by the insulated reactor wall instead of by the solid carbon particles. However, by increasing the particle density the fluid temperature near the wall became lower and overall fluid temperature became more uniform as a result of irradiation shadowing.

REFERENCES

Abanades, A., Rubbia, C., Salmieri, D. 2012, "Technological Challenges for Industrial Development of Hydrogen Based Methane Cracking," *Energy*, 46(1): 359-363

Adrian, R. J., Christensen, K. T., Liu, Z. C. 2000, "Analysis and Interpretation of Instantaneous Turbulent Velocity Fields" *Experiments in Fluids*, 29(3): 275-290 DOI: 10.1007/s003489900087

Adrian, R. J. 1997, "Dynamic Ranges of Velocity and Spatial Resolution of Particle Image Velocimetry," *Measurement Science and Technology*, 8: 1393-1398 DOI: 10.1088/0957-0233/8/12/003

Adrian, R. J. 1991, "Particle Imaging Techniques for Experimental Fluid Mechanics" *Annual Review of Fluid Mechanics*, 23: 261-304 DOI: 10.1146/annurev.fl.23.010191. 001401

Adrian, R.J. 1986. "Multi-point Optical Measurements of Simultaneous Vectors in Unsteady flow – a review." *International Journal of Heat and Fluid Flow*, 7(2): 127-145

Adrian, R.J. 1984. "Scattering Particle Characteristics and Their Effect on Pulsed Laser Measurements of Fluid flow: Speckle Velocimetry vs. Particle Image Velocimetry" *Applied Optics*, 23(11): 1690-1691 DOI: 10.1364/AO.23.001690

Bohren, C. F., Huffman, D. R., 1983, "Absorption and Scattering of Light by Small Particles," *John Wiley & Sons*, New York, 1983, DOI: 10.1002/9783527618156

Chen, H., Chen, Y. Hsieh, H. T., Siegel, N. P., 2007, "Computational Fluid Dynamics Modeling of Gas-particle Flow within a Solid-particle Solar Receiver," *ASME Journal of Solar Energy Engineering*, 129(2): 160-170 DOI: 10.1115/1.2716418

Cheng L., Spencer, A., 2012, "Residence Time Measurement of an Isothermal Combustor Flow Field," *Experiments in Fluids*, 52: 647-661 DOI: 10.1007/s00348-011-1085-3

Cortes C., Gil A., 2007, "Modeling the Gas and Particle Flow Inside Cyclone Separators," *Progress in Energy and Combustion Science*, 33: 409-452 DOI: 10.1016/j.pecs.2007.02.001

Dalzell, W. H., Sarofim A. F., 1969, "Optical Constants of Soot and Their Application to Heat Flux Calculations," *Journal of Heat Transfer*, 91: 100-104 DOI: 10.1115/1.3580063

Daw, J. E., Rempe, J. L., Knudson, D. L., 2010, "Thermal Properties of Structural Materials Used in LWR Vessels," *Journal of Nuclear Materials*, 401(1-3): 65-70

Grant, I. 1997, "Particle Image Velocimetry: A Review," *Proceedings of the Institution of Mechanical Engineers, Part C: Journal of Mechanical Engineering Science*, 211: 55-76. DOI: 10.1243/0.54406971521665

Han, J. C., Rallabandi, A.P., 2010, "Turbine Blade Film Cooling Using PSP Technique," *Frontiers in Heat and Mass Transfer*, 1: 013001 DOI: 10.5098/hmt.v1.1.3001

Hart, D. P., 2000, "PIV Error Correction," *Experiments in Fluids*, 29: 13-22 DOI: 10.1007-s003480050421

Hirsch, D., Steinfeld, A., 2004a, "Solar Hydrogen Production by Thermal Decomposition of Natural Gas Using a Vortex-flow Reactor," *International Journal of Hydrogen Energy*, 29: 47-55 DOI: 10.1016/S0360-3199(03)00048-X

Hirsch, D., Steinfeld, A., 2004b, "Radiative transfer in a solar chemical reactor for the co-production of hydrogen and carbon by thermal decomposition of methane," *Chemical Engineering Science*, 59: 5771-5778 DOI:10.1016/j.ces.2004.06.022

Keane, R. D., Adrian, R. J., 1992, "Theory of Cross-correlation Analysis of PIV Images," *Applied Scientific Research*, 49(3): 191-215

Keane, R. D., Adrian, R. J., 1990, "Optimization of Particle Image Velocimeters: I Double Pulsed Systems," *Measurement Science and Technology*, 1:1202-1215 DOI: 10.1088/0957-0233/1/11/013

Keane, R. D., Adrian, R. J., 1991, "Optimization of Particle Image Velocimeters: II Multiple Pulsed Systems," *Measurement Science and Technology*, 2: 963-974. DOI: 10.1088/0957-0233/2/10/013

Kogan, A., Israeli, M., Alcobi, E. 2007, "Production of Hydrogen and Carbon by Solar Thermal Methane Splitting IV Preliminary Simulation of a Confined Tornado Flow Configuration by Computational Fluid Dynamics," *International Journal of Hydrogen Energy*, 32(18): 4800-4810 DOI: 10.1016/j.ijhydene.2007.08.016

Kogan, A., Kogan, M., Barak, S., 2004, "Production of Hydrogen and Carbon by Solar Thermal Methane Splitting II Room Temperature Simulation Tests of Seeded Solar

Reactor," *International Journal of Hydrogen Energy*, 29(12): 1227-1236 DOI: 10.1016/j.ijhydene.2003.12.002

Kogan, A., Kogan, M., 2002, "The Tornado Flow Configuration - An Effective Method for Screening of a Solar Reactor Window," *ASME Journal of Solar Energy Engineering,* 124(3): 206-214 DOI: 10.1115/1.1487882

Krishna, D.J., Ozalp, N., 2013. "Numerical Investigation of Particle Deposition Inside Aero-shielded Solar Cyclone Reactor: A Promising Solution for Reactor Clogging." *International Journal of Heat and Fluid Flow*, 40:198-209 DOI: 10.1016/j.ijheatfluidflow.2012.12.004

Liu, T., Guille, M. & Sullivan, J.P., 2001, "Accuracy of Pressure Sensitive Paint," *AIAA Journal*, 39(1): 103-112 DOI: 10.2514/2.1276

Martinelli, F., Cozzi, F., Coghe, A. 2012, "Phase-Locked Analysis of Velocity Fluctuations in a Turbulent Free Swirling Jet after Vortex Breakdown," *Experiments in Fluids*, 53(2): 437-449 DOI: 1.1007/s00348-012-1296-2.

McLachlan, B.G., Bell, J.H., 1995. "Pressure-Sensitive Paint in Aerodynamic Testing," *Experimental Thermal and Fluid Science*, 10(4): 470-485 DOI: 10.1016/0894-1777(94)00123-P

Mei, R., 1996, "Velocity Fidelity of Flow Tracer Particles," *Experiments in Fluids*, 22: 1-13

Melling, A., 1997, "Tracer Particles and Seeding for Particle Image Velocimetry," *Measurement Science and Technology*, 8:1406-1416 DOI: 10.1088/0957-0233/8/12/005

Morris, M.J., Donovan, J.F., Kegelman, J.T., Schwab, D.D., Levy, R.L. 1993, "Aerodynamic Applications of Pressure Sensitive Paint," *AIAA Journal*, 31(3): 419-425 DOI: 10.2514/3.11346

Muradov, N., Chen, Z., Smith, F., 2005, "Fossil Hydrogen with Reduced CO2 Emission: Modeling Thermocatalytic Decomposition of Methane in a Fluidized Bed of Carbon Particles," *Internaitonal Journal of Hydrogen Energy*, 30(10): 1149-1158. DOI: 10.1016/j.ijhydene.2005.04.005

Muradov, N., Smith, F., T-Raissi, A., 2005, "Catalytic Activity of Carbons for Methane Decomposition Reaction," *Catalysis Today*, 102-103: 225-233 DOI: 10.1016/j.cattod.2005.02.018

Natarajan, D., 2011, "Numerical Simulation of Tornado-like Vortices," *Ph.D. Dissertation*, The University of Western Ontario, Ontario, Canada

Nishio, S. 2008, "Uncertainty Analysis – an Example for PIV measurement," *Proceedings of 25th International Towing Tank Conference*, 2: 453-455

Ozalp, N., Chien, M. H., Morrison, G., 2013, "Computational Fluid Dynamics and Particle Image Velocimetry Characterization of a Solar Cyclone Reactor," *ASME Journal of Solar Energy Engineering*, 135(3): 031003/1-15 DOI: 10.1115/1.4023183

Ozalp, N., Chien, M. H., Morrison, G.L., 2012, "Experimental Evaluation of a Solar Cyclone Reactor via Particle Image Velocimetry," *Proceedings of the ASME 2012 Heat Transfer Conference*, July 8-12, 2012, Rio Grande, Puerto Rico, USA. HT2012-58149: 97-110 DOI: 10.1115/HT2012-58149

Ozalp, N, Devanuri, J., 2010, "CFD Analysis on the Influence of Helical Carving in a Vortex Flow Solar Reactor," *International Journal of Hydrogen Energy*, 35(12): 6248-6260

Ozalp, N., Kogan, A., Epstein, M., 2009, "Solar decomposition of fossil fuels as an option for sustainability," International Journal of Hydrogen Energy, 34(2): 710-720. DOI: 10.1016/j.ijhydene.2008.1.019

Philip, J., Hutchins, N., Monty, J.P., Marusic, I., 2013, "Spatial Averaging of Velocity Measurements in Wall-bounded Turbulence: Single Hot-wires," *Measurement Science and Technology*, 24(11): 115301 DOI: 10.1088/0957-0233/24/11/115301

Prasad, A. K., Adrian, R. J., Landreth, C. C., Offutt, P. W., 1992, "Effect of Resolution on the Speed and Accuracy of Particle Image Velocimetry Interrogation," *Experiments in Fluids*, 13(2-3): 105-116 DOI: 10.1007/BF00218156

Rodat, S., Abanades, S., Flamant, G. 2010, "Experimental Evaluation of Indirect Heating Tubular Reactors for Solar Methane Pyrolysis," *International Journal of Chemical Reactor Engineering*, 8: 1543-6580 DOI: 10.2202/1542-6580.2084

Rodat, S., Abanades, S., Sans, J. L., Flamant, G. 2010, "A pilot-scale Solar Reactor for the Production of Hydrogen and Carbon Black from Methane Splitting," *International Journal of Hydrogen Energy*, 35(15): 7748-7758 DOI: 10.1016/j.ijhydene.2010.05.057

Saikrishnan, N., Marusic, I., Longmire, E.K., 2006, "Assessment of dual plane PIV measurements in wall turbulence using DNS data," *Experiments in Fluids*, 41: 265-278 DOI: 10.1007/s00348-006-0168-z

Shilapuram, V., Devanuri, J. K., Ozalp, N., 2011, "Residence Time Distribution and Flow Field Study of Aero-shielded Solar Cyclone Reactor for Emission-free Generation of Hydrogen," *International Journal of Hydrogen Energy*, 36(21): 13488-13500

Steinfeld A., Brack, M., Meier, A., Weidenkaff, A., Wuillemin, D., 1998, "A Solar Chemical Reactor for Co-production of Zinc and synthesis gas," *Energy*, 23(10): 803-814 DOI: 10.1016/s0360-5442(98)00026-7

Szekely, J., Carr, R., 1966. "Heat Transfer in a Cyclone," *Chemical Engineering Science*, 21(12): 1119-1132 DOI: 10.1016/0009-2509(66)8533-9

Weimer A.W., Dahl, J., Tamburini, J., 2000, "Thermal Dissociation of Methane Using a Solar Coupled Aerosol Flow Reactor," *Proceedings of 2000 DOE Hydrogen Program Review*. NREL/CP-570-28890

Westerweel, J., 2000, "Theoretical Analysis of the Measurement Precision in Particle Image Velocimetry," *Experiment in Fluids*, 29: S003-S012 DOI: 10.1007/s003480070002

Westerweel, J., 1993, "Digital Particle Image Velocimetry: Theory and Application," *Ph.D. Dissertation*, Delft University, Delft, Netherlands

Willert, C.E., Charib, M., 1991, "Digital Particle Image Velocimetry," Experiments in Fluids, 10(4): 181-193 DOI: 10.1007/BF00190388

Wu, Z., Caliot, C., Flamant, G., Wang, Z., 2011, "Coupled Radiation and Flow Modeling in ceramic foam volumetric solar air receivers," *Solar Energy*, 85(9): 2374-2385

Yakhot, V., Orszag, S. A., 1986, "Renormalization Group Analysis of Turbulence I. Basic Theory", *Journal of Scientific Computing*, 1: 3-51

Zhang, W., Sarkar, P. P., 2012, "Near-ground Tornado-like Vortex Structure Resolved by Particle Image Velocimetry (PIV)", *Experiments in Fluids*, 52(2): 479-493 DOI: 10.1007/s00348-011-1229-5

APPENDIX A

A. Synthetic data simulation

A.1.1 Overview

The primary uncertainty source of conventional PIV techniques comes from the miss-match of image pairs. Disregarding the out-of-plane loss, this error appearing in image processing will not only reduce the signal peak strength but also contribute to the background noise. In general, a large interrogation spot results in higher SNR ratio, but the spatial resolution of a measurement will also decrease, and small scale information is lost. On the other hand, smaller interrogation spots can effectively increase the spatial resolution but the uncertainty also rises due to insufficient displacement of particle images. Furthermore, the spurious component created by the inherent uncertainty might be up to the same scale of magnitude of the real fluctuation and cause resolution failure. In order to further evaluate the change of the interrogation spot size to the overall 2-D PIV measurement reliability, a numerical simulation is performed using a synthetic 2-D potential flow vortex street field as shown in Figure 92 since a vortex street contains organized spatial characteristics which repeatedly appear and undergo a temporal life cycle such as coherent structures. Flow enhancement and cancellation due to opposite directions of swirling, vortex merge and viscous decay to allow parametric analysis based on above features. It is even more realistic in the PIV measurement for wall

turbulence where the mean flow is constant, and the flow is primarily 2-D. Sufficient and uniform Particle distribution is assumed.

First, a 2-D complex potential flow function $\omega = \phi + i\psi$ is generated. ϕ is the potential function; ψ is the stream function. By definition a velocity profile V(x, y) can be obtained by taking the gradient of the potential function to create a synthetic vortex. When the vector field of the unit vortex is generated, unreasonable components of large magnitude are replaced and smoothed. By observing the similarity between real vortex profiles in the PIV measurement, a Gaussian weighting function is applied to the unit vortex to simulate the radial decay nature of vortex streets. Second, a synthetic whole-flow domain is defined as the original vector field. The unit vortex is reproduced and distributed on the domain with an artificial downstream decay factor as function of position to simulate viscous dissipation of real vortex streets. A mean flow field of adjustable incident direction is applied to the flow field. Third, a second whole-flow domain with the size same as that of the first domain is generated. The vortices with a coarser spatial resolution at same positions are established as the counterpart of the PIV measurement result. A spatial cross-correlation is performed between the unit vortex and the two synthetic vector fields using different interrogation spot sizes and flow complicity setup. A comprehensive result is shown in the following figures.

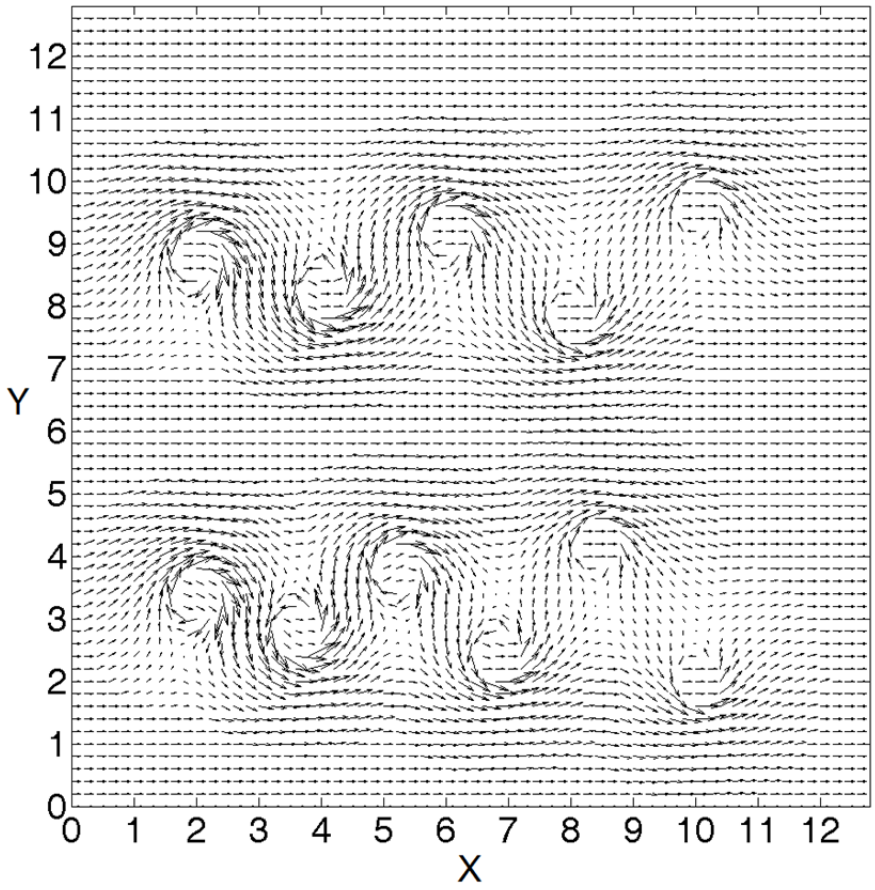

Figure 92 Synthetic vortex streets with uniform mean flow and viscous dissipation

A.1.2 Generation of synthetic vector field

A unit vortex is generated by the following potential flow function containing a mean flow, a doublet and a free vortex.

$$\omega = \phi + i\psi = UZ\exp(-i\theta) + \frac{Ua^2}{Z\exp(-i\theta)} - \frac{\Gamma}{2\pi} i\ln(Z)$$

U is the mean flow velocity, Z is the complex form of the x, y domain, θ is the incident direction of the mean flow, a is the radius of the doublet, Γ is the circulation. The first two terms represent the fluid passing over a solid rod of a in radius. In order to create a synthetic data field approximating a real velocity field, the above vortex is weighted to simulate the vector field from the top view PIV measurement. A visualization comparison between the resulting vortex and the PIV top view measurement is shown in Figure 93. The 0.1 spatial resolution of the synthetic vortex is adjustable.

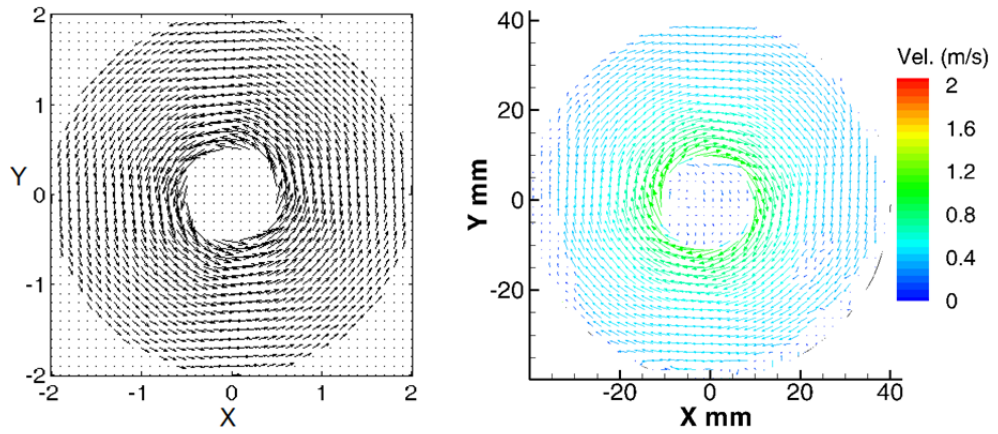

(a) (b)

Figure 93 Comparison between (a) synthetic vortex and (b) vortex by PIV

A synthetic flow field is established starting with 2 vortex streets. The direction of the mean flow is set to be from left to right of the flow field with an infinitesimal magnitude in order to simplify the flow condition. The vortex 1 and 2 are clockwise; vortex 3 and 4 are counter-clockwise. Based on a comprehensive flow setting purpose, vortex 1 and 2

are mild-contacted; vortex 2 and 3 are major-contacted. Vortex 4 is isolated from the others as an interference-free reference.

A spatial-averaged velocity field is constructed by the convolution of the original synthetic velocity field to a 2-D homogeneous low-pass filter window as

$$\bar{u} = \frac{1}{A}\iint u(s,r)b(x-s,y-r)ds \cdot dr$$

where s and r are two directions of convolution; b is an arbitrary filter; A is the normalizing area. An example of the original synthetic field compared to a coarsen vector field with 3 x 3 filter window, namely replacing 9 vectors within a 3 x 3 grid with an algorithmic averaged vector is shown in Figure 94 and Figure 95.

In additional to the analysis using synthetic free vortex streets, another case using forced vortex street is also performed to make comparison and to evaluate the sensitivity of the flow type change to the correlation signal strength. The synthetic forced vortex streets are placed at the same positions of the free vortex streets in previous case.

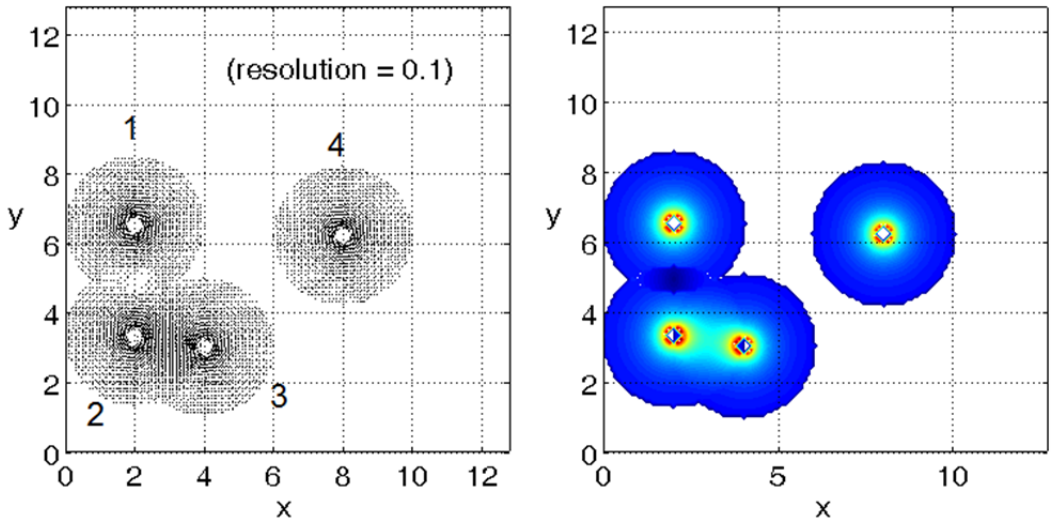

(a) (b)

Figure 94 Synthetic free vortex streets (a) original velocity vector field (b) original velocity magnitude contour

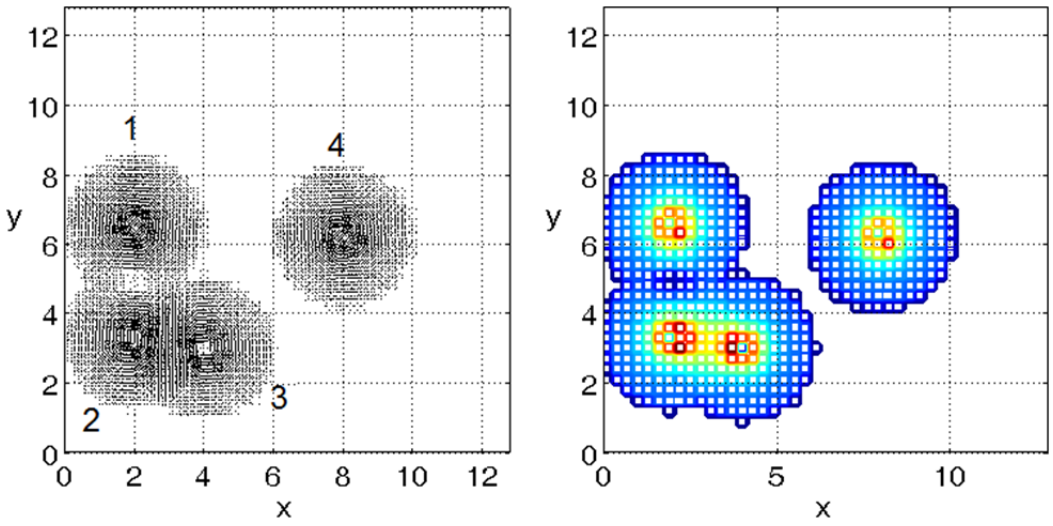

(a) (b)

Figure 95 Synthetic coarsen free vortex streets (a) 3 x 3 coarsen velocity vector field (b) 3 x 3 coarsen velocity magnitude contour

A.1.3 Synthetic data correlation

A cross-correlation of the synthetic velocity magnitude between the unit vortex and the 3 x 3 coarsen vector field with different vortex type is shown in Figure 96. The velocity magnitude correlation is analogous to the intensity field correlation in PIV image processing. It's found that the signal peak drops to lower than 90 % with respect to the correlation peak between the original vector field and the unit vortex. The accuracy of locating the vortex position also degrades from a point to an area on the signal peak. When the coarsen window increases to 5 x 5, the signal peak drops to 80 %. The effect of coarsen window size to the signal peak strength is shown in Figure 97. The tendency of peak strength to the coarsen window size is approximately linear. However, it's noticed that when the window size increases to larger than 9 x 9 in the forced vortex cases, the increasing spatial averaging effect between vortices in form of increasing the coarsen window size contribute to hold the signal strength from continuously decreasing. This happens in PIV measreuements when the vector compenents of many eddy structures contribute to an enhancing effect in a single interrogation spot. This phenomena also occurs in free vortex cases using window size larger than 6 x 6. Also when the window size increases to over 18 x 18, the synthetic data shows failure due to excessive vector contamination under the current flow field resolutioon and complicity. In general, the relation between the correlation window size to the signal strength can be refferred to the free vortex case result since the local scale tubulences are more like free

vortices. The two signal decay profiles of different slops indicate that the flow complicity dominates the correlation quality.

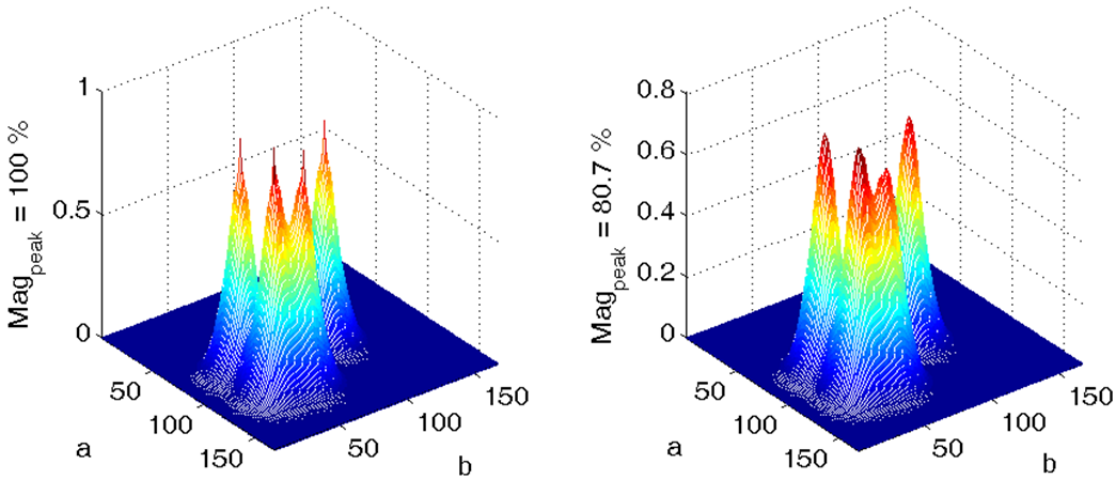

Figure 96 Correlation map of velocity magnitude (a) original field (b) 3x3 coarsen field

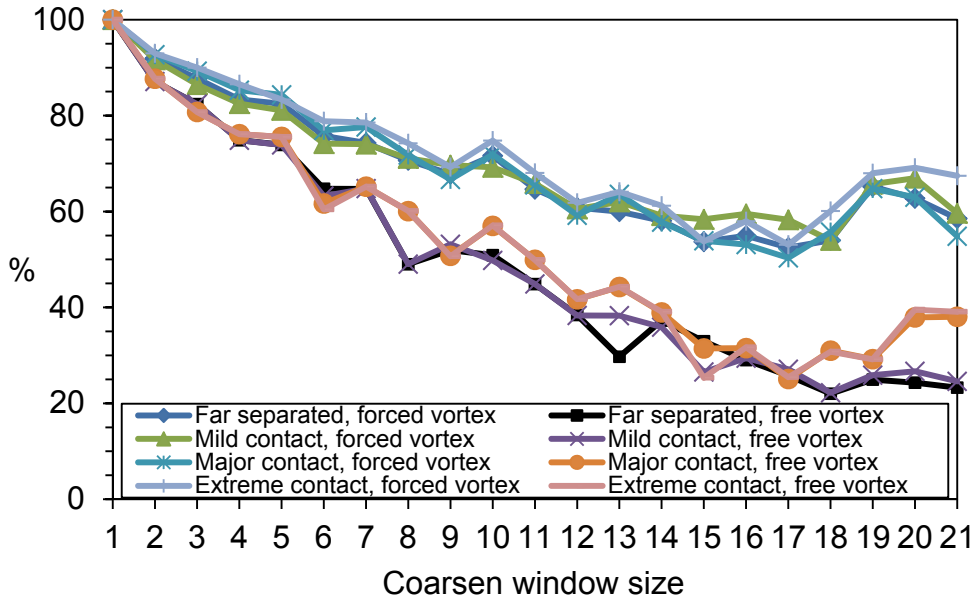

Figure 97 Peak strength versus coarsen window sizes under different flow conditions

In next, the flow condition is hold the same, but the spatial resolution to describe the entire flow domain is increased from 128 x 128 to 2048 x 2048, same as the pixel size of a real PIV image in this application. An extension of the two extreme contact cases in the previous figure is shown in Figure 98. The window size changes from 8 x 8 to 64 x 64. The free vortex case using different window sizes shows consistent decay profiles. The signal peak drop to 30 % while using the 16 x 16 window, 10 % while using the 32 x 32 window and 3 % while using 64 x 64 window. It comes to a conclude that when the interrogation spot size decreases from 64 pixels to 32 pixels, the signal strength to resolve the flow information increases by 3 times; when the spot size decreases from 32 to 16 pixels, the signal strength increases by another 3 times. As for the forced vortex case, the proportionality between velocity magnitude and radius makes the velocity vectors of larger magnitude more evenly distributed than in the free vortex case. Therefore the signal strength is relatively inconsistent due to the vector contamination.

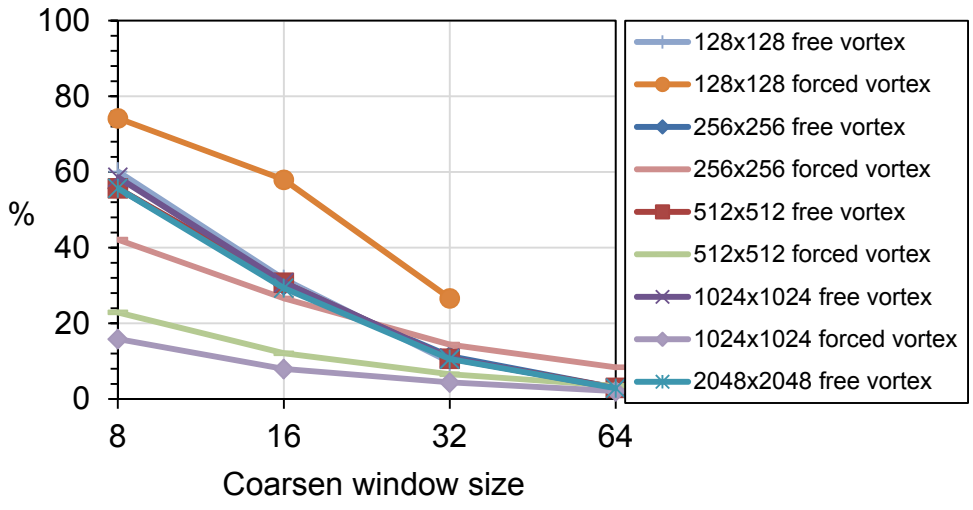

Figure 98 Peak strength versus coarsen window size under different spatial resolutions